The anisotropic space-time scaling of the atmosphere: turbulence and waves

Julien Pinel

Department of Physics

McGill University
Montreal, Quebec

February 2013

A thesis submitted in partial fulfillment of the requirements
of the degree of Doctor of Philosophy

ABSTRACT

This thesis addresses the problem of understanding and quantifying the variability of the atmosphere over wide ranges of space-time scales. We present empirical tests of a scaling model, the 23/9D model, which is an intermittent and anisotropic generalization of classical laws of turbulence - such as the Kolmogorov law - which describes how the statistical properties of atmospheric fields vary with spatial scales. We first address this problem for vertical sections for which there is still an ongoing debate about the nature of atmospheric dynamics: whether it is isotropic with a break in the horizontal scaling or anisotropic, but in a scaling manner. We make the first direct estimate of the joint horizontal-vertical structure function using wind velocity data measured on 14500 aircraft flights segments and demonstrate that it strongly supports the 23/9D model. We also study the consequences of this spatial anisotropy for the full horizontal space-time statistics. By considering that small structures are advected by larger turbulent ones and by considering averages over the latter, we theoretically obtain scale functions (which are generalizations of the notion of scale) which allow us to estimate structure functions and spectra. We test these predictions using geostationary satellite infrared data over the range 5 km to ~10000 km, 1 hour to 2 months. We found that our model could accurately reproduce the 3D (k_x, k_y, ω) spectral density over the range 1 hour to ≈4 days and 30 km to ≈5000 km. To obtain a more complete description of the statistics, we also found that our model accurately describes atmospheric radiances turbulent flux statistics (including infrared and passive microwave imagery over scale ranges of 100 km to 20000 km, 1 day to 1 year) with only small deviations at small and large scales. We finally show how to include atmospheric waves considered as strongly nonlinear phenomenon driven by turbulent fluxes and constrained by scaling symmetry, thus extending the 23/9D model. The theoretical development proposed is based on an effective turbulence - wave propagator which corresponds to a fractional and anisotropic extension of the classical wave equation propagator with dispersion relation similar to those of inertial gravity waves (and Kelvin waves) yet with anomalous (fractional) order $H_{wav}/2$. Using geostationary MTSAT IR radiances, we estimated the parameters finding that $H_{wav} \approx 0.17$ (the classical value =2).

RÉSUMÉ

Cette thèse s'intéresse au problème de comprendre et de quantifier la variabilité de l'atmosphère sur de grandes gammes d'échelles spatio-temporelles. Nous présentons des tests empiriques d'un modèle "scaling", le modèle 23/9D, qui est une généralisation intermittente et anisotrope des lois classiques de la turbulence - telle la loi de Kolmogorov - qui décrivent comment les propriétés statistiques des champs atmosphériques varient avec l'échelle spatiale. Nous abordons d'abord le problème pour des sections verticales par rapport auxquelles un débat sur la nature de la dynamique atmosphérique continue toujours: l'atmosphère est-il isotrope avec une brisure de symetrie d'échelle dans l'horizontal ou est-il décrit par une symétrie d'échelle, mais anisotrope ? Nous présentons le premier estimé direct de la fonction structure horizontale-verticale sur des vitesses de vent mesurées sur 14500 segments de vols d'avions et démontrons qu'elle supporte fortement le modele 23/9D. Nous étudions également les conséquences de cette symétrie d'échelle anisotrope sur les statistiques dans l'espace horizontal-temporel. En considérant que les plus petites structures turbulentes sont "advectées" par les plus grosses et en considérant un moyennage sur ces dernières, nous obtenons une forme théorique pour la fonction d'échelle (qui est une généralisation de la notion d'échelle), ce qui nous permet d'estimer les fonctions structure et les spectres. Nous testons ensuite ces prédictions à l'aide de données de rayonnement infrarouge prises par des satellites geostationnaires sur l'intervalle 5 km ~ 10000 km, 1 h ~2 mois. Nous avons trouvé que notre modèle pouvait précisement reproduire la densité spectrale 3D (k_x, k_y, ω) sur l'intervalle 1 h à ~ 4 jours et 30 km à ~5000 km. Afin d'obtenir une description statistique plus complète, nous avons également trouvé que notre modèle décrit précisement les statistiques des flux turbulents de rayonnements atmosphériques (dans l'infrarouge et pour les micro-ondes passives sur la gamme d'échelles 100 km a 20000 km, 1 jour a 1 an) avec seulement de légères déviations à petites et grandes échelles. Finalement, nous démontrons comment inclure les ondes atmosphériques, considerées ici comme un phénomène fortement non-linéaire dirigé par les flux turbulents et contraint par la symétrie d'échelle; étendant donc le modèle 23/9D. Les développements théoriques présentes sont basés sur un propagateur effectif turbulence-

ondes qui correspond a une extension fractionnaire et anisotrope du propagateur de l'équation d'ondes classique avec une relation de dispersion similaire à celle des ondes gravitationnelles inertielles (et des onde sde Kelvin), mais d'ordre anormal (fractionnaire) = $H_{wav}/2$. À l'aide de données infrarouge du satellite géostationnaire MTSAT, nous avons estimé les paramètres du modèle, trouvant $H_{wav} \approx 0.17$, (la valeur classique étant =2).

ACKNOWLEDGEMENTS

First, I would like to thank my supervisor Shaun Lovejoy for his time, his patience and his repeated explanations. Without his huge help, his scientific intuition and knowledge, this thesis wouldn't have been possible.

I would also like to thank Juan Gallego, who is always in a good mood and available to help with computer problems.

I would like to thank Jon Stolle for helping me with everything during my first years at McGill.

Finally, I would like to thank J-F Degardens, as well as my other colleagues from office 207, Elvis and Asmahan for all the discussions and laughing moments.

PREFACE AND CONTRIBUTION OF AUTHORS

All the work presented in this thesis is a reproduction of articles that were either accepted by or submitted to scientific journals. The research was made in collaboration with Shaun Lovejoy, Daniel Schertzer and Adrian Tuck and is presented here with their permission.

Chapter 2 reproduces the article: "Pinel, J., S. Lovejoy, D. Schertzer, A. F. Tuck, (2012): Joint horizontal - vertical anisotropic scaling, isobaric and isoheight wind statistics from aircraft data, **Geophysical Research Letters** (GRL) 39, L11803, doi:10.1029/2012GL051689" which investigates atmospheric turbulence in the vertical plane using aircraft wind data. It contains the first direct estimate of the joint horizontal-vertical structure functions. I performed the data analysis and I wrote the article in collaboration with my supervisor Shaun Lovejoy. Daniel Schertzer and Adrian Tuck provided helpful comments and advice.

Chapter 3 reproduces the article "Pinel, J., S. Lovejoy, D. Schertzer, (2013): The horizontal space-time scaling and cascade structure of the atmosphere and satellite radiances" submitted to **Atmospheric Research** in February 2013. It presents a study of the consequences of the anisotropic spatial scaling on the statistics in the full horizontal space-time domain. It extends the theoretical work started in [*Lovejoy and Schertzer*, 2010] to obtain 2D subsections of the 3D (k_x, k_y, ω) spectral density and test this using geostationary infrared radiances data. It also presents a study of atmospheric radiance flux intermittency in order to characterize their horizontal-space-time statistics. I performed the data analysis and wrote the article in collaboration with my supervisor Shaun Lovejoy. Daniel Schertzer provided helpful comments.

Chapter 4 reproduces the article "Pinel, J., S. Lovejoy, (2013): Atmospheric waves as scaling, turbulent phenomena" submitted to **Atmospheric Chemistry and Physics** in February 2013. It presents an extension of the 23/9D anisotropic scaling model to take into account the statistical description of atmospheric waves. Extending the

theoretical work by *Lovejoy et al.*, [2008] to take into account the random large scale turbulent advection, we obtain a concrete form for a turbulence-wave propagator and test this using geostationary infrared radiance data. I performed the data analysis and wrote the article in collaboration with Shaun Lovejoy.

TABLE OF CONTENTS

LIST OF TABLES

LIST OF FIGURES

Chapter 1: Introduction

The atmosphere is a highly nonlinear and complex turbulent system involving hierarchies of structures (eddies, vortices) of different sizes over wide ranges of spatial and temporal scales. The variability of such systems is characterized as a function of scale by the classical laws of turbulence. These laws are based on three features of the dynamical equations (e.g. the Navier-Stokes equations): the scale invariance of the nonlinear terms, the existence of scale by scale conserved fluxes and the fact that interactions are strongest between structures with similar sizes. Following the prototypical Kolmogorov law [*Kolmogorov*, 1941], they deduce the existence of a range of scales in which the fluctuations are scaling:

$$\Delta I\left(\underline{\Delta r}\right) \approx \varphi \left|\underline{\Delta r}\right|^{H}; \qquad \Delta I\left(\underline{\Delta r}\right) = I\left(\underline{r}+\underline{\Delta r}\right) - I\left(\underline{r}\right) \tag{1.1}$$

for a turbulent field I, where H is the scaling exponent, $\underline{r}$ is a position variable, $\underline{\Delta r}$ is a "lag" and its modulus $\left|\underline{\Delta r}\right|$ is the scale over which ΔI is estimated. The sign "≈" is to be understood as equality in probability distributions. φ is a scale by scale conserved turbulent flux which is transferred from one scale to another (e.g. from the coarser vortices to the finer). The Kolmogorov law, describing the velocity field, is recovered with H=1/3 and $\varphi = \varepsilon^{1/3}$ where ε is the energy flux transferred from large scales to a small "dissipation scale" at which the viscosity of the fluid dominates and the flux is dissipated. Similarly, the Corrsin-Obukhov law [*Corrsin*, 1951; *Obukhov*, 1949] for passive scalar advection has H=1/3 and $\varphi = \chi^{1/2}\varepsilon^{-1/6}$ with χ the passive scalar variance flux and the Bolgiano-Obukhov law [*Bolgiano*, 1959; *Obukhov*, 1959] for buoyancy-driven turbulence has H=3/5 and $\varphi = \phi^{1/5}$ with ϕ the buoyancy variance flux. Since the turbulent fluxes are transferred from one scale to another and this transfer is strongest between structures of similar sizes, the effects of large scale boundary conditions are progressively "forgotten" at small scales, so that the classical laws assumed turbulence to be, over their ranges of validity, isotropic and homogeneous. For the atmosphere, with gravity acting, the range of validity of the Kolmogorov law was believed to be only $0.2\ \text{cm} \ll \left|\underline{\Delta r}\right| \ll 100\ \text{m}$, [*Batchelor*, 1953]. Paradoxically, Kolmogorov scaling was found

to hold for much larger (up to planetary) scales in the horizontal, but has not been observed at all in the vertical [see the review by *Lovejoy and Schertzer*, 2010]. Furthermore, the assumption of homogeneity of the process of transfer of the fluxes is unrealistic, as noted by *Batchelor and Townsend*, [1949] turbulence is "spotty". Therefore when such laws are applied to the atmosphere, two difficulties have to be addressed: the atmosphere's strong intermittency and stratification.

The intermittency corresponds to the fact that the process of transfer of the turbulent fluxes from one scale to another is highly heterogeneous in space and in time. Up until the 1970s the intermittency was considered primarily as a source of small corrections to the spectral exponents so that its importance was underestimated. However, at the same time, explicit multiplicative cascade models [*Novikov and Stewart*, 1964; *Yaglom*, 1966; *Mandelbrot*, 1974] were developed in order to model intermittency. During the 80s, it was realized that multiplicative cascade models were the generic multifractal processes leading to non-classical "multifractal intermittency", [e.g. the universal multifractal model discussed in *Schertzer and Lovejoy*, 1987, 1997; *Schertzer et al.*, 1997]. Cascades involve scale invariant mechanisms which, repeated scale after scale, generate multifractal fluxes φ with different turbulent intensities obeying different scaling laws. This is responsible for the enormous variability of the atmosphere. In the atmosphere, the range of scales over which the fluxes are concentrated through the cascade mechanism is very large, so that the fraction of the total volume giving a significant contribution to, for instance, the energy flux $\left(\varepsilon \propto \Delta v^3\right)$ is low ≈0.01 % (using typical values of atmospheric intermittency parameters), [*Lovejoy and Schertzer*, 2013].

Before cascade models can be applied to the atmosphere, the range of scaling must be established. In particular, the stratification characterized by a large aspect ratio of the atmosphere (20000 km/10 km, horizontal/vertical) needs also to be taken into account. When one tries to apply the classical laws of turbulence to the atmosphere, a choice is immediately faced: to drop either the isotropy or the scaling symmetry. Following the development of theories of 2D isotropic turbulence [*Fjortoft*, 1953; *Kraichnan*, 1967] and the quasi-geostrophic extension by *Charney*, [1971], the usual approach hypothesizes that the isotropic symmetry is fundamental, postulating 3D isotropic dynamics at small scales and 2D isotropic dynamics at large scales - the 2D/3D

isotropic model of atmospheric turbulence - both regimes being separated by a break in the horizontal scaling at ≈10 km. However, gravity acts at all scales and it is argued in the alternative 23/9D model [*Schertzer and Lovejoy*, 1985a,b; 1987] that it induces anisotropies in a scaling manner so that the atmospheric dynamics are described by eq. (1.1) but with different vertical and horizontal fluxes φ and exponents H, over the whole dynamically significant ranges of scales: a single anisotropic scaling regime characterized by the intermediate, non-integer dimension 23/9 ≈2.56 which describes the scaling stratification of the atmosphere. This is described in the 23/9D model with the help of a "scale function" (presented in detail in chapters 2 and 3) which is a generalization of the notion of scale and which is convenient for describing anisotropic scaling.

Despite increasing empirical and theoretical evidence pointing towards anisotropic scaling [*Lovejoy and Schertzer*, 2010; *Tuck*, 2008; *Schertzer et al.*, 2012], the debate about the nature of atmospheric dynamics (isotropic with a break in the horizontal scaling vs. anisotropic scaling) continues. Virtually the only evidence supporting the 2D/3D isotropic model is the break in the horizontal scaling of the horizontal wind measured by aircraft. Even this is problematic: the break is at a few hundred km, (not at 10 km) and the transition is from H=1/3 at small scales to H=0.7 at large scales (and not to H=1 at large scales as predicted by the 2D/3D model). Since drop sondes in the vertical also found H~0.7 [*Lovejoy et al.*, 2007], it was shown by *Lovejoy et al.*, [2009a] that this break in the scaling could be explained by the aircraft followed gently sloping trajectories - such as isobars - so that at large enough scales, the vertical fluctuations (rather than horizontal ones) dominate the statistics. This implies that statistics measured by aircraft over isobars and isoaltitudes are different. The paper by *Lovejoy et al.* [2009a] sparked a debate [*Lindborg et al.*, 2009, 2010 ; *Lovejoy et al.*, 2009b, 2009c, 2010 ; *Schertzer et al.*, 2011, 2012 ; Yano, 2009] and provoked *Frehlich and Sharman* [2010] to perform a new analysis using Tropospheric Airborne Meteorological Data Reporting (TAMDAR) commercial aircraft wind data. The key new element was that - for the first time for commercial aircraft - the TAMDAR data had GPS altimetry and were thus able to adequately distinguish isobaric and isoheight statistics. Although *Frehlich and Sharman* [2010] did not find a transition at 10 km, nor from H=1/3 at small scales to H=1 at large scales, they did make the claim that statistics measured over isobars and isoheight

were the same, bringing into question the arguments proposed by *Lovejoy et al.* [2009a]. This motivated chapter 2: the first estimate of the joint horizontal-vertical statistics from 14500 flight segments giving a high precision confirmation of the theory ($D_{el} \sim 2.57 \pm 0.02$ rather than $23/9 \approx 2.56$).

The basic 23/9D model is for the spatial statistics. However, since the wind field connects space and time (not only dimensionally, also physically via advection), this model has consequences for the full space-time structure. If we want to understand the statistics in the more convenient Eulerian framework, a classical way to obtain temporal statistics which can be applied when the turbulent fluctuations are sufficiently small compared to an imposed mean flow - such as in laboratory turbulence - is provided by Taylor's hypothesis of "frozen turbulence" [*Taylor*, 1938], for which the imposed constant mean flow velocity relates temporal to spatial statistics. As argued in the 23/9D model, no such scale separation exists in the atmosphere and another model for space-time statistics is needed. As argued by *Tennekes*, [1975], even if we consider a flow with zero imposed mean horizontal velocity, smaller structures will still be advected by larger (planetary sizes) ones in the scaling regime. Based on the Galilean invariance of the dynamical equations and boundary conditions, we can easily consider the case of a constant deterministic advection. But since the statistical properties of real atmospheric fields are influenced by random turbulent velocities, following the work by *Lovejoy and Schertzer*, [2010], we consider averages over these to theoretically obtain scale functions (which are generalizations of the notion of scale) which allow us to estimate statistics (structure functions and spectra). Because (x, y, z, t) data sets spanning significant ranges of scales are not available, we only consider the horizontal (x, y, t) space-time. We extend the work by *Lovejoy and Schertzer*, [2010], obtaining theoretical expressions for 2D subsections of the 3D (k_x, k_y, ω) spectral density and we test this empirically using two months of geostationary satellite infrared radiance.

Atmospheric field space-time statistics can be further characterized considering the general feature of turbulent flows that there exists a statistical relation between size of structures and their lifetime (their "eddy turnover time"). For the wind field, $\Delta v = \varepsilon^{1/2} \Delta t^{H_\tau}$ with H_τ=1/2. This is a Lagrangian relation which is used conceptually in meteorology in constructing space-time "Stommel" diagrams but has generally not been

directly calculated empirically, as it needs datasets with large scale ranges in both space and time. We investigate this using atmospheric radiance fluxes measured from geostationary as well as orbiting satellite.

The basic space-time extension of the 23/9D model describes structures that are localized in space-time and live for a well defined duration, in accord with the usual turbulence phenomenology. Since it is only constrained by scaling symmetry, we can also consider the possibility of including in the description structures that are localized in space but unlocalized in space-time: atmospheric waves. Even though the atmosphere is highly nonlinear, atmospheric waves are modeled by linear (or weakly linear) theories; commonly with Taylor-Goldstein equations which are the results of linearization and from which we obtain the dispersion relations to be tested empirically [*Nappo*, 2002]. These linear theories also predict the space-time propagators relating wave forcings and responses; obtained from wave equations involving only integer powers of space and time differential operators which is an unnecessary constraint on the form of the propagators. In order to have a theoretically consistent approach (i.e. strong nonlinearity), we consider waves as a strongly nonlinear phenomenon driven by turbulence fluxes which are only constrained by scaling symmetries. This is described by a wave-extended 23/9D model involving an effective turbulence-wave propagator which corresponds to possibly fractional wave equations driven by turbulent flux forcing. Extending the work by *Lovejoy et al.*, [2008] to take into account the random large scale turbulent advection, we obtain a concrete form for the turbulence-wave propagator and test this using geostationary infrared radiance data.

The 23/9D model is thus an anisotropic scaling multiplicative cascade model which is a generalization of the classical laws of turbulence and which basically describes the statistical properties of the turbulent atmosphere in the spatial domain. This thesis presents an empirical test of the model for vertical sections, as well as theoretical space-time and wave extensions (and their corresponding empirical tests). Chapter 2 presents the empirical test of the 23/9D model for vertical sections using wind velocity measured by commercial aircraft. Chapter 3 presents the theoretical space-time extension of the 23/9D model as well as the empirical test in horizontal space-time using geostationary satellite infrared radiances data. We also investigate the question of intermittency using

geostationary as well as orbiting satellites radiances in infrared and passive microwave. Finally, chapter 4 presents the extension of the 23/9D model to waves and the empirical test using geostationary satellite infrared radiances data. We conclude in chapter 5.

Chapter 2: Joint horizontal-vertical anisotropic scaling, isobaric and isoheight wind statistics from aircraft data

The following reproduces the article: "Pinel, J., S. Lovejoy, D. Schertzer, A. F. Tuck, (2012): Joint horizontal - vertical anisotropic scaling, isobaric and isoheight wind statistics from aircraft data, Geophysical Research Letters (GRL) 39, L11803, doi:10.1029/2012GL051689" which investigates atmospheric turbulence in the vertical plane using aircraft wind data.

Abstract

Aircraft measurements of the horizontal wind have consistently found transitions from roughly $k^{-5/3}$ to $k^{-2.4}$ spectra at scales Δx_c ranging from about 100 - 500 km. Since drop sondes find $k^{-2.4}$ spectra in the vertical, the simplest explanation is that the aircraft follow gently sloping trajectories (such as isobars) so that at large scales, they estimate vertical rather than horizontal spectra. In order to directly test this hypothesis, we used over 14500 flight segments from GPS and TAMDAR sensor equipped commercial aircraft. We directly estimate the joint horizontal-vertical (Δx, Δz) wind structure function finding - for both longitudinal and transverse components - that the ratio of horizontal to vertical scaling exponents is $H_z \approx 0.57 \pm 0.02$, close to the theoretical prediction of the 23/9D turbulence model which predicts $H_z = 5/9 = 0.556$ This model also predicts that isobars and isoheight statistics will diverge after Δx_c; using the observed fractal dimension of the isobars ($\approx 1.79 \pm 0.02$), we find that the isobaric scaling exponents are almost exactly as predicted theoretically and $\Delta x_c \approx 160$, 125 km, (transverse, longitudinal). These results thus give strong direct support to the 23/9D scaling stratification model.

2.1 Introduction

The classical laws of turbulence exploit the scale invariance of the dynamical equations to predict the scaling behaviour of the wind and other turbulent fields. For simplicity, they also assume statistical rotational invariance: isotropy. When applying

these laws to the strongly stratified atmosphere, one faces a choice: to drop either the scaling or the isotropy symmetry. Starting with the claimed discovery of the meso-scale gap [*Van der Hoven*, 1957], and the subsequent development of theories of 2D (isotropic) turbulence [*Kraichnan*, 1967] - and especially Charney's geostrophic variant [Charney, 1971] - the dominant choice was to drop the scaling symmetry, to assume that the small scale dynamics were 3D isotropic and the large scale 2D isotropic with a scale break somewhere near the atmospheric scale height (≈10 km).

Starting in the early 1980s the opposite proposal was made [*Schertzer and Lovejoy*, 1985b, 1987]: to drop isotropy but to maintain wide range horizontal scaling. In this framework, the vertical structure was also expected to be scaling but with different exponents than the horizontal. Since then, evidence in the horizontal and vertical from satellites, lidar, aircraft, radiosondes, drop sondes and reanalyses has accumulated, supporting the anisotropic scaling model (see the review *Lovejoy and Schertzer* [2010] and also *Tuck* [2008]). More recently, an (anisotropic) scaling (rather than a traditional scale) analysis of the governing equations [*Schertzer et al.*, 2012] has allowed the derivation of new fractional vorticity equations with anisotropic scaling solutions.

Until recently, the outstanding piece of evidence supporting the isotropic 2D/3D model and potentially falsifying the anisotropic scaling hypothesis was the observed break in aircraft spectra of the horizontal wind at scales of several hundred kilometers. However, using high quality scientific aircraft data, *Lovejoy et al.* [2004, 2009a] argued that the aircraft trajectories - and hence the wind measurements - would be affected by the turbulence and they predicted a transition from $k^{-\beta_{small}}$ spectra with $\beta_{small} \sim \beta_h$ and $\beta_h \sim 5/3$ at small horizontal scales to $k^{-\beta_{large}}$ spectra at large scales where the aircraft essentially sensed the vertical rather than horizontal fluctuations; with vertical exponent $\beta_{large} \sim \beta_v$ and $\beta_v \sim 2.4$. They also showed that essentially all the horizontal wind spectra and structure functions published to date were compatible with this transition □but not with the more drastic transition from $\beta_{small}=5/3$ to $\beta_{large}=3$ near 10 km predicted by the competing 2D/3D model.

The paper by *Lovejoy et al.* [2009a] sparked a debate [*Lindborg et al.*, 2009, 2010 ; *Lovejoy et al.*, 2009b, 2009c, 2010 ; *Schertzer et al.*, 2011, 2012 ; Yano, 2009] and

provoked *Frehlich and Sharman* [2010, hereafter FS] to perform a new analysis using Tropospheric Airborne Meteorological Data Reporting (TAMDAR) commercial aircraft data. The key new element was that the TAMDAR data had GPS altimetry and were thus - for the first time for commercial aircraft - able to adequately distinguish isobaric and isoheight statistics. This is important because most aircraft follow isobars and these are gently sloping. If these slopes are large enough, then the aircraft spectra will show a spurious transition from β_h to β_v at a scale which depends on the slope and the turbulent fluxes, thus explaining the observations. FS found neither a scale break near 10 km nor a structure function with exponent anywhere near 2 (corresponding to $\beta_{large}=3$) - so that presumably there was not a 2D/3D transition. However, they did make the strong claim that the statistics on isobars and isoheights were identical. If their claim was true, then another mechanism to account for the $k^{-5/3}$ to $k^{-2.4}$ transition would be required.

However, distinguishing the statistics on isoheights and isobars requires very high accuracy - both of wind but especially altitude - measurements. These accuracy requirements are too demanding for the older Aircraft Meteorological Data Relay (AMDAR) equipment (also discussed by FS). With the newer GPS equipped TAMDAR data, the requisite accuracy is possible to achieve if two conditions are met. First, we do not use wind differences from two *different* aircraft since this involves both larger (absolute) errors as well as nontrivial complications due to the very inhomogeneous distribution of TAMDAR flights paths over the US: the errors are unacceptably large. Second, the TAMDAR sampling protocol was ill adapted for our purpose, it was essential to use only the high quality "cruise" flight segments. Unfortunately, the copiously sampled ascent and descent segments had to be discarded because of their unacceptably low vertical resolutions (see Figure A.3 from appendix A). Using two aircraft differences and these low resolution segments, we could accurately reproduce the FS TAMDAR results (see Figures A.1 and A.2 from appendix A).

Finally, we could mention that *Lovejoy and Schertzer* [2010] examined hydrostatic models and found that they also gave isobaric exponent β~2.4 and *Lovejoy and Schertzer* [2011] confirmed this in reanalyses, although with an extra complication due to a strong horizontal (zonal/meridional) scaling anisotropy (i.e. different exponents in orthogonal horizontal directions); so that these data are not appropriate for

distinguishing isoheight and isobaric statistics. With these differences, we therefore redid the FS TAMDAR analyses.

2.2 Generalized Scale Invariance

Isotropic turbulent laws are of the general type: $\Delta v = f\,|\Delta \boldsymbol{r}|^{H}$, where Δv is a fluctuation in a turbulent field v, f is a scale by scale conserved turbulent flux, $|\Delta \boldsymbol{r}|=|(\Delta x, \Delta z)|$ is the length of the horizontal, vertical lag vector over which Δv is calculated (for simplicity, we consider only a single horizontal component of the velocity field) and H is the scaling (non conservation, mean fluctuation) exponent. Anisotropic scaling turbulence has different vertical (H_v) and horizontal (H_h) exponents which result when different conserved turbulent fluxes dominate the corresponding dynamics, for example:

$$\Delta v(\Delta x) = \varepsilon^{1/3} \Delta x^{H_h} \qquad (2.1)$$

$$\Delta v(\Delta z) = \phi^{1/5} \Delta z^{H_v}$$

where ε and ϕ are the energy and buoyancy variance fluxes (i.e. $f = \varepsilon^{1/3}, \phi^{1/5}$ respectively and H_h=1/3 and H_v=3/5). The horizontal law is the Kolmogorov, 1941 scaling and the vertical is the Bolgiano-Obukhov, 1959 scaling. The way to deal with this anisotropy while keeping an overall scaling symmetry is to replace the usual vector norm for the spatial separation by a different measure of scale - the (anisotropic) scale function - a simple example for vertical sections is:

$$[[\Delta \boldsymbol{r}]] = l_s \left\{ |\Delta x / l_s| + |\Delta z / l_s|^{1/H_z} \right\} \qquad (2.2)$$

where $H_z=H_h/H_v$=5/9 and l_s is the "sphero-scale": the scale at which structures are "roundish". (If needed, the scale function can be generalized for full space-time vector displacements.) The anisotropy is reflected by the exponent $H_z \neq 1$ that describes the stratification of structures. Since $H_z<1$, at scales much smaller than l_s, structures tend to be vertically aligned whereas at scales much larger than l_s, they become horizontally flatter. With this scale function, we can write:

$$\Delta v(\Delta \boldsymbol{r}) = \varepsilon^{1/3} [[\Delta \boldsymbol{r}]]^{1/3} \qquad (2.3)$$

which, for $\Delta \boldsymbol{r}=(\Delta x, 0)$, $\Delta \boldsymbol{r}=(0, \Delta z)$ reduces to equation (2.1). The vertical extent of structures of horizontal size L is L^{H_z} ; their volumes are $L^{D_{el}}$ with $D_{el}=2+H_z=23/9$; this is the 23/9D model [*Schertzer and Lovejoy*, 1985a,b]).

2.3 Data Analysis

TAMDAR equipped aircraft make short range flights at low altitudes mostly below 7 km; their sensors are the most modern in the AMDAR programme [*Moninger et al.*, 2008 ; *Daniels et al.*, 2004] and were designed to measure atmospheric fields including wind, humidity, pressure and temperature, as well as location, time and altitude from a built-in GPS. The sampling protocol is important to understand: the system either makes measurements due to significant changes in pressure (changes of 10 hPa or 50 hPa, depending on the altitude) or - if cruising at nearly constant pressure - it switches to a time-based protocol, making measurements every 3 or 7 minutes (again, depending on the level). For an aircraft flying at 500 km/h at an altitude of 5.5 km, the former corresponds to ~25 km. We analysed data for the year 2009 over roughly the continental US (20°N to 50°N latitude). In order to have good statistics and to minimize the strong altitude dependence, we confined our analysis to the layer between 5 and 5.5 km altitude using over 14500 aircraft legs. Only the highest quality data (according to automated quality control checks) were kept.

A nonobvious problem arises since the data were passed through a 10 second smoother, so that ascents and descents at 250 km/h and angle of 15° correspond to a section 180 m thick. Including these low resolution segments led to biases of 7% at 200 km, but this rapidly increased to 67% at 400 km, hence we discarded them (appendix A, Figure A.3). This bias, their use of multi-aircraft data pairs and the fact that FS took much thicker layers for isobars and isoheights (4 hPa, 200 m) compared to those used here (1.26 hPa, 20 m) led to our qualitatively different conclusions (Figures A.1 and A.2). Similarly to FS, we took only time intervals less than 1 hour to limit the effects of noninstantaneous measurements.

From the near-constant altitude and near-constant pressure levels, we estimated second order structure functions $D_{ii} = \left\langle \left| \Delta v_i(\Delta \boldsymbol{r}) \right|^2 \right\rangle = \left\langle \left| v_i(\boldsymbol{r}+\Delta \boldsymbol{r}) - v_i(\boldsymbol{r}) \right|^2 \right\rangle$ where $\langle . \rangle$

means ensemble average, i=N,L for transverse, longitudinal components respectively. The accuracies were estimated from the structure function at small enough lags; per component, the absolute calibration error is ≈±1.8 m/s, the relative calibration error is <±1.8 m/s and the altitude error is ≈±3 m (close to the manufacturer's values ±2-3 m/s on wind speed and ±3 m on altitude, [*Daniels et al.*, 2004]). To eliminate the absolute calibration errors and numerous other problems introduced by the highly nonuniform distribution of TAMDAR trajectories, we always computed velocity increments with data coming from the same aircraft.

2.4 Results

Taking ensemble averages of the square of equation (2.3), we obtain:

$$\left\langle \left|\Delta v(\Delta \boldsymbol{r})\right|^2 \right\rangle = \left\langle \varepsilon^{2/3} \right\rangle [[\Delta \boldsymbol{r}]]^{2H_h} = \left\langle \left|\Delta v(l_s)\right|^2 \right\rangle \left\{ \left|\Delta x/l_s\right| + \left|\Delta z/l_s\right|^{1/H_z} \right\}^{\xi_h(2)} \tag{2.4}$$

where $\xi_h(2)$ is the second order structure function exponent which takes into account the intermittency of ε. Since $\left\langle \varepsilon^{2/3} \right\rangle \sim [[\Delta \boldsymbol{r}]]^{-K_\varepsilon(2/3)}$, we have $\xi_h(2)=2H_h-K_\varepsilon(2/3)$ where $K_\varepsilon(2/3)$ is a small intermittency exponent (~ -0.07, see [*Lovejoy et al.*, 2010]). From its definition and the assumption of statistical translational invariance, $\left\langle \left|\Delta v(\Delta \boldsymbol{r})\right|^2 \right\rangle = \left\langle \left|\Delta v(-\Delta \boldsymbol{r})\right|^2 \right\rangle$; we also assumed left-right symmetry so that the four quadrants of $\left\langle \left|\Delta v(\Delta x, \Delta z)\right|^2 \right\rangle$ are symmetric. In order to test the theory, we estimated the parameters in equation (2.4) by regression. First, $\xi_h(2)$ was estimated from linear regression using 1D structure functions (Figure 2.3a), yielding $\xi_{h,N}(2)=0.81\pm0.02$ and $\xi_{h,L}(2)=0.76\pm0.03$ which are close to the Kolmogorov value corrected for intermittency: $2H_h+0.07\approx0.74$. Only vector lags with at least 500 independent aircraft Δv^2 estimates were used, the average number over the regressions range 16 km < Δx < 400 km - see Figure 2.3 - was 24800. Since presumably $\xi_{h,N}(2)= \xi_{h,L}(2)$, we took the value $\xi_h(2)=0.8$. Then, from multivariate regression on the joint lags (cross-section, Figure 2.1), we obtained $H_{z,N}\sim H_{z,L}\sim0.57\pm0.02$, $l_{s,N}\sim l_{s,L}\sim1.0\pm0.1$ mm and $\left\langle \left|\Delta v(l_s)\right|^2 \right\rangle_N^{1/2} \sim 3.2\pm0.2$ mm/s, $\left\langle \left|\Delta v(l_s)\right|^2 \right\rangle_L^{1/2} \sim 2.0\pm0.2$ mm/s. While H_z is close to the theoretical value $H_z=H_h/H_v=(1/3)/(3/5)\approx0.56$, the sphero-scale is a bit smaller than the

one estimated (l_s~4-80 cm) by *Lilley et al.* [2004] ; *Lovejoy et al.* [2009a] and *Lovejoy and Schertzer*, [2010]. From H_z, we can estimate the vertical scaling exponent $\xi_{v,N}(2)= \xi_{h,N}(2)/H_{z,N}=1.42\pm0.06$ and $\xi_{v,L}(2)= \xi_{h,L}(2)/H_{z,L}=1.33\pm0.07$ values consistent with direct estimates of vertical exponents ($\xi_v(2)$~1.35 at 6 km) from drop sondes by *Lovejoy et al.* [2007]. Interestingly, while both the horizontal and vertical $\xi(2)$ are little larger than the theoretical values (ignoring intermittency, 2/3, 6/5 respectively) yet, as expected, their ratio H_z is almost the same: 0.8/1.4=0.57. These exponents are far from the theoretical values of 2D isotropic turbulence $\xi_h(2)=2$, $H_z=0$. The overall fits (for $|\Delta z| < 40$ m and $|\Delta x| < 275$ km) are shown in Figure 2.1, they are very good with mean relative deviations ±6% and ±4% (transverse, longitudinal respectively). Although the vertical range of scales is short, to our knowledge, Figure 2.1 constitutes the first direct estimate of the joint horizontal-vertical structure function; and it gives strong support to the hypothesis of horizontal-vertical anisotropic scaling.

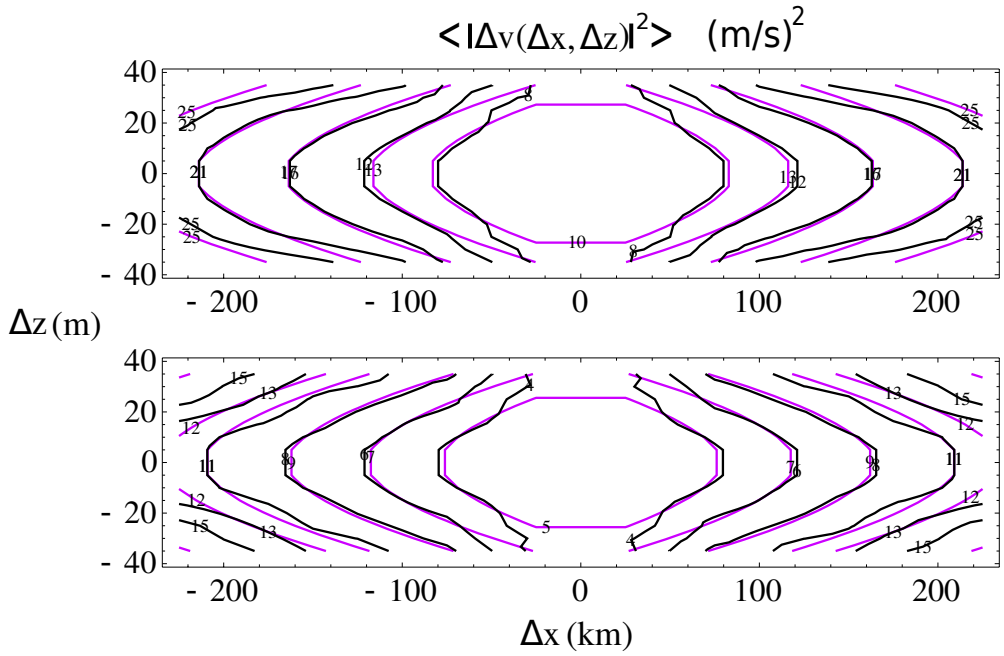

Figure 2.1: Contour plot of $\left\langle \left|\Delta v(\Delta x,\Delta z)\right|^2 \right\rangle$, in black: horizontal wind measured by TAMDAR. In purple, a fit with the help of the scale function (equations (2.2) and (2.3)). Up: transverse component. Bottom: longitudinal component. Parameters are : $l_{s,N}$~$l_{s,L}$~1.0±0.1 mm, $\xi_h(2)$=0.8 (from 1D structure functions fits) and $H_{z,N}$~$H_{z,L}$~0.57±0.02 and $\left\langle \varepsilon_N^{2/3} \right\rangle^{3/2}$ ~(10±1)x10^{-6} m^2/s^3, $\left\langle \varepsilon_L^{2/3} \right\rangle^{3/2}$ ~(4.0±0.8)x10^{-6} m^2/s^3. The average relative error between fitted and empirical curves, the mean of $\dfrac{\left|\left\langle \left|\Delta v\right|_{fit} \right\rangle - \left\langle \left|\Delta v\right|_{emp} \right\rangle\right|}{\left\langle \left|\Delta v\right|_{fit} \right\rangle}$ is ~ 6% (4%) for transverse (longitudinal) component.

2.5 Fractal aircraft trajectories

In order to compare statistics at constant pressures and constant altitudes, we need to take into account the fractality of the aircraft trajectories. This fractality arises because aircraft at cruising altitudes fly on roughly isobaric levels and these are fractal [*Lovejoy et al.*, 2004], (although, due to aircraft inertia, at scales < 3 km, the trajectories become smooth). This implies:

$$\left\langle \left|\Delta z(\Delta x)\right| \right\rangle \sim \left(\frac{\Delta x}{L_f}\right)^{H_{tr}} \left\langle \left|\Delta z(L_f)\right| \right\rangle \qquad (2.5)$$

where $\left\langle \left|\Delta z(\Delta x)\right| \right\rangle$ is the average vertical displacement of an aircraft over a horizontal lag Δx, L_f~180 km is the average length of our TAMDAR flight segments, (chosen as a

convenient reference scale) and $H_{tr} = D_{tr} - 1$ where D_{tr} is the fractal dimension of the "trajectory" (more precisely, it corresponds to the fractal dimension of the set of points on our isobaric sample). From Figure 2.2, we find $H_{tr} = 0.79 \pm 0.02$ and $\langle |\Delta z(L_f)| \rangle \sim 19 \pm 2$ m (which represents the average vertical displacement of the isobaric sample over L_f).

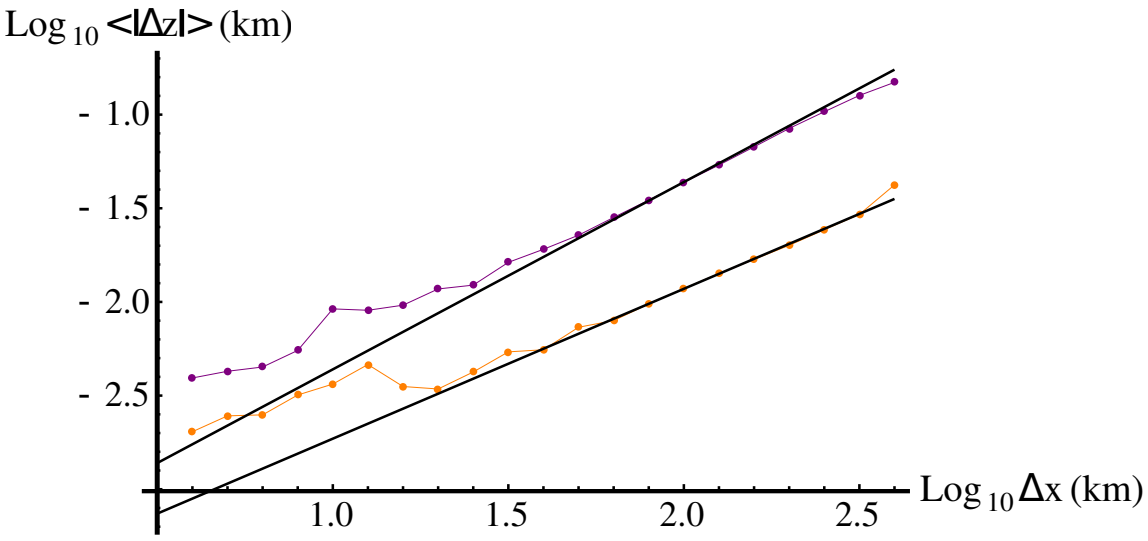

Figure 2.2: Mean vertical displacement as a function of horizontal separation. In orange: structure function calculated over near-constant pressure levels (Δp<1.26 hPa). In purple: structure function calculated over near-constant pressure levels with an additional constraint on the slope ($\Delta z/\Delta x > 3 \times 10^{-4}$). Reference lines have slopes 0.8 and 1.0. The near-constant altitude (orange) curve shows a break in scaling symmetry for Δx<16 km due to poor statistics.

To investigate the consequences for the velocity fluctuations statistics, we can use equation (2.2) and make a rough "mean field" type argument [see *Lovejoy et al.*, 2009a], where, in the scale function (equation (2.2)), we replace Δz with $\langle |\Delta z(\Delta x)| \rangle$ from equation (2.5):

$$\left\langle |\Delta v(\Delta x)|^2 \right\rangle \sim \left\{ \left| \frac{\Delta x}{l_s} \right| + \left| \frac{\Delta x}{\Delta x_0} \right|^{H_{tr}/H_z} \right\}^{\xi_h(2)} ; \; \Delta x_0 = L_f \left(\frac{l_s}{\langle |\Delta z(L_f)| \rangle} \right)^{1/H_{tr}} \qquad (2.6)$$

Since $H_{tr}>H_z$, for isobars, there is a critical scale Δx_c for which, (taking $\xi_v(2)=\xi_h(2)/H_z$~0.8/0.57~1.4) :

$$\left\langle \left|\Delta v(\Delta x)\right|^2 \right\rangle \sim \left|\Delta x\right|^{\xi_h(2)} = \left|\Delta x\right|^{0.8} \quad \Delta x \ll \Delta x_c \qquad ; \; \Delta x_c \sim \left(\Delta x_0^{H_{tr}} l_s^{-H_z}\right)^{1/(H_{tr}-H_z)} \tag{2.7}$$

$$\left\langle \left|\Delta v(\Delta x)\right|^2 \right\rangle \sim \left|\Delta x\right|^{H_{tr}\xi_v(2)} = \left|\Delta x\right|^{1.1} \qquad \Delta x \gg \Delta x_c$$

The value of Δx_c depends on the turbulent fluxes (through the parameter l_s) and on Δx_0. Figure 2.3 (top) compares the horizontal structure functions for near-constant pressure and altitude levels. As expected, the two curves are nearly identical for scales smaller than $\Delta x_{c,N}$ ~160 km, $\Delta x_{c,L}$ ~125 km, and follow a straight line with slope $\xi_h(2)$~0.8. As predicted, for scales larger than Δx_c, the near-isobaric (orange) curve follows a new line with slope $H_{tr}\xi_v(2)$~1.1. At the extreme large scale limit of our data (~300 km), there is a small deviation in the scaling of the longitudinal component. We checked that at this scale, there was a 25% difference in the contribution to $\left\langle \left|\Delta v_L(\Delta x)\right|^2 \right\rangle$ for positive and negative Δv_L ; since the aircraft mostly made round trips, this must be a consequence of the pilot modifying the trajectories depending on the weather - particularly affecting longitudinal components - hence introducing correlations between the aircraft and wind. By taking the ratio of the isobaric and isoaltitude $\left\langle \left|\Delta v\right|^2 \right\rangle$ we largely eliminate this effect (Figure 2.3b): as predicted, the isoheight to isobar ratio continues to grow with scale with exponent ≈0.3.

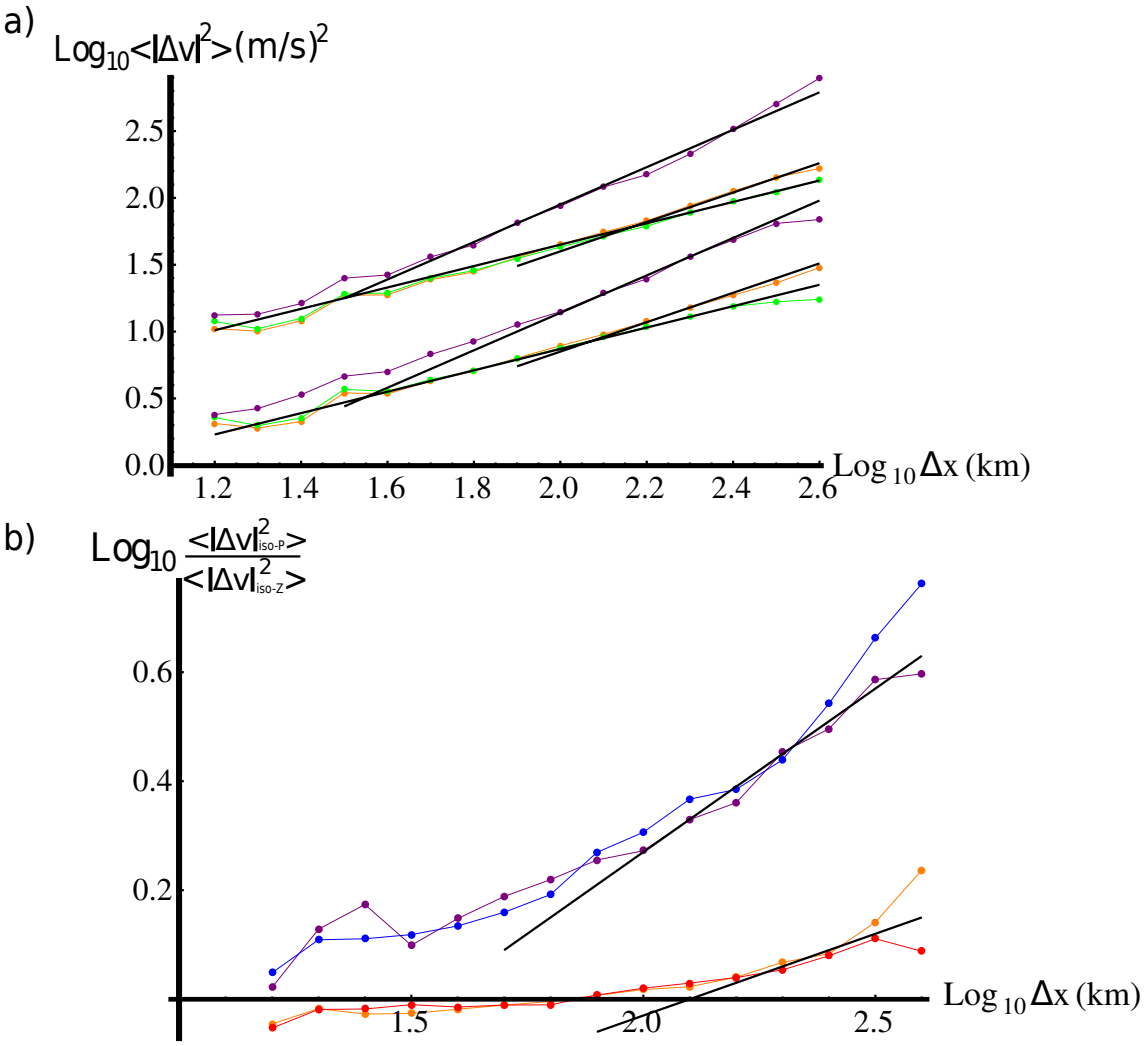

Figure 2.3: a) : $\left\langle \left|\Delta v(\Delta x,\Delta z)\right|^2 \right\rangle$ for the transverse (upper curves) and longitudinal (lower curves) components of the wind measured by TAMDAR. The curves for transverse components were displaced in the vertical by 0.5 for clarity. In green: $\left\langle \left|\Delta v(\Delta x,\Delta z)\right|^2 \right\rangle$ calculated over near-constant altitude levels (Δz<20 m). In orange: $\left\langle \left|\Delta v(\Delta x,\Delta z)\right|^2 \right\rangle$ calculated over near-constant pressure levels (Δp<1.26 hPa). In purple: $\left\langle \left|\Delta v(\Delta x,\Delta z)\right|^2 \right\rangle$ calculated over near-constant pressure levels with an additional constraint on the slope ($\Delta z/\Delta x > 3\text{x}10^{-4}$). Reference lines have slopes 0.8, 1.1 and 1.4. b) : in orange (red) : difference between the logs of $\left\langle \left|\Delta v(\Delta x,\Delta z)\right|^2 \right\rangle$ calculated on near-constant pressure and near-constant altitude levels for the transverse (longitudinal) component. In Purple (blue): difference between the logs of $\left\langle \left|\Delta v(\Delta x,\Delta z)\right|^2 \right\rangle$ calculated on near-constant pressure with the additional constraint on the slope ($\Delta z/\Delta x > 3\text{x}10^{-4}$) and near-constant altitude

levels for the transverse (longitudinal) component. Reference lines have slopes 0.3 and 0.6.

This $2+H_z$=2.57 dimensional turbulence has transverse to longitudinal ratio D_{NN}/D_{LL}~1.78±0.08, somewhat higher than the theoretical 3D, 2D isotropic turbulence values (D_{NN}/D_{LL}~4/3, 5/3, respectively [*Monin and Yaglom*, 1975; *Ogura*, 1952 ; *Lindborg*, 1999]).

In order to further test the 23/9D theory, we show the results for data pairs constrained to have slopes > $3x10^{-4}$ (roughly the mean isobaric slope at 400 km resolution), this sampling is linear (H_{tr}~1, top, Figure 2.2) so that we expect exponents $H_{tr}\zeta_v(2)$~1.4. This is confirmed by Figure 2.3a (top) at scales > 40 km: it is the slope, not the pressure that is important. For these conditional isobaric curves, Figure 2.3a indicates Δx_c~36 km, a value close to Δx_c~40 km estimated using equation (2.7) and parameters estimated on Figures 2.1 and 2.2. The bottom of Figure 2.3 shows the difference between isobaric (with and without the condition on the slopes of the smaple) and near-constant altitude cases. For increasing horizontal lags, the difference between the isobaric and near-constant altitudes curves increase, showing the relevance of the 23/9D model and the effect of fractal trajectories/sampling as described by equation (2.5). Interestingly, the previous studies cited (from flights near the top of the troposphere, including Figures 1, 2 of FS) find $\xi(2)$~1.4 so that presumably for these, H_{tr}~1.

2.6 Conclusions

The horizontal wind field is anomalous in that it has a break in the scaling at scales typically in the range 100 - 500 km with small scale spectra roughly $k^{-5/3}$ transitioning at lower wavenumbers to ≈ $k^{-2.4}$. Both the transition scale and exponent are quite different from those predicted by theories of isotropic 3D and isotropic 2D turbulence (≈ 10 km and k^{-3}). A simple explanation is that the aircraft trajectories are gently sloping (e.g. they are isobaric) so that at a critical scale, the vertical fluctuations are dominant implying $k^{-2.4}$ for the sloping spectra (as in the vertical). In order to test this directly, high accuracy altitude and wind measurements are required; when carefully used the TAMDAR commercial aircraft sensors are adequate. However, due to degraded

vertical resolution on ascending and descending flight segments, only cruise altitude data should be used and stringent pressure and altitude bounds are needed to define the isoheights and isobars (±10 m, ±0.63 hPa).

Using data from over 14500 flights, for the first time we were able to estimate the joint horizontal-vertical structure functions providing strong support to the 23/9D anisotropic scaling theory (Figure 2.1), and estimating the key stratification exponent as H_z=0.57±0.02, quite close to the theoretical value 5/9. Using this, and the observed fractal dimension of the isobars (D_{tr}=1.79±0.02), we were able to theoretically calculate the isoheight, isobaric and constant slope structure function exponents (0.8, 1.1, 1.4 respectively) as well as the critical isoheight/isobar transition distance (≈160 km, 125 km, transverse, longitudinal). The results of this study give the strongest and most direct support to date for the 23/9D anisotropic scaling model.

Chapter 3: The Horizontal Space-Time Scaling and Cascade Structure of the Atmosphere and Satellite Radiances

The following reproduces the article "Pinel, J., S. Lovejoy, D. Schertzer, (2013): The horizontal space-time scaling and cascade structure of the atmosphere and satellite radiances" submitted to **Atmospheric Research** in February 2013. It presents the first study of the consequences of the anisotropic spatial scaling (addressed in the previous chapter) on the statistics in the full horizontal space-time domain.

Abstract

Even today, there is still no agreement about the space-time statistical properties of the atmosphere. Classically, spatial statistics have been modelled by a hierarchy of different isotropic scaling regimes. However, gravity acts at all scales and theory and observations now point towards an atmosphere described by a single anisotropic scaling regime where two different scaling laws apply in the horizontal and vertical; the 23/9D turbulence model. However, the implications of this anisotropic spatial scaling for the full space-time scaling are not clear and are the subject of this paper. By considering that small structures are advected by larger turbulent structures and by considering averages over the latter we approximate the structure functions and spectra with the help of scale functions. In order to test these predictions, we analyze geostationary satellite MTSAT data which provide wide scale ranges in both horizontal space and time (5 km to ~10000 km, 1 hour to 2 months). We found that our model could accurately reproduce the 3D (k_x, k_y, ω) spectral density over the range 1 hour to ≈2 weeks and 30 km to ≈13000 km. The 1D spectral exponents were the same in the 3 space-time directions (i.e horizontal space-time isotropy for the exponents), with β~1.55±0.01, comparable to the passive scalar, Corrsin-Obukhov value with intermittent corrections (β=5/3-K(2)≈1.55±0.01)). To obtain a more complete description of the statistics, we found that we can describe atmospheric radiances turbulent flux statistics (including TRMM's infrared and passive microwave over scale ranges 100 km to 20000 km, 1 day to 1 year) by a multiplicative cascade model over large ranges of spatial scales with typically slight deviations at small and

large scales. Analogous temporal analyses showed similar agreement at small scales, but with significant deviations at scales larger than a few days (2 to 14 days), marking two regimes, associated with weather and climate. This allows us to find a statistical relation between typical sizes of structures and their lifetimes - relation expressed by an effective velocity - that characterizes the space-time statistics.

3.1 Introduction

Turbulent flows have long been recognized for their complexity, randomness and myriad of structures of different sizes and lifetimes. Typically, one describes the statistics of the corresponding fluctuations with the help of scaling laws. For instance, the celebrated Kolmogorov law [*Kolmogorov*, 1941] describes how turbulent mean wind fluctuations change with scale. In real space, this law has the form: $\Delta v = \varepsilon^{1/3} \Delta x^H$ where Δv is a fluctuation in the turbulent horizontal wind field v, Δx the spatial separation over which Δv is calculated, H is the mean fluctuation scaling exponent and ε is the flux of energy from large to small scales. The Kolmogorov law applies to statistically isotropic turbulence in three spatial dimensions and the classical arguments based on the energy flux yield H=1/3. We can also express these laws in Fourier space where (neglecting intermittency) they follow $E(k) = \varepsilon^{2/3} k^{-\beta}$ where $E(k)$ is the power spectrum of the turbulent field, k the wavenumber and $\beta = 1 + 2H$, hence the famous "5/3 law".

If we attempt to apply the Kolmogorov law to the atmosphere, a basic question that must be addressed is the stratification due to gravity which introduces anisotropy at all scales. Either the stratification breaks the scaling somewhere near the atmospheric scale height (~10 km) allowing the law to hold at least approximately over smaller scales, or alternatively, the isotropic laws are always poor approximations and new laws are required. Indeed, empirical evidence points towards the latter: a spatially anisotropic scaling atmosphere (see the review by *Lovejoy and Schertzer* [2010; 2013]). In this model, the turbulence is never isotropic so that (even ignoring intermittency) the Kolmogorov law never holds, nevertheless, the energy flux and Kolmogorov exponent govern the horizontal statistics (from the small dissipation scale (~1 mm) up to the largest, planetary scales. In the vertical, the buoyancy variance flux with a different

exponent - the Bolgiano-Obukhov exponent - is relevant: H_v=3/5 (or β_v =11/5) (Bolgiano, 1959 ; Obukhov, 1959), leading to overall 23/9D turbulence, intermediate between flat (2D) and isotropic (3D) turbulence [*Schertzer and Lovejoy*, 1985a]. This model thus has a single anisotropic scaling regime describing the stratification of turbulent structures in the atmosphere, from millimeters to planetary scales.

This 23/9D model provoked a debate [*Lovejoy et al.*, 2009a; *Lindborg et al.*, 2009, 2010; *Lovejoy et al.*, 2009b, 2009c, 2010; *Schertzer et al.*, 2011; *Yano*, 2009; *Frehlich and Sharman*, 2010] followed by the recent [*Pinel et al.*, 2012, i.e. Chapter 2] re-evaluation of commercial aircraft measurements, and the derivation [*Schertzer et al.*, 2012] of fractional vorticity equations respecting anisotropic scaling symmetries. The latter provide respectively empirical and theoretical arguments in favor of the 23/9D model that are difficult to refute. This raises the question: if the spatial structures do indeed respect anisotropic scaling, what are the implications for the temporal evolution, i.e. the full space-time scaling? Since (x, y, z, t) data sets spanning significant ranges of scales are not available we consider the simpler problem: what are the horizontal-temporal statistics ?

Although our goal is to understand Eulerian (fixed frame) statistics, first recall that a general feature of turbulent flows is that there exists a statistical relation between size of structures and their lifetime (their "eddy turnover time"); for Kolmogorov turbulence this is $\Delta v = \varepsilon^{1/2} \Delta t^{H_\tau}$ with H_τ=1/2. This is a Lagrangian relation which is used conceptually in meteorology in constructing space-time "Stommel" diagrams but has generally not been directly calculated empirically, (see e.g. Dias et al., 2012). In this paper, instead we estimate the corresponding Eulerian space-time relationships. A classical way to obtain Eulerian statistics is to consider the case when the turbulent fluctuations are sufficiently small compared to an imposed mean flow, such that a clear scale separation exists, Taylor's hypothesis of "frozen turbulence" developed for wind tunnels experiments [*Taylor*, 1938] can then be used. In this case, a constant (mean flow) velocity V relates temporal to spatial statistics so that $\Delta v = \varepsilon^{1/3} \left(V \Delta t \right)^{1/3}$ so that H_τ=1/3 (or β_τ=5/3). However, in the atmosphere, we have argued that no scale separation exists so that another model for space-time scaling is needed.

Rather than assuming a scale separation, *Tennekes* [1975] argued that in the Eulerian framework, for a flow with negligible externally imposed mean velocity, the turbulent eddies would "sweep" the small eddies. The largest eddies with largest velocities V_e would dominate so that $\Delta v \sim (V_e \Delta t)^{1/3}$ and thus H_τ=1/3 so that the Eulerian exponent would be different from the Lagrangian one. On the empirical side, *Radkevich et al.* [2008] found support for this by analyzing passive scalar concentrations in the atmosphere (using lidar backscatter as surrogate), finding values of H_τ mostly ≈1/3 but occasionally ≈1/2. It was argued that the latter values were consequences of the vertical wind dominating the statistics, not a manifestation of the Lagrangian exponent [*Lovejoy et al.*, 2008].

Unfortunately, full (3D) space-time data with wide ranges of scale are not available and reanalyses have limitations - due amongst other reasons - to the use of the hydrostatic approximation; see [*Stolle et al.*, 2010, 2012]. Therefore, to better understand the horizontal Eulerian statistics, we present a spectral study of the space-time scaling of atmospheric variability and its (horizontal) space-time statistical relations, using infrared radiances measured by geostationary satellite Multi-Functional Transport Satellite (MTSAT). These infrared radiances are probably the best data currently available for this task as they cover wide scale ranges in both space and time (5 km to ~10000 km, 1hour to months, years) and they don't suffer from significant sensor remapping issues. The use of passive thermal emission bands or active sensing is necessary to avoid strong diurnal effects. In comparison, planetary scale active sensors (satellite-borne radars and lidars) have low temporal resolutions with return times of days for existing systems. We therefore consider thermal IR from a geostationary satellite which is the best available for the purpose. Nevertheless, along with MTSAT data, we also analyzed infrared and passive microwave radiances measured by the Tropical Rainfall Measuring Mission (TRMM) orbiting satellite whose sampling protocol is not conveniently adapted for temporal spectral analysis but still allows us to investigate the intermittency.

On the theoretical side, we use a concrete anisotropic scaling model based on multiplicative cascades (see below) to interpret the results. Section 2 presents a review of the model. In section 3, we present the results of the spectral study made on MTSAT IR data. Section 4 presents an application of our method in understanding the Atmospheric

Motion Vectors which are used to estimate the wind. In addition to the spectral analysis, we also present a more detailed investigation of the scaling behaviour of the atmosphere and its space-time statistical relations by examining its intermittency (Section 5).

3.2 Review and development of the anisotropic scaling model

3.2.1 Anisotropic scaling in real space

If the turbulent field I has anisotropic space-time scaling, then for each space-time direction:

$$\Delta I(\Delta x) = \varphi_h \, \Delta x^{H_h} \tag{3.1}$$

$$\Delta I(\Delta y) = \varphi_h \, \Delta y^{H_h}$$

$$\Delta I(\Delta z) = \varphi_v \, \Delta z^{H_v}$$

$$\Delta I(\Delta t) = \varphi_\tau \, \Delta t^{H_\tau}$$

where ΔI is a fluctuation in a turbulent field I, φ's are scale by scale conserved turbulent fluxes, Δx, Δy and Δz are the spatial (or temporal) scales over which ΔI is estimated and H is the "non conservation" or "mean fluctuation" exponent. As in the case of the horizontal velocity, equation (3.1) assumes unique horizontal, vertical and temporal exponents H_h and H_v, H_τ. If I is a horizontal wind component, we have already described how arguments from classical turbulence theory and dimensional analysis yield for isotropic 3D turbulence: $\varphi_h=\varepsilon^{1/3}$, H_h=1/3 and $\varphi_\tau=\varepsilon^{1/2}$, H_τ=1/2. *Schertzer and Lovejoy* [1985a] proposed that in the vertical, the scaling exponent H_v =3/5 on the assumption that a different quadratic invariant: the buoyancy variance flux ϕ ($\varphi_v=\phi^{1/5}$) dominated the dynamics; see [Lovejoy et al., 2007) for empirical confirmation using drop sondes. This value was proposed by *Bolgiano*, [1959] and *Obukhov*, [1959] for the isotropic buoyancy subrange. Analogous laws for passive scalar concentrations ρ can be obtained by making the following change: $\varepsilon \to \chi^{3/2}\varepsilon^{-1/2}$ where χ is the passive scalar variance flux.

The way to combine these laws for any space-time vector displacements is described by *Schertzer and Lovejoy*, [1985b], using the formalism of "Generalized Scale Invariance". It consists in replacing the usual vector norm for the space-time increments

by a different measure of scale - the scale function $[\![\underline{\Delta R}]\!]$ - that takes into account the anisotropy. A simple example of such a "canonical" scale function is:

$$\Delta I(\underline{\Delta R}) = \varphi_{h,[\![\underline{\Delta R}]\!]}\,[\![\underline{\Delta R}]\!]^{H_h}; \qquad (3.2)$$

$$[\![\underline{\Delta R}]\!] = L_w \left\{ \left(\frac{\Delta x}{L_w}\right)^2 + \left(\frac{\Delta y}{L_w}\right)^2 + \lambda_s^{2(1/H_z-1)} \left(\frac{\Delta z}{L_w}\right)^{2/H_z} + \left(\frac{\Delta t}{\tau_w}\right)^{2/H_t} \right\}^{1/2}$$

where $\underline{\Delta R}=(\underline{\Delta r}, \Delta t)$ with $\underline{\Delta r}=(\Delta x, \Delta y, \Delta z)$; L_w is a convenient reference scale (see below), of the order of the size of the Earth (L_e=20000 km) and $\tau_w=\varepsilon^{-1/3}L_w^{2/3}$ is the corresponding duration, the lifetime planetary scale structures; the subscript "w" is for "weather". $\varphi_{h,[\![\underline{\Delta R}]\!]}$ is the turbulent flux governing the dynamics in the horizontal at resolution $[\![\underline{\Delta R}]\!]$ and $\lambda_s=L_w/l_s$ where $l_s=\phi^{-3/4}\varepsilon^{5/4}$ is the "sphero-scale" (i.e. the scale at which structures in the vertical plane are roughly roundish). Here we introduced the exponents $H_z=H_h/H_v$, $H_t=H_h/H_\tau$ that characterize the vertical/horizontal and (horizontal) space-time stratifications. For the wind and passive scalars, H_h=1/3, H_v=3/5, H_τ=1/2 and H_z=5/9, H_t=2/3. Note that the temporal exponents are Lagrangian, not Eulerian; equation (3.2) assumes no mean advection. When $\underline{\Delta r}$ is aligned with one of the axes in our coordinate system, (e.g. $\underline{\Delta R}=(\Delta x, 0, 0,0)$), we retrieve equation (3.1) for that particular direction. Using the scale function, taking the q^{th} order moments and averaging, the statistics of the space-time fluctuation $\Delta I(\underline{\Delta R})$ follow:

$$\left\langle \left|\Delta I(\underline{\Delta R})\right|^q \right\rangle = \left\langle \varphi^q_{[\![\underline{\Delta R}]\!]} \right\rangle [\![\underline{\Delta R}]\!]^{qH_h} \propto [\![\underline{\Delta R}]\!]^{\xi(q)}; \qquad (3.3)$$

$$\left\langle \varphi^q_{[\![\underline{\Delta R}]\!]} \right\rangle = \left(\frac{L_w}{[\![\underline{\Delta R}]\!]}\right)^{K(q)}; \qquad \xi(q) = qH - K(q)$$

where the function $K(q)$ takes into account the intermittency of the flux φ and yields the overall structure function exponent $\xi(q)$ as indicated. Its statistical behaviour is determined by multiplicative cascades whose external scale is L_w and which we discuss in section 5.

The scale function (equation (3.2)) uses only the Lagrangian temporal scaling; it ignores advection. In the Eulerian frame, we also need to take into account the mean

advection of structures. For a fixed advection velocity $\underline{v}=(v_x, v_y, v_z)$, we can use the Galilean transformation $\underline{r}\rightarrow\underline{r}-\underline{v}t$; $t\rightarrow t$, to obtain:

$$\left[\!\left[\underline{\Delta R}\right]\!\right] = L_w \left\{ \left(\frac{\Delta x - v_x \Delta t}{L_w} \right)^2 + \left(\frac{\Delta y - v_y \Delta t}{\left(L_w / a\right)} \right)^2 + \lambda_s^{2(1/H_z - 1)} \left(\frac{\Delta z - v_z \Delta t}{L_w} \right)^{2/H_z} + \left(\frac{\Delta t}{\tau_w} \right)^{2/H_t} \right\}^{1/2} \quad (3.4)$$

where we also introduced a, a parameter that describes the possible trivial (scale independent) zonal/meridional anisotropy in the horizontal spatial plane.

The basic problem now is that equation (3.4) holds only for a fixed, constant and uniform advection $\underline{v}$ whereas the actual $\underline{v}$ is a turbulent field, i.e. we must consider an "effective" scale function that takes into account the turbulence. The situation is complicated by the fact that at fixed location (i.e. $\Delta x=\Delta y=\Delta z=0$), there are four temporal terms and each can in principle be dominant depending on the $\underline{v}$ field. In [*Lovejoy et al.*, 2008 ; *Radkevich et al.*, 2008], it was argued that sometimes the vertical wind can dominate the statistics of the horizontal wind, producing $\Delta v \approx \Delta t^H$ with $H\approx 0.5$ scaling. To see how this might arise, take $\Delta z=0$, so that the vertical term in equation (3.4) is $\propto \left(v_z \Delta t\right)^{1/H_z}$. Unlike the horizontal wind, the vertical wind has typically small values and follows $\left|v_z\right| \propto \Delta t^{H_{v_z}}$ with $H_{v_z} \sim -0.2$. From equation (3.4), taking $H_z=5/9$ and neglecting the intermittency, we find: $\left[\!\left[(0,0,0,\Delta t)\right]\!\right] \propto \Delta t^{H_{v_z}/H_z} = \Delta t^{1/H_{\tau,eff}}$ with $H_{\tau,eff}=0.7\sim H_t=2/3$; hence $\Delta v \sim \Delta t^{0.5}$ scaling when this vertical term is dominant. In the following, we consider only satellite radiance fields, which are (x, y, t) fields. The consequence of the vertical wind on the radiances is therefore quite different. Since our field is horizontal, we take $\underline{\Delta R}=(\underline{\Delta r}, \Delta t)$ where $\underline{\Delta r}=(\Delta x, \Delta y)$, so that for constant advection $\underline{v} = \left(v_x, v_y\right)$, (i.e. $v_z=0$ in equation (3.4)) we have:

$$\left[\!\left[\underline{\Delta R}\right]\!\right]_{advec} = L_w \left\{ \left(\frac{\Delta x - v_x \Delta t}{L_w} \right)^2 + \left(\frac{\Delta y - v_y \Delta t}{\left(L_w / a\right)} \right)^2 + \left(\frac{\Delta t}{\tau_w} \right)^{2/H_t} \right\}^{1/2} \quad (3.5)$$

However, as argued by *Tennekes*, [1975], the largest eddies with speed $V_w = L_w / \tau_w$ advect all the others so that the "effective" Eulerian scale function will involve averages over v's ranging up to V_w. Using this in equation (3.5) for v_x and

ignoring v_y, we see that whenever $\Delta t < \tau_w$, the corresponding advection term $\left|\frac{V_w \Delta t}{L_w}\right| = \left|\frac{\Delta t}{\tau_w}\right|$ will dominate the temporal scaling term $\left|\frac{\Delta t}{\tau_w}\right|^{1/H_t} = \left|\frac{\Delta t}{\tau_w}\right|^{3/2}$. Indeed, as argued by *Radkevich et al.* [2007] using meteorological analyses from a component of the operational Canadian Meteorological Centre Global Environmental Multiscale (GEM) model, the empirical probability that the transition scale - from horizontal advection scaling to pure time evolution scaling - is shorter than τ_w (~10 days) is low, hence we drop the Lagrangian term. There will be two main effects of the turbulence on the scale function equation (3.5). The first is the advection by the mean $\underline{v}$, the second is to determine the space-time relationship given by the typical turbulent velocity, which is conveniently estimated from its variance. The two effects can be conveniently understood by considering the square of the scale function:

$$\left[\!\left[\underline{\Delta R}\right]\!\right]^2_{advec} = L_w^2 \left\{ \left(\frac{\Delta x - v_x \Delta t}{L_w} \right)^2 + \left(\frac{\Delta y - v_y \Delta t}{\left(L_w / a \right)} \right)^2 \right\} \tag{3.6}$$

$$= L_w^2 \left\{ \left(\frac{\Delta x}{L_w} \right)^2 + \left(\frac{a\, \Delta y}{L_w} \right)^2 + \left(\frac{{v_x}^2 + a^2\, {v_y}^2}{L_w^2} \right) \Delta t^2 - 2 \left(\frac{v_x \Delta x}{L_w} + \frac{a^2 v_y \Delta y}{L_w} \right) \left(\frac{\Delta t}{L_w} \right) \right\}$$

Averaging this over the turbulence, we obtain:

$$\left[\!\left[\widehat{\underline{\Delta R}}\right]\!\right] = \widehat{\underline{\Delta R}}^T \, \underline{\underline{B}} \, \widehat{\underline{\Delta R}} \tag{3.7}$$

where $\widehat{\underline{\Delta R}} = \left(\widehat{\Delta x}, \widehat{\Delta y}, \widehat{\Delta t} \right)$, (not to be confused with unit a vector) and

$$\underline{\underline{B}} = \begin{pmatrix} 1 & 0 & -\mu_x \\ 0 & a^2 & -a^2 \mu_y \\ -\mu_x & -a^2 \mu_y & 1 \end{pmatrix} \tag{3.8}$$

where we have used the dimensionless parameters :

$$\widehat{\Delta x} = \frac{\Delta x}{L_w}; \qquad \widehat{\Delta y} = \frac{a\, \Delta y}{L_w}; \qquad \widehat{\Delta t} = \frac{\Delta t}{\tau_w};$$

$$\mu_x = \frac{\overline{v_x}}{V_w}; \qquad \mu_y = \frac{\overline{v_y}}{V_w}; \qquad \underline{\mu} = (\mu_x, \mu_y) \tag{3.9}$$

and $\underline{v} = (v_x, v_y) \rightarrow \bar{\underline{v}} = (\overline{v_x}, \overline{v_y})$ and $V_w = \left(v_x{}^2 + a^2 v_y{}^2\right)^{1/2} \rightarrow V_w = \left(\overline{v_x^2} + a^2 \overline{v_y^2}\right)^{1/2}$ where $\bar{\underline{v}}$ is the overall mean advection in the region studied and V_w is a large-scale turbulent velocity; $\overline{v^2}$ is the mean square. Note that since $\overline{v^2} > \bar{v}^2$, $|\mu_{x,y}| < 1$. These results are generalizations of those presented by *Lovejoy and Schertzer* [2010].

3.2.2 Anisotropic scaling in Fourier space

If the increments in a turbulent field *I* are described by the scaling equation (3.3), then, we expect the spectral density $P(\underline{K})$ to be scaling as well, but with a different (Fourier space) scale function ($[\![\underline{K}]\!]_F$). To derive this, we start from the general relation between structure functions and spectra (a corollary of the Wiener-Khintchin theorem):

$$\left\langle |\Delta I(\underline{\Delta R})|^2 \right\rangle = 2 \int d\underline{K}\, (1 - e^{i\underline{K}\cdot\underline{\Delta R}}) P(\underline{K}) \qquad (3.10)$$

with $\underline{K} = (k_x, k_y, \omega)$; the *k*'s being the wavenumbers in the horizontal plane and ω the frequency. In order to determine the form of $[\![\underline{K}]\!]_F$, we define the dimensionless wave vector: $\underline{\hat{K}} = (\hat{k}_x, \hat{k}_y, \hat{\omega}) = (L_w k_x, L_w k_y, \tau_w \omega)$ and use the relation:

$$\left|\underline{\widehat{\Delta R}}\right|^{\zeta(2)} = 2 \int \left|\underline{\hat{K}}\right|^{-(D+\zeta(2))} \left(1 - e^{i\underline{\hat{K}}\cdot\underline{\widehat{\Delta R}}}\right) d\underline{\hat{K}} \qquad (3.11)$$

where |.| is the usual vector norm. Equations (3.10) and (3.11) state that, if the integral converges and the (isotropic) spectral density obeys a scaling behaviour (i.e. $P(\underline{K}) \sim \left|\underline{\hat{K}}\right|^{-s}$), then $\left|\underline{\widehat{\Delta R}}\right|$ is scaling as well and their scaling exponents are related by s=ξ(2)+d (with d=3). For real fields, the scaling is always only valid for a finite range of scales and the corresponding truncated integral always converges. If we make the change of variable $\underline{\hat{K}} \rightarrow \underline{\underline{C}}^{-1} \underline{\hat{K}}$, (with $\underline{\underline{C}}^{-1}$ a real matrix), we obtain:

$$\left\langle |\Delta I(\underline{\Delta R})|^2 \right\rangle \sim [\![\underline{\Delta R}]\!]^{\xi(2)} \leftrightarrow P(\underline{K}) = \left\langle \left|\tilde{I}(\underline{K})\right|^2 \right\rangle \sim [\![\underline{K}]\!]_F^{-s}; \qquad s=\xi(2)+3 \qquad (3.12)$$

$$[\![\underline{\widehat{\Delta R}}]\!] = \left(\underline{\widehat{\Delta R}}^T \underline{\underline{B}}\, \underline{\widehat{\Delta R}}\right)^{1/2} \leftrightarrow [\![\underline{\hat{K}}]\!]_F = \left(\underline{\hat{K}}^T \underline{\underline{B}}^{-1} \underline{\hat{K}}\right)^{1/2}; \qquad \underline{\underline{B}} = \underline{\underline{C}}\,\underline{\underline{C}}^T \; ; \quad \det(\underline{\underline{B}}) > 0$$

with:

$$\underline{\underline{B}}^{-1} = \frac{1}{1-\mu_x^2-a^2\mu_y^2}\begin{pmatrix} 1-a^2\mu_y^2 & \mu_x\mu_y & \mu_x \\ \mu_x\mu_y & (1-\mu_x^2)/a^2 & \mu_y \\ \mu_x & \mu_y & 1 \end{pmatrix} \tag{3.13}$$

from equation (3.8). The result for $\det\left(\underline{\underline{B}}\right) < 0$ cannot be obtained from this approach and has qualitatively different behaviour [see *Lovejoy and Schertzer*, 2013; *Pinel and Lovejoy*, 2013, (i.e. Chapter 4)]. Since $\det\left(\underline{\underline{B}}\right) = a^2\left(1-\mu_x^2-a^2\mu_y^2\right)$, $\det\left(\underline{\underline{B}}\right) > 0$ when $\mu_x^2 + a^2\mu_y^2 < 1$, a condition which is always satisfied here. Notice that we introduced the exponent ξ(2) in equation (3.11) that takes into account the non-conservation exponent *H* as well as the second order intermittency correction (see below).

We can further simplify the form of $\left[\!\left[\underline{\widehat{K}}\right]\!\right]_F$ by introducing:

$$\mu_x' = \frac{\mu_x}{\left\{1-\left(\mu_x^2+a^2\mu_y^2\right)\right\}} \;; \qquad \mu_y' = \frac{\mu_y}{\left\{1-\left(\mu_x^2+a^2\mu_y^2\right)\right\}};$$

$$\widehat{\omega'} = \frac{\widehat{\omega}}{\left\{1-\left(\mu_x^2+a^2\mu_y^2\right)\right\}} \tag{3.14}$$

to obtain :

$$\left[\!\left[\underline{\widehat{K}}\right]\!\right]_F = \left(\underline{\widehat{K}}^T\,\underline{\underline{B}}^{-1}\underline{\widehat{K}}\right)^{1/2} = \left\{\left(\widehat{\omega'}+\underline{\hat{k}}\cdot\underline{\mu'}\right)^2 + \hat{k}_x^2 + \left(\hat{k}_y/a\right)^2\right\}^{1/2} \tag{3.15}$$

with $\underline{\hat{k}} = \left(\hat{k}_x, \hat{k}_y\right)$ and the final expression for the spectral density:

$$P(\underline{\widehat{K}}) \sim P_0\left[\!\left[\underline{\widehat{K}}\right]\!\right]^{-s} = P_0\left\{\left(\widehat{\omega}' + \underline{\hat{k}}\cdot\underline{\mu'}\right)^2 + \left\|\underline{\hat{k}}\right\|^2\right\}^{-s/2} \tag{3.16}$$

where P_0 is a dimensional constant and $\left\|\underline{\hat{k}}\right\| = \left(\hat{k}_x^2 + \hat{k}_y^2/a^2\right)^{1/2}$ is a Fourier spatial scale function. Note that we can express the parameters: $\mu_x' = \frac{\overline{v_x}}{\sigma_v}$; $\mu_y' = \frac{\overline{v_y}}{\sigma_v}$ with $\sigma_v^2 = \left(\overline{v_x^2} - \overline{v_x}^2\right) - a^2\left(\overline{v_y^2} - \overline{v_y}^2\right)$ so that $\frac{\mu_x'}{\mu_x} = \frac{\mu_y'}{\mu_y} = \frac{V_e}{\sigma_v}$; the parameter $\underline{\mu'}$ being directly related to the mean advection.

Directly testing the prediction that the horizontal space-time spectral density is of the form of equation (3.12) is unwieldy; it is more convenient to consider various 2D and 1D subspaces, obtained by successively integrating out $\hat{k}_x, \hat{k}_y, \hat{\omega}$ in $P(\underline{\hat{K}}) = P_{xyt}\left(\hat{k}_x, \hat{k}_y, \hat{\omega}\right)$. To do this, we use the Wiener-Khintchin theorem that relates the autocorrelation function to the spectral density:

$$R(\Delta x, \Delta y, \Delta t) = (2\pi)^{-3} \int P\left(\hat{k}_x, \hat{k}_y, \hat{\omega}\right) e^{i(\hat{k}_x \Delta x + \hat{k}_y \Delta y + \hat{\omega}\Delta t)} d\hat{k}_x d\hat{k}_y d\hat{\omega} \tag{3.17}$$

If we successively put Δx=0, Δy=0, Δt=0, we obtain:

$$R(\Delta x, \Delta y, 0) = (2\pi)^{-2} \int P_{xy}\left(\hat{k}_x, \hat{k}_y\right) e^{i(\hat{k}_x \Delta x + \hat{k}_y \Delta y)} d\hat{k}_x d\hat{k}_y \; ; \quad P_{xy}\left(\hat{k}_x, \hat{k}_y\right) = \int P\left(\hat{k}_x, \hat{k}_y, \hat{\omega}\right) d\hat{\omega} \; ;$$

$$R(\Delta x, 0, \Delta t) = (2\pi)^{-2} \int P_{xt}\left(\hat{k}_x, \hat{\omega}\right) e^{i(\hat{k}_x \Delta x + \hat{\omega}\Delta t)} d\hat{k}_x d\hat{\omega} \; ; \quad P_{xt}\left(\hat{k}_x, \hat{\omega}\right) = \int P\left(\hat{k}_x, \hat{k}_y, \hat{\omega}\right) d\hat{k}_y$$

$$R(0, \Delta y, \Delta t) = (2\pi)^{-2} \int P_{yt}\left(\hat{k}_y, \hat{\omega}\right) e^{i(\hat{k}_y \Delta y + \hat{\omega}\Delta t)} d\hat{k}_y d\hat{\omega} ; \quad P_{yt}\left(\hat{k}_y, \hat{\omega}\right) = \int P\left(\hat{k}_x, \hat{k}_y, \hat{\omega}\right) d\hat{k}_x \tag{3.18}$$

From equation (3.18) and developments similar to equations (3.11)-(3.13), we find:

$$P_{xy}\left(\hat{k}_x, \hat{k}_y\right) \sim \left\|\left(\hat{k}_x, \hat{k}_y\right)\right\|_{xy}^{-(s-1)} \; ; \qquad P_{xt}\left(\hat{k}_x, \hat{\omega}\right) \sim \left\|\left(\hat{k}_x, \hat{\omega}\right)\right\|_{xt}^{-(s-1)} \tag{3.19}$$

$$P_{yt}\left(\hat{k}_y, \hat{\omega}\right) \sim \left\|\left(\hat{k}_y, \hat{\omega}\right)\right\|_{yt}^{-(s-1)}$$

with:

$$\left\|\left(\hat{k}_x, \hat{k}_y\right)\right\|_{xy}^2 = \hat{k}_x^2 + a^{-2}\hat{k}_y^2 \tag{3.20}$$

$$\left\|\left(\hat{k}_x, \hat{\omega}\right)\right\|_{xt}^2 = \left(\hat{\omega}'_x + \hat{k}_x \mu''_x\right)^2 + \hat{k}_x^2 \; ; \qquad \mu''_x = \frac{\overline{v_x}}{\left(\sigma_v^2 + a^2\left(\overline{v_y}\right)^2\right)^{1/2}} = \frac{\mu'_x}{\left(1 + a^2 \mu'^2_y\right)^{1/2}}$$

$$\hat{\omega}'_x = \frac{\hat{\omega}}{\left(1 - \mu_x^2\right)^{1/2}} \; ;$$

$$\left\|\left(\hat{k}_y, \widehat{\omega}\right)\right\|_{yt}^2 = \left(\widehat{\omega_y'} + \hat{k}_y \mu_y''\right)^2 + \hat{k}_y^2 \;; \qquad \mu_y'' = \frac{\overline{v_y}}{\left(\sigma_v^2 + \left(\overline{v_x}\right)^2\right)^{1/2}} = \frac{\mu_y'}{\left(1+\mu_x'^2\right)^{1/2}} \quad ;$$

$$\widehat{\omega_y'} = \frac{\widehat{\omega}}{\left(1 - a^2 \mu_y^2\right)^{1/2}}$$

Similarly, for the 1D subspaces, we obtain:

$$E_x(\hat{k}_x) = \int P\left(\hat{k}_x, \hat{k}_y, \widehat{\omega}\right) d\widehat{\omega}\, d\hat{k}_y \sim \hat{k}_x^{-\beta}; \qquad \beta = s - 2 \tag{3.21}$$

$$E_y(\hat{k}_y) = \int P\left(\hat{k}_x, \hat{k}_y, \widehat{\omega}\right) d\widehat{\omega}\, d\hat{k}_x \sim \hat{k}_y^{-\beta}$$

$$E_t(\widehat{\omega}) = \int P\left(\hat{k}_x, \hat{k}_y, \widehat{\omega}\right) d\hat{k}_x\, d\hat{k}_y \sim \widehat{\omega}^{-\beta}$$

3.3 MTSAT spectra

We now test the spectrum equation (3.16) with infrared radiance data measured by the MTSAT satellites which are a series of geostationary weather satellites operated by the Japan Meteorological Agency. MTSAT-1R, the first of the series, was launched in 2005 and replaced the older series of Geostationary Meteorological Satellites (GMS, also called "Himawari", operational since 1977). It measures radiances from the region centered on longitude 140° East (Japan, tropical western Pacific, Australia) over five channels: one visible (0.55-0.90 μm), four infrared (10.3-11.3 μm ; 11.5-12.5 μm ; 6.5-7.0 μm and 3.5-4.0 μm). MTSAT-1R has a maximal resolution of 1 km (visible) and 4 km (infrared) at nadir. The temporal resolution is 30 minutes (above the equator) and 1 hour (full disk), [*Takeuchi et al.*, 2010; *Puschell et al.*, 2002 ; 2003].

We analysed 1386 images (~ two months of data, September and October 2007), from the first ("thermal") infrared channel (10.3-11.3 μm, sensitive to temperature at (roughly) the top of clouds) taken from the Atmospheric Radiation Measurement database that archives MTSAT-1R data at 5 km and 1 hour resolutions over latitudes 40°S - 30°N and longitudes 80°E - 200°E (see Figure 3.1). This corresponds to 1675 x 2672 pixels (north-south, east-west) covering a region 8375 by 13360 km.

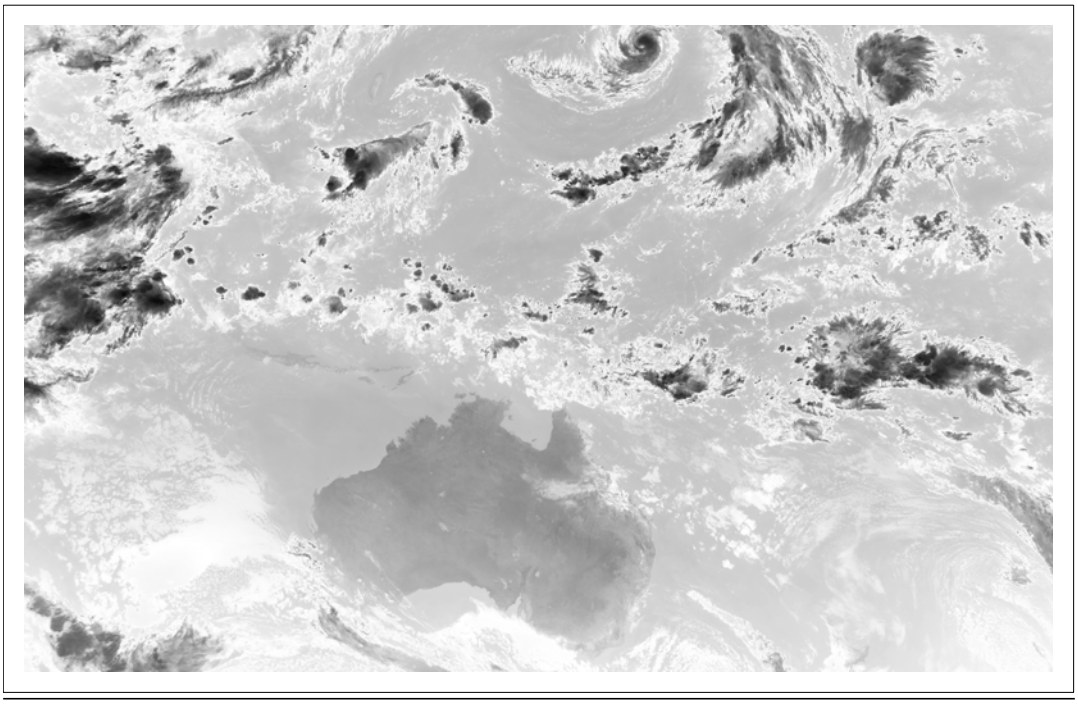

Figure 3.1: Thermal IR MTSAT-1R image taken on September 9, 2007, at 5 km resolution; between latitudes 40°S - 30°N and longitudes 80°E - 200°E. We can easily recognize the shape of Australia at the bottom and observe several examples of (presumably) cloud structures.

We separated the MTSAT sample into five 277 hr (~12 day) blocks (with resolutions, 30 km, 1 hr), calculating for each block, the spectral density on fluctuations of the field with respect to the mean image (over the 2 month period; we used a standard Hann window to reduce spectral leakage). Although the images are variable in both space and time due to the land and ocean surfaces as well as clouds, it is the latter that dominate the variability over the scales considered here. After averaging over the five blocks to improve the statistics, we compared the results to the theoretical form (equation (3.16)). Figures 3.2 and 3.3 show the comparisons between MTSAT data and a regression from equation (3.16). Because we have to determine the value of the constant P_0 in equation (3.16) from the regression, only the ratio ($V_w=L_w/\tau_w$) can be uniquely determined. We thus fixed one parameter, taking $L_w=L_e=$ 20000 km and estimated the time scale $\tau_w=L_w/V_w$. The parameters we found are (see also Table 1):

$V_w = 41\pm3$ km/h (≈1000 km/day) ; $\tau_w = L_w/V_w \sim 20\pm1$ days ; $a \sim 1.2\pm0.1$ (3.22)

$s \sim 3.4\pm0.1$; $\mu_x \sim -0.3\pm0.1$; ($\overline{v_x} \sim -12\pm4$ km/h ≈ -300 km/day) ;

$\mu_y \sim 0.10\pm0.08$; ($\overline{v_y} \sim 4\pm3$ km/h ≈ 100 km/day); $P_0 = 2.8\pm0.2$ °C^2 km^2 h

From Figure 3.2, we see that the 1D spectra are very close to power laws over the range of scales 120-5000 km in space and 3-100 hrs in time (except for diurnal cycle contributions at 12 and 24 hrs). The exponents are $\beta \sim 1.55\pm0.01$, a bit smaller than the non-intermittent passive scalar, Corrsin-Obukhov value $\beta = 5/3$, (with intermittency corrections, the latter are nearly identical, see (Lilley et al., 2008)). We thus have space-time isotropy in the spectral exponents, as predicted. However, the scaling is even better than suggested by the near linearity displayed in Figure 3.2. Indeed, we expect deviations from log-log linearity due to the space-time anisotropy coupled with our finite sample size which breaks the scaling symmetry at high and low wavenumbers/frequencies. When the integrals in equation (3.21) are performed on the discretized, numerically integrated theoretical expressions, we see (Figure 3.2) that much of the curvature at both ends of the spectra can be explained, although for spatial scales ≥ 6000 km or temporal scales longer than ~100 hrs, deviations become important. Note that the regression value $V_w = L_w/\tau_w = 41$ km/h is also consistent with the values $L_w = 5000$ km and $\tau_w = 120$ hrs (with $P_0 = 0.03$ °C^2 km^2 h), which are roughly the scales at which the scaling is broken; these are denoted L_d and τ_d for space and time respectively (table 1; see Figure 3.2 in the north-south direction, $L_w/a \approx 4300$ km).

		Spectra	Statistical Moments				
			This study			Lovejoy et al., [2009d]	
		MTSAT	MTSAT	VIRS-5	TMI-8	VIRS-5	TMI-8
Resolutions	Space (km)	30	30	100	100	8.8	13.9
	Time (hrs)	1	1	24	24	-	-
C_1		-	0.07	0.07	0.05	0.084	0.102
α		-	1.5-1.6	1.8	2	1.63	1.90
L_{eff}	E-W (km)	-	50000	25000	12600	12600 (orb. dir.)	6300 (orb. dir.)
	N-S (km)	-	32000	12600	8000		
τ_{eff}	Time (days)	-	48	57	57	-	-
L_d	E-W (km)	5000	6000	12000	5000	10000 (orb. dir.)	2500 (orb. dir.)
	N-S (km)	2500	2000	9000	2000		
τ_d	Time (days)	4	2	14	4	-	-
V	(km/day)	1000	~800	~340	~120	-	-
a		1.2	~1.35	~1.4	1.1	-	-

Table 3.1: A comparison of different parameters obtained from the spectral method (section 3) and from statistical moments (section 5) as well as results from a previous TRMM analysis in the along track direction [*Lovejoy et al.*, 2009d]. L_d and τ_d are the (large) spatial and temporal scales respectively beyond which the scaling symmetry breaks down. The speed V provides an estimate of the statistical relation between the size of structures and their lifetimes, i.e. it corresponds to V_w evaluated by the spectral method (section 3) or an averaged (north-south, est-west) V_{eff} evaluated from the cascade analysis (section 5). The parameter a from the spectral method was directly estimated from the regression while for the statistical moments, a is an averaged value from the "shifting method" and from the Eulerian Stommel diagrams (section 5.3). Generally, values of parameters obtained for MTSAT by spectral and statistical moments methods are comparable. We find small discrepancies between parameters found for MTSAT, VIRS-5 and TMI-8, even though the values of C_1 and a are comparable (except for TMI-8). Interestingly, the values of L_{eff} found in the north-south direction are comparable with those found by [*Lovejoy et al.*, 2009d] in the direction of the orbit.

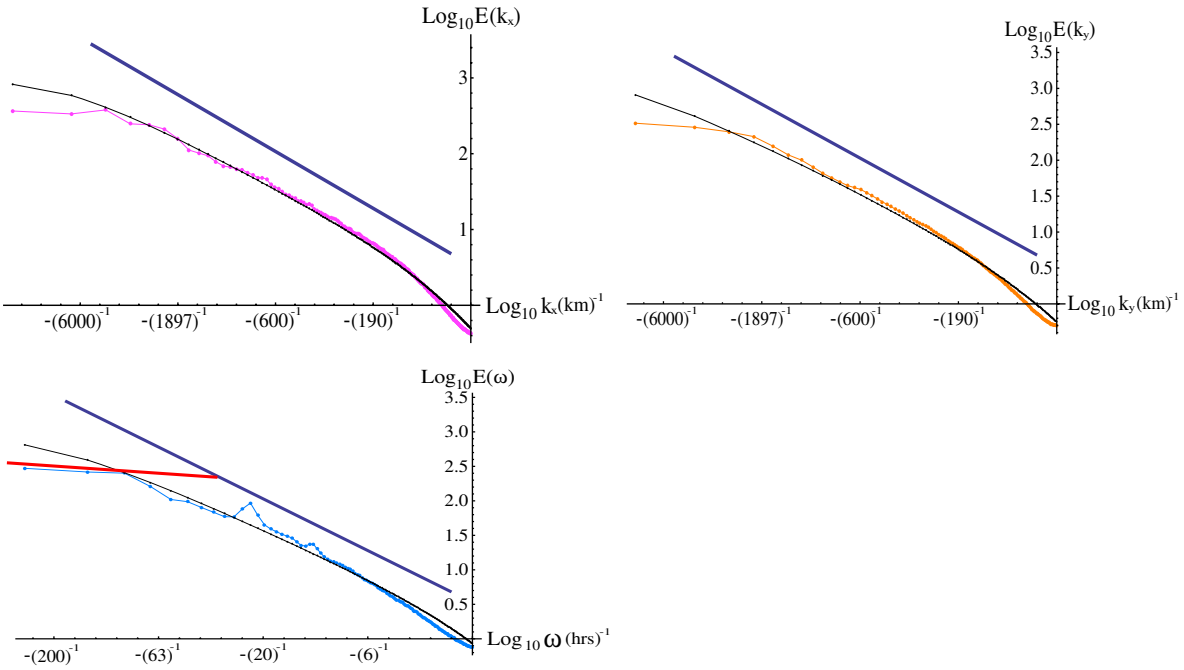

Figure 3.2: 1D spectra. In black: the theoretical spectrum using parameters estimated by regression from equation (3.16) and taking into account the finite space-time sampling volume. The parameters are: L_w~ 20000 km ; τ_w~ 20±1 days ; (V_w~L_w/τ_w= 41±3 km/h ≈1000km/day) ; a~ 1.2±0.1 ; s~ 3.4±0.1 ; μ_x~ -0.3±0.1 ; ($\overline{v}_x$ ~ -12±4 km/h ≈ -300 km/day) ; μ_y~ 0.10±0.08 ; ($\overline{v}_y$ ~ 4±3 km/h ≈ 100 km/day) ; P_0=2.8±0.2 K^2 km^2 h. In color: MTSAT thermal IR radiances. The straight lines are reference lines with slopes -1.5 (blue) and -0.2 (red). Upper left: zonal spectrum. Upper right: meridional spectrum. Bottom: temporal spectrum.

To understand the break in the temporal spectrum at large scales, we recall that there is a statistical relation between size of structures and their lifetimes. As the scaling symmetry seems to generally hold in space for scales as large as planetary scales (see the review by *Lovejoy and Schertzer*, [2010]), it was estimated by *Lovejoy and Schertzer* [2010] from "first principles" (i.e. using the energy flux due to solar radiation) and from ECMWF reanalyses that structures of planetary scale L_e have typical lifetimes of $\tau_e=\varepsilon^{-1/3}L_e^{2/3}$~10 days. It was also observed that atmospheric fields all undergo a transition in their statistics at a scale $\tau_w \approx \tau_e$, from a small scale regime ($\Delta t<\tau_w$) to a different larger scale regime ($\Delta t>\tau_w$); the two regimes having qualitatively different scaling behaviours with fluctuations growing or decreasing with scale respectively (the sign of H changed

from positive to negative at τ_w). It was proposed by *Lovejoy and Schertzer*, [2010, 2013] to identify the former regime with weather and the latter as low frequency or "macroweather", (the subscript "w" refers to "weather").

In order to investigate this more fully, we can examine 2D rather than 1D spectra (equation (3.18)). Regressions on the 2D spectra also reproduce the data relatively well, but there are still residuals (see Figure 3.3). The mean deviations between the two surfaces (for the three 2D cases shown in Figure 3.3) are of the order of ±14%, even though the signal $\left(P(\widehat{\underline{K}})\right)$ varies over ~ six orders of magnitude. The orientation of the contours of $\mathrm{Log}_{10}\mathrm{P}(k_x, \omega)$ (in zonal wavenumber/frequency subspace) is a consequence of the non zero (and relatively large) mean zonal advection $\overline{v_x}$ ~ -12±4 km/h (-300 km/day). Hence, with our contours, we can estimate the overall mean advection. The area analyzed in this paper is not perfectly symmetric with respect to the equator so that we found a small advection in the meridional direction.

The functional form equation (3.16) was derived by assuming that the structures were localized, turbulent like; however, there is a longstanding phenomenology of wavelike disturbances (localized in space but not in space-time) so that we may expect that the residual differences between the empirical and theoretical regression space may be associated largely with waves. This is the basic idea behind the technique developed by *Wheeler and Kiladis*, [1999] who also used IR radiances (although at somewhat larger space-time scales). In order to study the residual spectrum believed to be associated with waves, they removed a turbulent background. However, instead of using a theoretically motivated characterization of this turbulent component, they used an ad hoc averaging technique and estimated the wave part of the spectrum as deviations from this. The idea is then to try to identify the remaining dominant variability using dispersion relations based on classical linearized wave equations. We discuss this for MTSAT data and our anisotropic model in [*Pinel and Lovejoy*, 2013 (i.e. Chapter 4); *Lovejoy and Schertzer*, 2013] where it is argued that the waves are on the contrary an emergent phenomenon arising from strongly nonlinear but scaling dynamics.

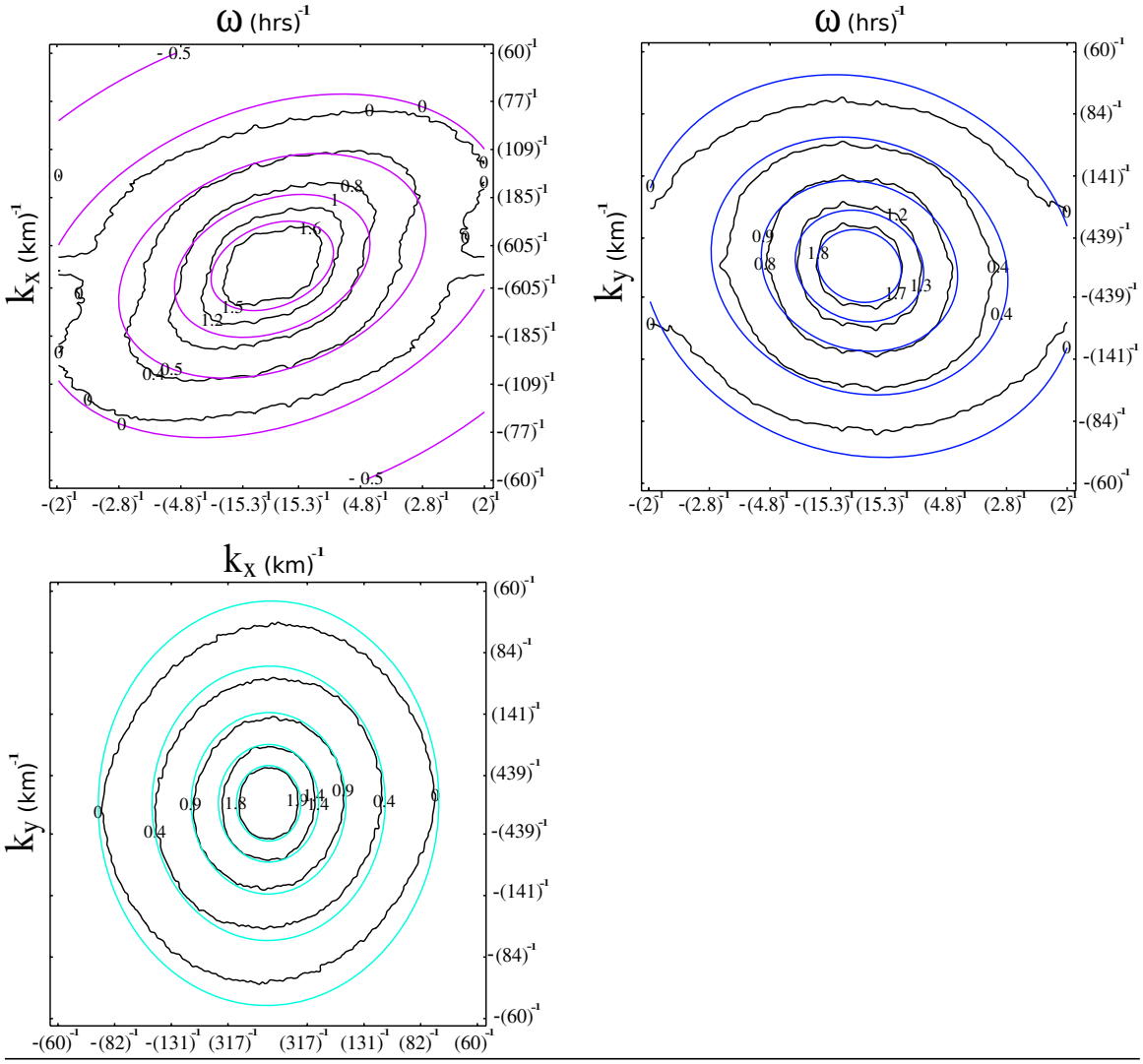

Figure 3.3: Contours of Log of spectral densities projected on to 2D subspaces. In color: the fit from theoretical expression (equation (3.16)) with parameters : L_w~ 20000 km ; τ_w~ 20 days ; (V_w~L_w/τ_w= 41±3 km/h ≈1000 km/day) ; a~ 1.2±0.1 ; s~ 3.4±0.1 ; μ_x~ -0.3±0.1 ; ($\overline{v_x}$ ~ -12±4 km/h ≈-300 km/day) ; μ_y~ 0.1±0.08 ; ($\overline{v_y}$ ~ 4±3 km/h ≈100 km/day) ; P_0=2.8±0.2 °C^2 km^2 h. In black: MTSAT thermal IR radiances. Upper left : $\mathrm{Log}_{10}P(k_x, \omega)$; zonal wavenumber/frequency subspace. Upper right: $\mathrm{Log}_{10}P(k_y, \omega)$; meridional wavenumber/frequency subspace. Bottom: $\mathrm{Log}_{10}P(k_x, k_y)$; spatial spectral density.

3.4 Application to Atmospheric Motion Vectors

As an application of the model, we now show that equation (3.16) gives a theoretical basis for extracting "Atmospheric Motion Vectors" (AMV's) from sequences of IR satellite images [*Leese et al.*, 1970 ; *Szantai and Seze*, 2008] which are used to determine cloud (or water vapour) "motion" vectors in near real-time from geostationary satellite data; these are used as surrogates for wind vectors for weather forecasting applications. Although several techniques exist to estimate AMV's, they are all variants of the maximum cross correlation technique which is based on the displacement $\underline{\Delta r}_{\max}$ which yields the maximum cross correlation between successive images. From this, the motion vector: $\underline{v}_{motion} = \dfrac{\underline{\Delta r}_{\max}}{\Delta t}$ is obtained, where Δt is the time interval between consecutive images.

We now estimate $\underline{\Delta r}_{\max}$ and $\underline{v}_{motion}$ from the structure function: $S_2(\underline{\Delta r})$ (equation (3.3) for q=2). $\underline{\Delta r}_{\max}$ can be found, from the condition on the cross-correlation function: $R(\underline{\Delta r}_{\max}, \Delta t) = \underset{\underline{\Delta r}}{max}\{R(\underline{\Delta r}, \Delta t)\}$ where $R(\underline{\Delta r}, \Delta t) = \langle I(x,y,t) I(x+\Delta x, y+\Delta y, t+\Delta t) \rangle$

(3.23)

Using $R(\underline{\Delta r}, \Delta t) = R(0,0) - \dfrac{1}{2} S_2(\underline{\Delta r}, \Delta t)$, we can derive $\underline{v}_{motion}$ in terms of the matrix $\underline{\underline{B}}$ as follows. Both functions follow $\underset{\underline{\Delta r}}{max}\{R\left(\widehat{\underline{\Delta r}}\right)\} \sim \underset{\underline{\Delta r}}{min}\{S_2\left(\widehat{\underline{\Delta r}}\right)\}$ and we only need to minimize $S_2\left(\widehat{\underline{\Delta r}}\right)$ for a fixed Δt. From equations (3.3)-(3.9), we find that: $\nabla S_2\left(\widehat{\underline{\Delta r}}\right) = 0$ so that $\dfrac{\widehat{\Delta x}_{\max}}{\widehat{\Delta t}} = \mu_x$; $\dfrac{\widehat{\Delta y}_{\max}}{\widehat{\Delta t}} = \mu_y$. We thus see that the cross correlation techniques used to estimate AMV's do indeed correspond to the mean advection in the region considered. In contrast, if the spectra are used to estimate the advection from (k_x, ω) and (k_y, ω) sections, using equation (3.20), we estimate the μ'' velocities which are related to the μ velocities measured by AMV's by an extra normalization factor (however these represent an average over the total sample, as we'll see in the next section).

3.5 Intermittency

3.5.1 Cascades

Up until now, we have used Fourier techniques since these are straightforward, well understood and allowed us to validate the basic space-time turbulence model. The main limitation is that spectra are second order statistics so that - unless the statistics are quasi-Gaussian - they only give a partial description of the process. In order to obtain a full description, we must consider statistics of all orders; this takes into account intermittency. A full validation necessitates a characterization of the flux φ which, in this model, is the result of a multiplicative cascade process. In such processes, a large ("mother") eddy breaks up into smaller ("daughter") eddies, transferring to each of them a fraction of its turbulent flux φ, according to a stochastic rule. The process is scale invariant and repeats down to smaller and smaller scales (until scales at which viscosity becomes dominant are reached). The resulting flux at resolution λ will have the following statistics where, generally, different moments and intensities have different scaling behaviours:

$$M_q = \frac{\left\langle \varphi_\lambda^q \right\rangle}{\left\langle \varphi_1 \right\rangle^q} = \lambda'^{K(q)}; \quad \lambda' = \frac{L_{eff}}{\Delta x} = \frac{\lambda}{\lambda_{eff}}; \qquad \lambda = L_w / \Delta x \; ; \quad \lambda_{eff} = L_w / L_{eff} \tag{3.24}$$

where $K(q)$ is the multi-scaling exponent, L_{eff} is the effective outer scale of the cascade, $L_w \approx L_e$=20000 km is the size of the earth and λ is the scale ratio with respect to the reference scale and λ' with respect to the effective outer (initial) cascade scale in which is determined empirically. $<\varphi_1>$ is the large scale mean of the flux and serves as a normalisation factor. <.> means ensemble average. For temporal analysis, instead of using L_w, we can use a reference time scale τ_{ref} = the duration of our sample. Equation (3.24) states that for a pure cascade, if, for different values of q, we plot the log of the normalized statistical moments versus the log of the scale ratio, we should observe straight lines with slopes $K(q)$ and these lines should intersect at L_{eff} (or if the analysis is in the time domain, τ_{eff}). These stochastic multiplicative cascades are the generic multifractal process and $K(q)$ is a convex function. For the "generator" of the cascade (i.e. of the multiplicative factors determining how φ is transferred from one scale to another at each step of the cascade), we can apply the additive central limit theorem [*Schertzer and*

Lovejoy, 1987, 1997], so that K(q) can be expressed as a stable and attractive (universal) form depending on two parameters:

$$K(q) = \frac{C_1}{\alpha - 1}(q^{\alpha} - q) \tag{3.25}$$

where C_1 is the "codimension" of the mean (i.e. a measure of the sparseness of the dominant contribution to the mean flux) and α ($0 < \alpha < 2$) is the (Lévy) index of multifractality. For $\alpha < 2$, this is only valid for $q > 0$; for $q < 0$, the moments diverge.

3.5.2 The space-time cascade structure of MTSAT and TRMM radiances

To quantify the intermittency of the cascade, we calculate the statistical moments of φ as a function of spatial (or temporal) scale Δx and see if they follow equation (3.24). Since MTSAT was over-sampled in the east-west direction [*Kigawa and Sullivan*, 1998], there was spurious lower variability at the smallest scale (5 km) and we therefore spatially averaged the data to 10 km resolution. We then estimated the normalized flux:

$$\varphi' = \frac{\varphi}{\langle \varphi \rangle} = \frac{\Delta I}{\langle \Delta I \rangle} \tag{3.26}$$

The fluctuation in the field was estimated as $\Delta I = Max\left\{\left|I(x+\Delta x, y) - I(x,y)\right|, \left|I(x, y+\Delta y) - I(x,y)\right|\right\}$ for each pixel where x and y are coordinates in east-west and north-south directions respectively and $\Delta x = \Delta y = 10$ km, the resolution at which the flux was estimated, (I is the thermal IR radiance intensity measured by MTSAT). The "max" was used to partially compensate for residual measurement artefacts (excessive small scale smoothness). This improved the scaling somewhat at the smallest scales, but is not essential.

We can verify the predictions of the cascade model (equation (3.24)) by degrading (averaging) the resolution of the flux, taking ensemble averages of different powers of the flux for each scale of the degradation process, (we took 10 points per order of magnitude of scales, equally spaced on a log scale). Figure 3.6 shows the results for the zonal and meridional directions. The "effective" outer spatial scales of the cascade are found to be L_{eff}=50000 km and 32000 km in the east-west and north-south directions respectively, i.e. somewhat larger than planetary scales. This is possible because even at planetary scales there are nonlinear interactions with other atmospheric fields, which are responsible for

the additional planetary scale variability. We see that for spatial analyses, the predictions of the cascade model are well verified for smaller scales, up to ~ 6000 and 2000 km for east-west and north-south directions respectively; for scales beyond this we observe deviations from pure scaling. The upper scaling regime limit is smaller than L_{eff} (the outer cascade limit) and is comparable to the spectral scales L_d (5000 km and 2500 km for E-W and N-S directions respectively) from the spectral method in section 3 (table 1). These large scale deviations may be at least partly due to the anisotropy discussed earlier. Therefore, it is interesting to average the moments in both directions: $M_q^{(EWNS)} = \frac{M_q^{(EW)} + M_q^{(NS)}}{2}$. When this is done (Figure 3.4), we observe almost perfect scaling over the available range of scales.

For the temporal analysis, we had to deal with an extra complication due to the resolution of the data. MTSAT images are taken every hour, but the radiances are not *averaged* over one hour (i.e. they are basically snapshots). However, it is the resolution in *space-time* that is important: averaging snapshots in space at resolution L has the same space-time resolution as averaging data with very small spatial resolution in time over durations $\tau = L/V_w$ where V_w is the velocity estimated from the spectrum i.e. ≈40 km/h. In order to sample at the appropriate time scale and to keep the highest resolution possible, we averaged our estimated flux over a 30 km scale.

In Figure 3.4, we observe that up to about ~2 days, the data are well described by the model, beyond which we observe significant deviations from scaling (the effective outer cascade scale τ_{eff} ~48 days estimated by regression is the outer scale required so that the smaller scale statistics are accurate). As mentioned earlier, atmospheric dynamics undergoes a drastic change in its variability from a *weather* regime at time scales less than ~10 days to a macroweather regime at larger scales. As expected, the MTSAT data exhibit a breakdown in the scaling, but at scales a little bit smaller than this (2 days), even though it is not completely obvious to determine the transition scale from these curves. Here we see a large spread between the outer cascade scale (48 days) and the scale where the cascade scaling becomes poor (~2 days) and the scale at which the spectral scaling breaks down (~4 days, see table 1). At small time scales - the weather regime - the statistics of the turbulent flux are described by a cascade. At larger scales - the macro

weather - the spatial degrees of freedom are effectively quenched and there is a "dimensional transition" leading to different, low intermittency statistics.

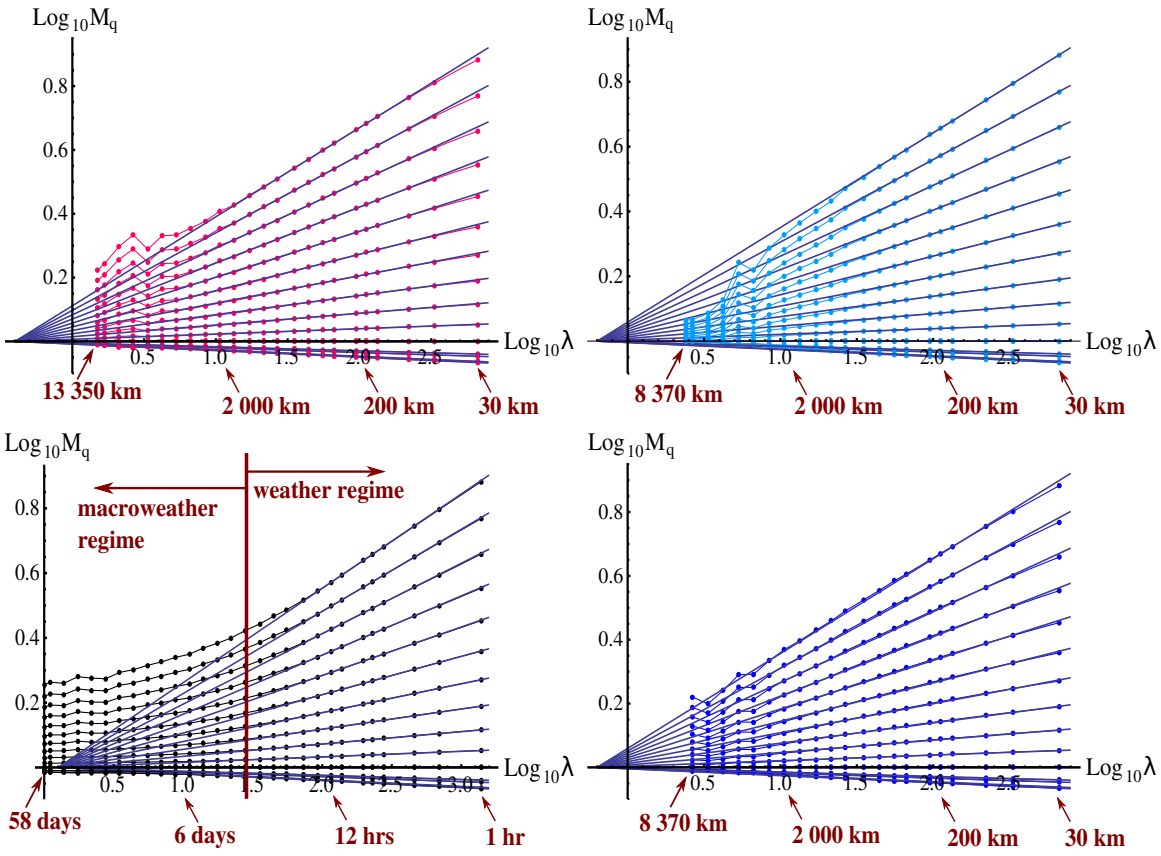

Figure 3.4: Log-log plot of the moments M_q of the normalized flux φ' for MTSAT thermal IR as a function of the scale ratio λ (dots correspond to data). Each curve corresponds to a single value of q, from q=0 at the bottom to q=3 at the top, by step of 0.2. Straight blue lines are a fit with the constraint that they all intersect at a unique scale, L_{eff}. Each graph corresponds to a different direction in which the degradation of the resolution was done. Top-left: east-west, L_{eff}=50 000 km. Top-right: north-south, L_{eff}=32 000 km. Bottom-left: time, τ_{eff} =48 days. Bottom-right: average of east-west and north-south directions, L_{eff}=32 000 km.

In order to further substantiate this space-time scaling model, we also used Tropical Rain Measuring Mission (TRMM) data. The TRMM satellite was launched in 1997 by the National Aeronautics and Space Administration (NASA) to monitor the atmosphere in tropical regions. Its orbit is between ±38° of latitude at an altitude of 350 km, (period ~90 minutes; average return period ~2 days. See Figure 3.5). The satellite

measures radiances in 5 bands in infrared and visible (VIRS) - at wavelengths: 12.2 μm ; 10.8 μm ; 3.75 μm ; 1.60 μm and 0.63 μm - as well as in the microwave region (TMI) at frequencies 10.65 GHz, 19.35 GHz, 21.3 GHz, 37 GHz and 85.5 GHz. TRMM thus has the advantage (over MTSAT) of providing access to larger scales (in the zonal direction) as well as extra wavelengths not provided by MTSAT. The VIRS instrument is primarily sensitive to clouds whereas TMI is a radiometer that is also sensitive to rain (NASDA, 2001). Below, we analyzed 359 days in 1998 of VIRS channel 5 (~12.2 μm, sensitive to the temperature near the top of clouds, resolution 2.2 km, swath width 720 km) and TMI channel 8 (85.5 GHz, that has a strong signal from rain, resolution 4.4 km, swath width 760 km).

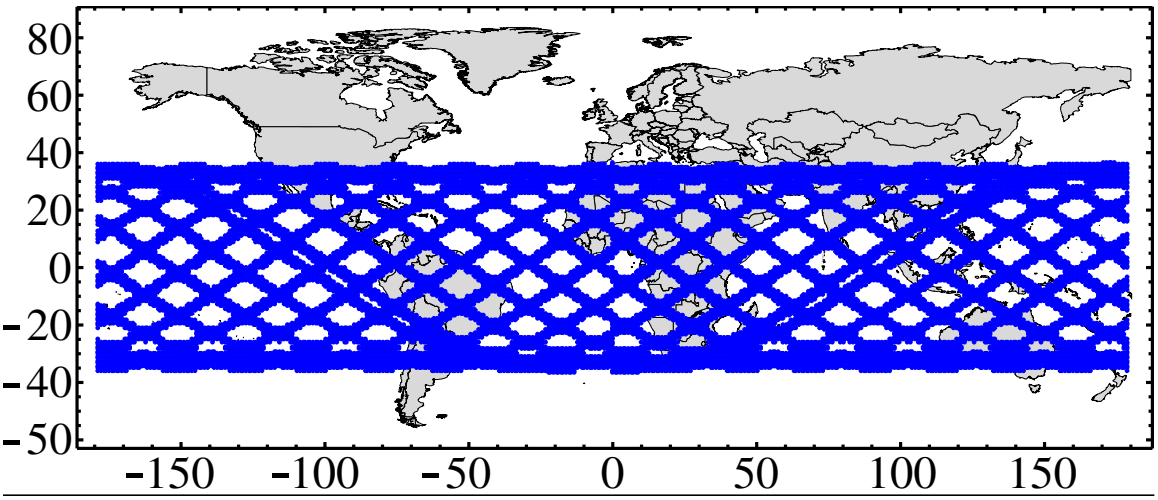

Figure 3.5: One day (i.e. ~16 orbits, in blue) of TRMM VIRS-5, (2.2 km resolution) degraded at 100 km resolution. The temporal resolution is higher near ±38°.

When analysing TRMM radiances, we degraded the data resolution by a factor 2 before estimating the fluxes (in order to avoid possible spuriously smooth data at highest resolution). In order to investigate the temporal scaling in the weather and low-frequency weather regimes, we averaged the data at resolutions 1 day and 100 km in time and space (see Figure 3.5). The return period of the satellite is shorter at higher latitudes from the equator and can be as much as 4 days for certain areas near the equator. The space-time resolutions were thus chosen as a compromise, so the analysis could benefit from the

highest temporal resolution possible while having enough values to provide a good spatial average on and reasonable statistics. We rejected every resulting 100 km pixel having less than a critical fraction (75%) of data coverage. Similarly, when testing equation (3.24) for different spatial or temporal resolutions, we rejected degraded pixels with more than 25% missing values.

Figures 3.6 and 3.7 show the results for VIRS-5 and TMI-8. For VIRS-5, we see that for the east-west spatial analysis, predictions of our cascade model are generally well verified except for small deviations at small scales for high order statistical moments. The outer scale is L_{eff}=25000 km, a little smaller than for MTSAT (~50 000 km) in the same direction. The scaling in the north-south direction is not as good with additional, although small, deviations at larger scales. The outer scale of the north-south cascade is L_{eff}=12600 km, again smaller than what we found for MTSAT. For the temporal analysis, we observe that equation (3.24) gives an accurate description (with an outer scale τ_{eff}=57 days) for small scales, up to ~14 days, scale beyond which, once again, we observe significant deviations from scaling, (corresponding to a transition towards a different scaling regime). (See table 1)

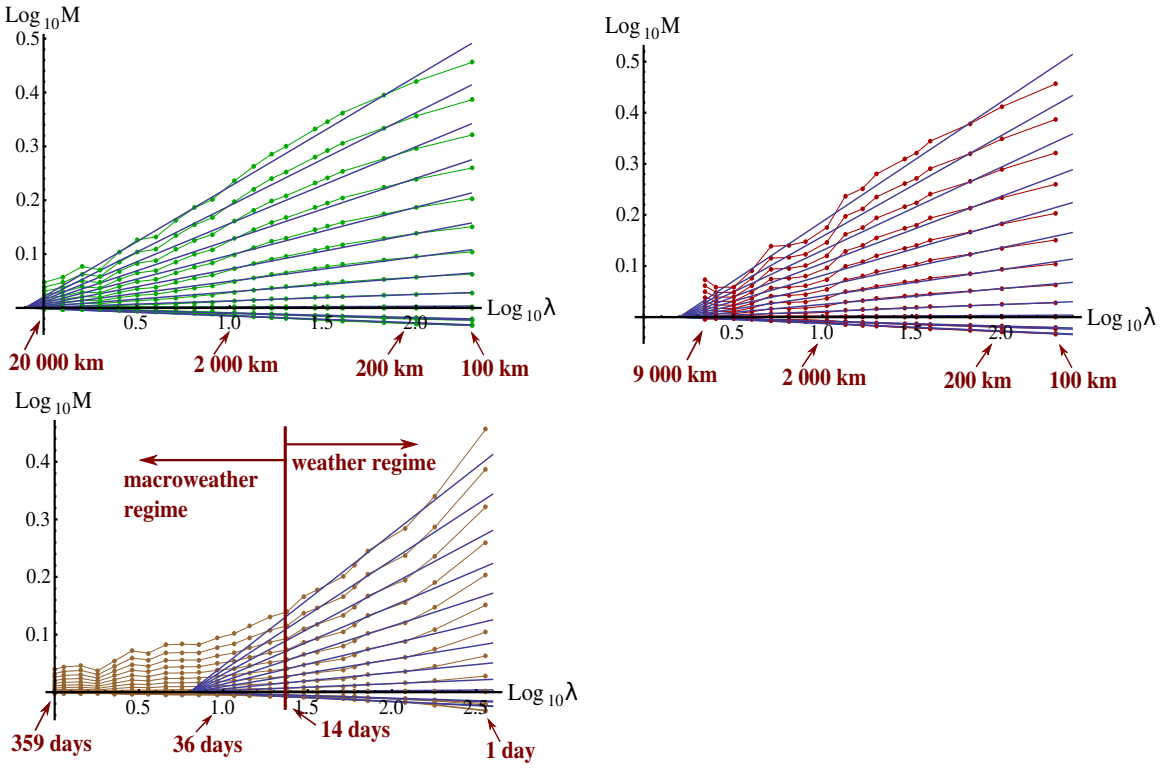

Figure 3.6: Log-log plot of the moments M_q of the normalized flux φ' for VIRS-5 as a function of the scale ratio λ (dots correspond to data). Each curve corresponds to a single value of q, from q=0 at the bottom to q=2.8 at the top, by step of 0.2. Straight blue lines are a fit with the constraint that they all intersect at a unique scale, L_{eff}. Each graph corresponds to a different direction in which the degradation of the resolution was done. Top-left : east-west, L_{eff}=25000 km. Top-right : north-south, L_{eff}=12600 km. Bottom-left : time, τ_{eff}=57 days.

For TMI-8, the cascade model predictions are well followed for spatial scales up to 4000 and 2000 km for east-west and north-south directions respectively. At larger scales, we observe slight deviations from pure scaling. Similarly to MTSAT and VIRS-5, the north-south moments have lower variability than predicted by the cascade model at large scales, while variability of east-west moments is slightly higher than the model predictions. The outer scales are L_{eff}=12600 km and 8000 km for east-west and north-south directions respectively; scales smaller than for MTSAT and VIRS-5. For the temporal direction, we can identify a weather regime at small scales (< 4 days), even though there are only a few data points. The outer scale is τ_{eff}=57 days, just like VIRS-5. For time scales larger than 4 days, we observe the usual transition.

We can compare these values with analyses of VIRS-5 and TMI-8 data in the satellite orbit direction made by *Lovejoy et al.* [2009d] at higher resolutions (8.8 km and 13.9 km for VIRS-5 and TMI-8 respectively) from the months of January and February 1998 (Table 1). Interestingly, the values of L_{eff} and L_d found in their analyses are comparable with our values in the north-south direction.

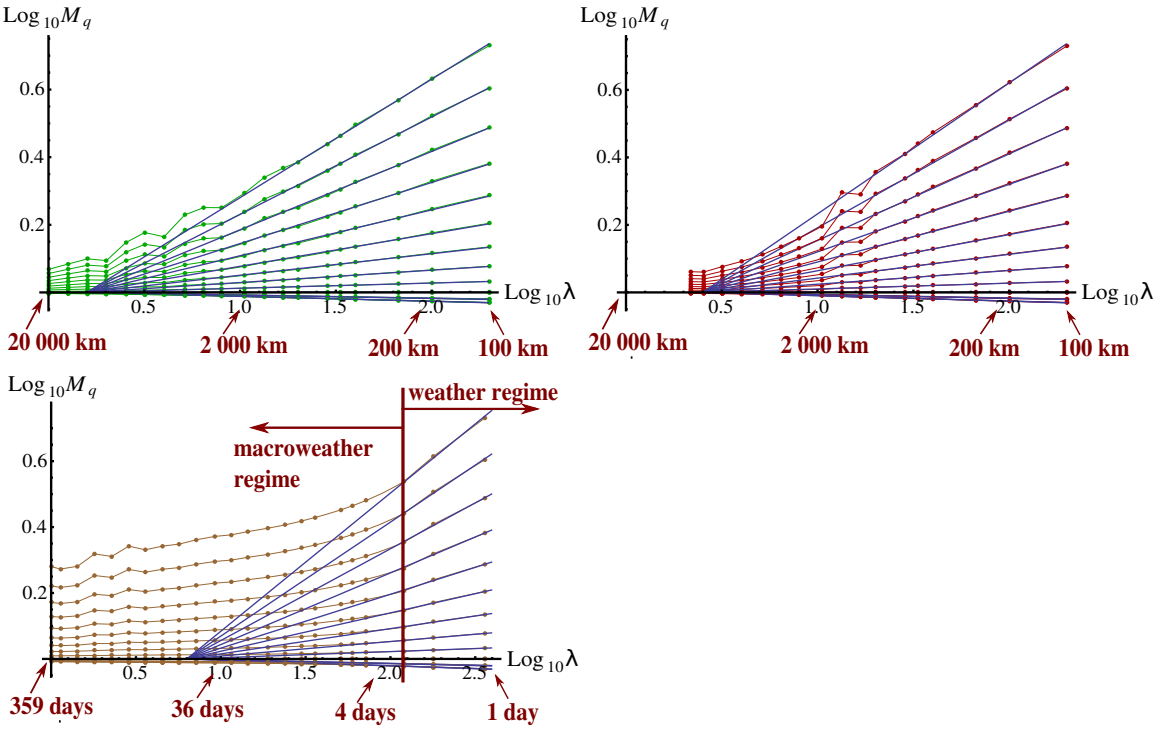

Figure 3.7: Log-log plot of the moments M_q of the normalized flux φ' for TMI-8 as a function of the scale ratio λ (dots correspond to data). Each curve corresponds to a single value of q, from q=0 at the bottom to q=2.8 at the top, by step of 0.2. Straight blue lines are a fit with the constraint that they all intersect at a unique scale, L_{eff}. Each graph corresponds to a different direction in which the degradation of the resolution was done. Top-left : east-west, L_{eff}=12600 km. Top-right : north-south, L_{eff}=8000 km. Bottom-left : time, τ_{eff}=57 days.

From Figures 3.4, 3.6 and 3.7 we can estimate the multi-scaling exponent $K(q)$ with the parameter C_1 and α for the three directions (east-west, north-south, time). We see from Figure 3.8 that the intermittency of MTSAT data is nearly the same in all directions. Similarly to MTSAT, the intermittency of the VIRS-5 and TMI-8 fluxes is almost isotropic (Figure 3.8), with small differences in the different directions for higher

statistical order. We estimate C_1 using $C_1 = K'(1)$ (see equation (3.25)). All the values are close to each others and are comparable to those found by *Lovejoy et al.* [2009d], (although our value for TMI-8 is a little bit smaller, see table 1.)

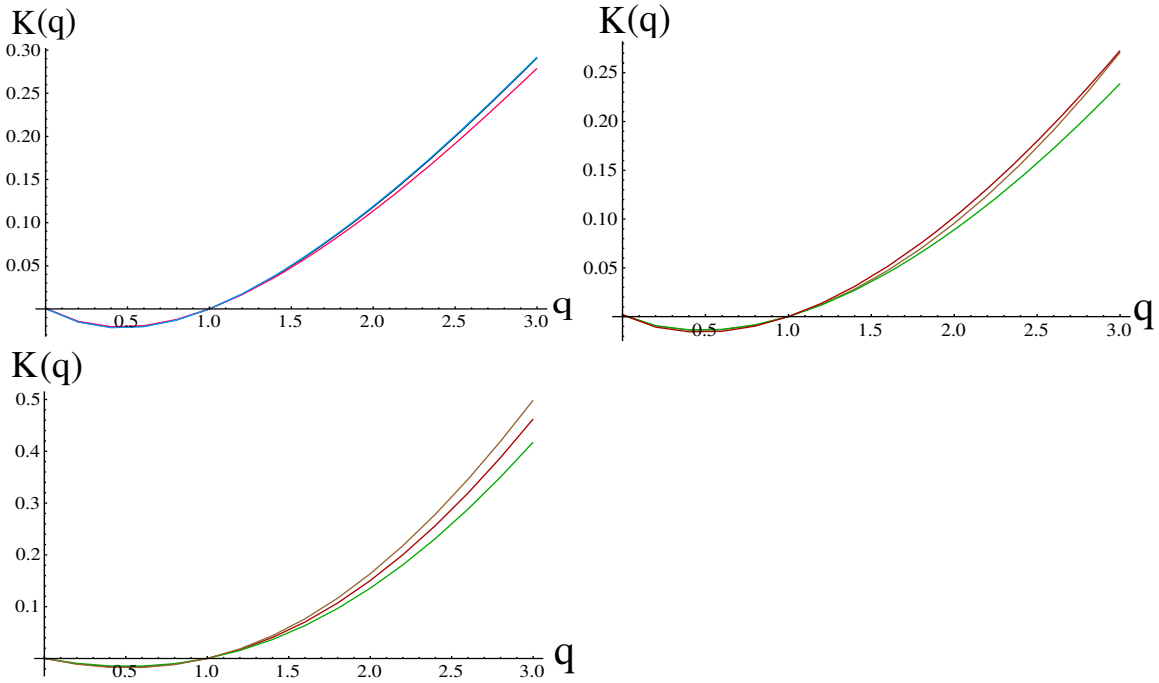

Figure 3.8: Top-left: Characterization of the intermittency of MTSAT thermal IR turbulent flux by its moment scaling exponent $K(q)$ estimated from Figure 3.4. In blue: north-south direction, C_1=0.07. In magenta: east-west direction, C_1=0.07. In black (superposed to the north-south curve exactly): in time, C_1=0.07. Top-right: Characterization of the intermittency of VIRS-5's turbulent fluxes by its moments scaling exponent function $K(q)$ estimated from Figure 3.6. In red: north-south direction, C_1=0.06. In green: east-west direction, C_1=0.05. In brown: temporal direction, C_1=0.05. Bottom: Characterization of the intermittency of TMI-8's turbulent fluxes by its moments scaling exponent function $K(q)$ estimated from Figure 3.7. In red: north-south direction, C_1=0.06. In green: east-west direction, C_1=0.05. In brown: temporal direction, C_1=0.08.

With the help of eq. (3.25), we can also estimate the parameter α. We calculate the "reduced moments": $M'_q = M_q^{(\alpha-1)/(q^\alpha - q)} = \lambda^{C_1}$. If the log of the moments follow equations (3.24) and (3.25), all the curves should collapse - the "Lévy collapse" - onto a single curve λ^{C_1} (up to a critical value q_c beyond which $K(q)$ becomes linear, expressing the fact that the moments of order $q > q_c$ are dominated by the maximum value in a finite

sample. We can estimate α for the cascade by identifying the value for which we find the best collapse. The values of α for our three datasets vary, though they are all ≥1.5. (See Figure 3.9 and Table I).

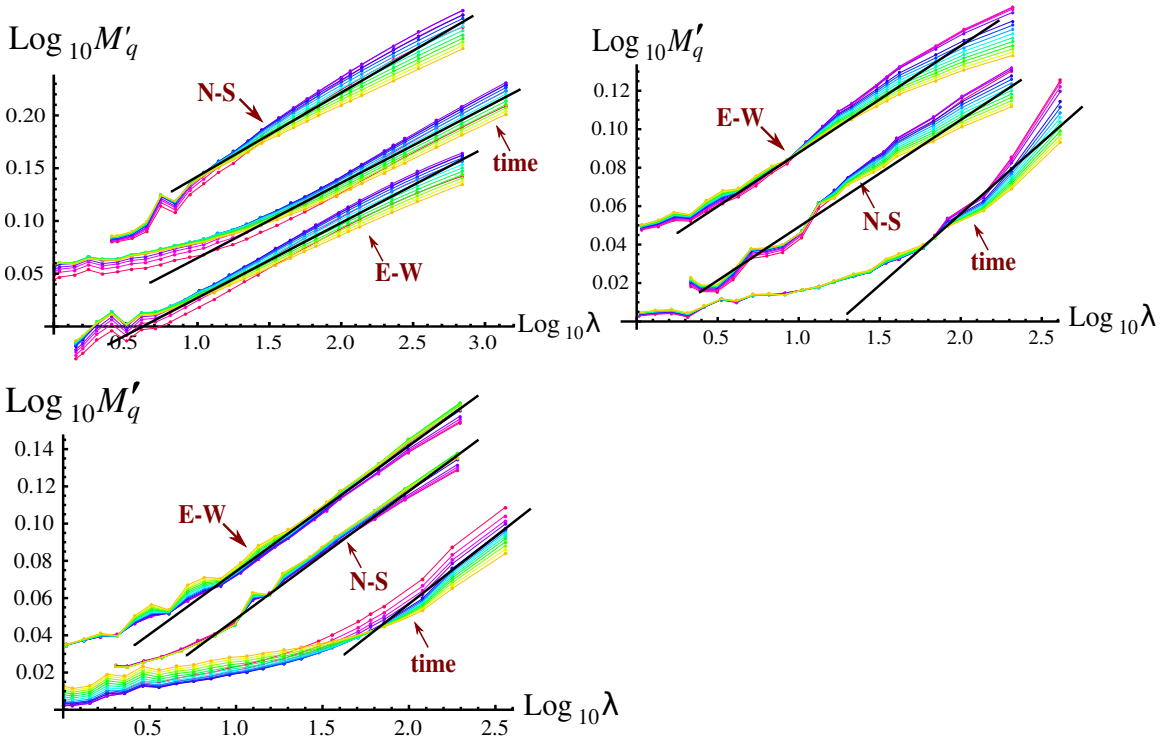

Figure 3.9: Levy collapse for the value of α that minimizes the deviations. Top-left: MTSAT IR fluxes: α~1.5-1.6. Top-right: VIRS-5 fluxes: α~1.8. Bottom: TMI-8 fluxes: α~2.2 (since theoretically α≤2, presumably, α~2). Note that the outer scale (corresponding to λ=1) in the spatial analyses was 20000 km whereas in time it was 2 months (MTSAT) and 359 days (VIRS-5, TMI-8).

3.5.2 Probability distributions of MTSAT and TRMM radiance fluxes

In the last section, in order to study the intermittency, we presented a detailed analysis of the statistical moments of radiance fluxes. We can also, in an equivalent way, describe the fluxes by looking at their probability distributions. A general prediction of cascade models is that their extreme probability tails are "hyperbolic" or "fat-tailed":

$$\Pr(\varphi > s) \sim s^{-q_D} \quad ; \qquad s \gg 1 \quad ; \qquad q > q_D \tag{3.27}$$

The value q_D depends on the bare cascade, but also on the space-time dimension D over which the bare cascade is averaged. Distributions with an exponent q_D have statistical moments that diverge for all orders $q > q_D$. If the sample size is sufficiently large, we can

observe this hyperbolic tail as a straight line on a log-log plot. Figure 3.10 shows the results for MTSAT and TRMM fluxes. While VIRS-5 and TMI-8 fluxes fairly convincingly exhibit this hyperbolic behaviour with $q_D \approx 7$, MTSAT fluxes have distributions which fall off much more rapidly. In comparison, *Lovejoy and Schertzer* [2013] present a summary of similar analyses including horizontal wind for which q_D=5-7.5 and temperature for which q_D=4.5-5.5 was found. The existence of hyperbolic tails has theoretical implications since it means that certain models of the atmosphere such as Log-Poisson or microcanonical cascades can be ruled out.

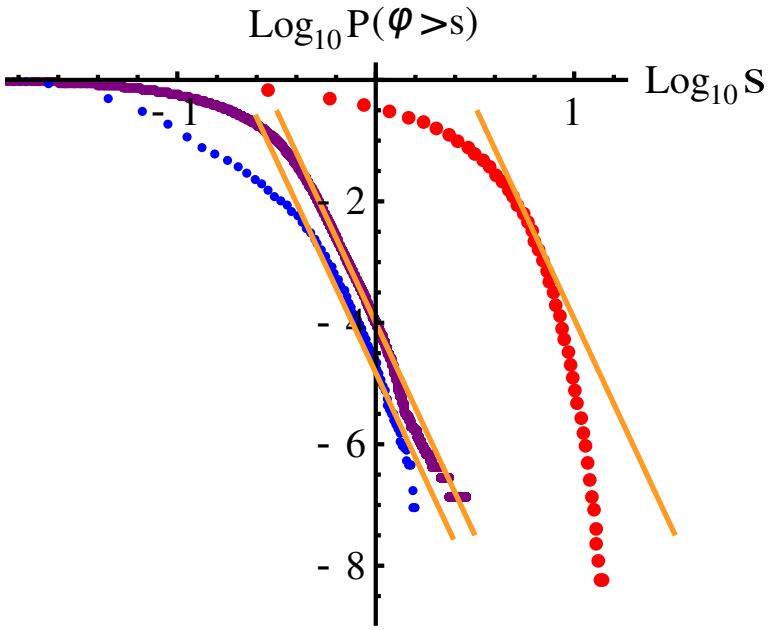

Figure 3.10: Probability distributions for the radiances fluxes exceeding a fixed threshold *s*. In red: MTSAT fluxes at 30 km, 1 hr resolutions. In purple: VIRS-5 fluxes at 100 km, 1 day resolutions. In blue: TMI-8 fluxes at 100 km, 1 day resolutions. The orange reference lines all have absolute slopes $q_D = 7$.

3.5.4 Space-time statistical relation from atmospheric radiance fluxes

In order to further characterize the space-time statistics, we may estimate the Eulerian size/lifetime statistical relation. A method is to find a correspondence between spatial and temporal resolution for which the variability is the same:

$$\left\langle \varphi^q_{\tau_{ref}/\tau} \right\rangle = \left\langle \varphi^q_{L_{ref}/L} \right\rangle \tag{3.28}$$

i.e. an implicit relation between τ and L. The fact that the $K(q)$ functions are close for space and time shows that this relation is the same for all q's and that there is a constant

value - with the dimensions of a velocity - describing this space-time relation. If the scaling were perfect with identical $K(q)$ in space and time, we would obtain:

$$V_{eff} = \frac{L_{eff}}{\tau_{eff}} \tag{3.29}$$

To test this, we may estimate V_{eff} by superposing the curves from Figures 3.4, 3.6 and 3.7 and horizontally shift one set of curves (spatial or temporal), such as to make them overlap as much as possible (Figures 3.11, 3.12 and 3.13). From this shift, we can identify the relation between L and τ (giving the same variability) and can extract V_{eff}. We found for MTSAT (Figure 3.10) V_{eff}=33 km/h =792 km/day (average of east-west and north-south directions), comparable with V found from spectral methods (~41 km/h ≈ 1000 km/day, see Table 1). This effective velocity implies that a structure in the flux of size 33 km will "live" for 1 hr. These velocities are typical values of turbulent wind in the atmosphere (~36 km/h=10 m/s). Although a linear relation between spatial and temporal statistics is predicted by the "frozen turbulence" hypothesis; our interpretation is quite different. In "frozen turbulence", relative motion within structures is negligible and V_{eff} is a constant deterministic advection velocity whereas in our case, V_{eff} is a turbulent velocity (e.g. a RMS velocity). Similarly, we can compare statistics in east-west and north-south directions, a relation expressed with the parameter a that describes the horizontal space trivial (scale independent) anisotropy. We found a≈1.2 so that structures are typically 1.2 times wider (E-W) than their N-S extents. (c.f. the value a~1.2 from MTSAT IR spectra ; see Table 1).

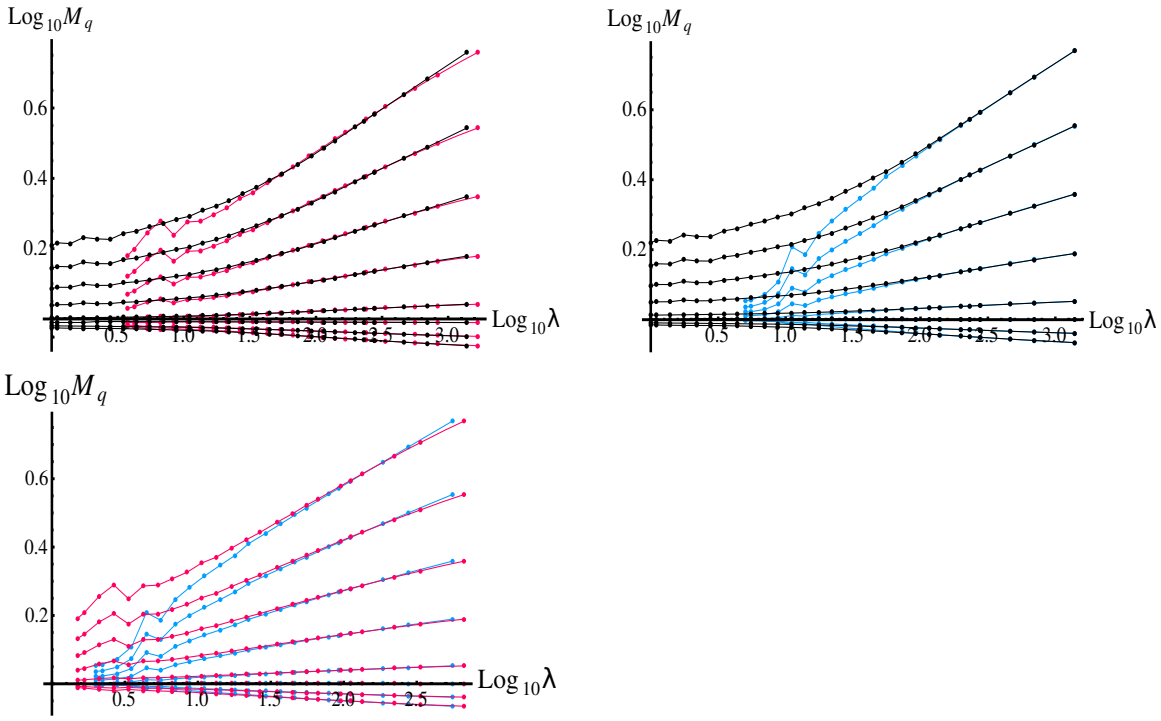

Figure 3.11: Comparison of statistical moments of radiances fluxes. One set of curves is shifted to match the other set. An effective velocity V_{eff} is extracted from that shift, characterizing the statistical size/lifetime relation for atmospheric structures measured by MTSAT. Upper-left: space (east-west: magenta) vs time (black), V_{eff}=36 km/h. Upper-right : space (north-south : blue) vs time (black), V_{eff}=30 km/h . Bottom: space (north-south: blue) vs space (magenta), a=1.2 (characterizing horizontal trivial anisotropy). Values of q shown: 0.0 ; 0.4 ; 0.8 ; 1.2 ; 1.6 ; 2.0 ; 2.4 ; 2.8.

Figures 3.12 and 3.13 show the corresponding matches of statistical moments for VIRS-5 and TMI-8. From the shift applied, we can extract an effective velocity: V_{eff}=14 km/h=336 km/day and for V_{eff}=5 km/h=120 km/day for VIRS-5 and TMI-8 respectively, smaller than for MTSAT (Table 1). The spatial anisotropy parameters a are on the contrary all comparable.

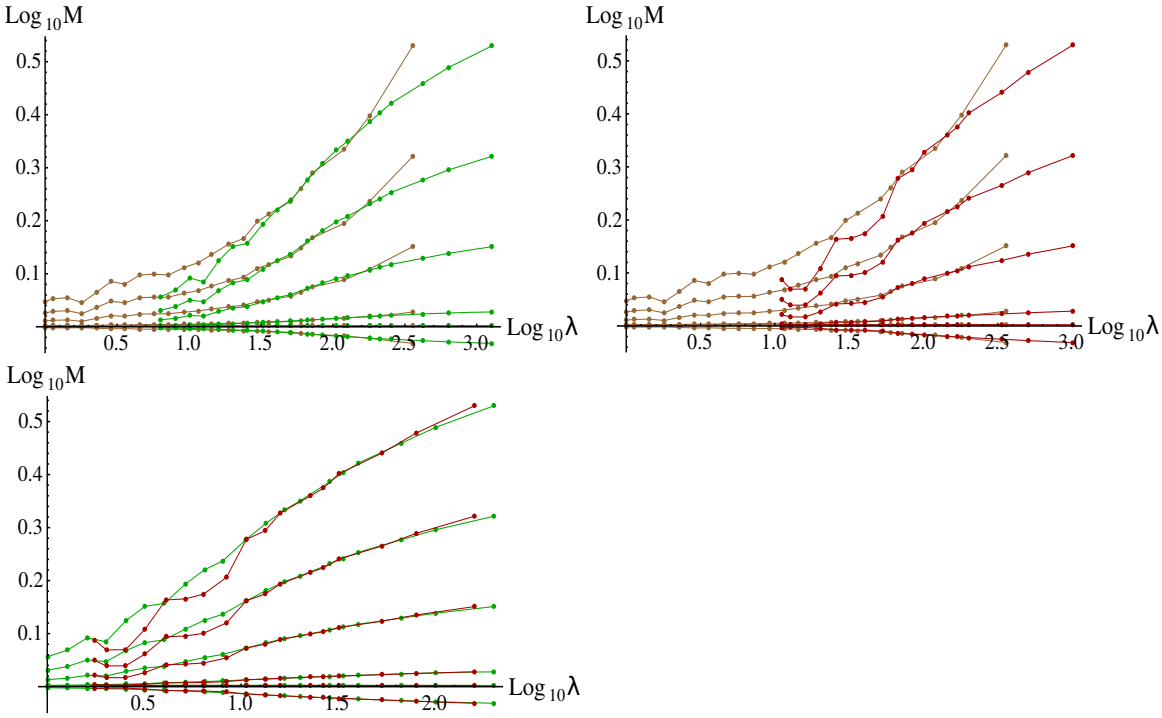

Figure 3.12: Comparison of statistical moments of VIRS-5's fluxes. One set of curves is shifted to match the other set. An effective velocity V_{eff} is extracted from that shift, characterizing the statistical size/lifetime relation for atmospheric structures measured by VIRS-5. Upper left : space (east-west : green) vs time (brown), V_{eff}=15 km/h. Upper right : space (north-south : red) vs time (brown), V_{eff}=12 km/h. Bottom : space (north-south : red) vs space (green), a=1.3 (characterizing horizontal trivial anisotropy). Values of q shown : 0.0 ; 0.6 ; 1.0 ; 1.6 ; 2.2 ; 2.8.

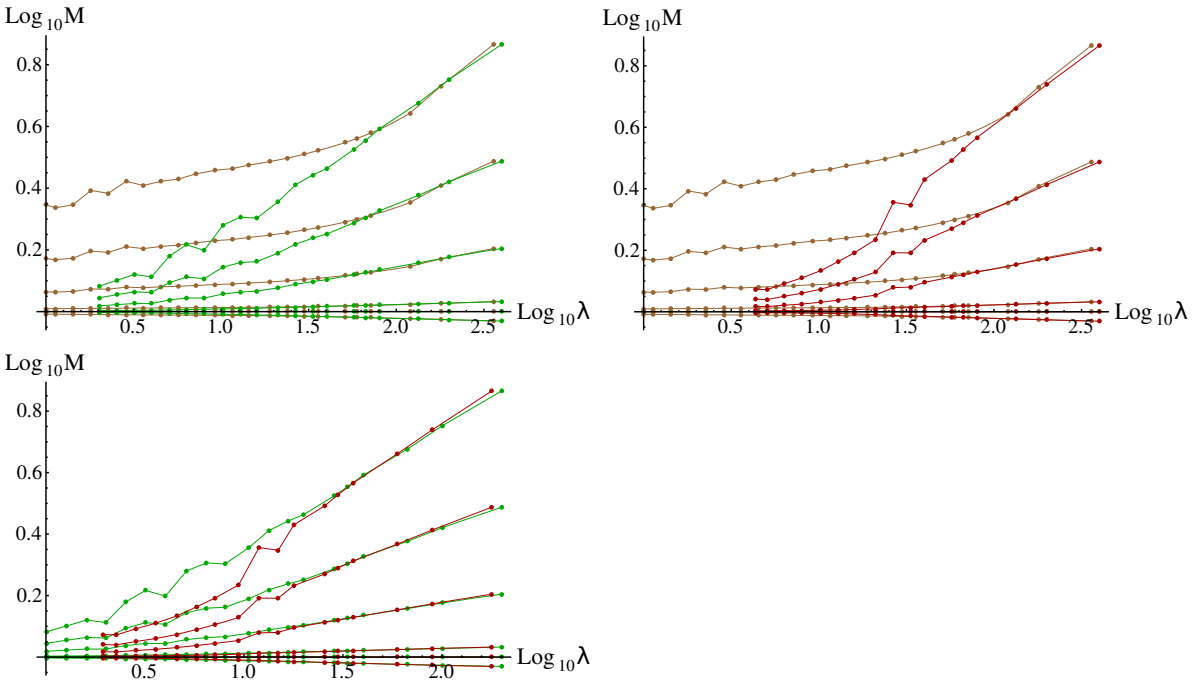

Figure 3.13: Comparison of statistical moments of TMI-8's fluxes. One set of curves is shifted to match the other set. An effective velocity V_{eff} is extracted from that shift, characterizing the statistical size/lifetime relation for atmospheric structures measured by TMI-8. Upper left : space (east-west : green) vs time (brown), V_{eff}=5 km/h. Upper right : space (north-south : red) vs time (brown), V_{eff}=5 km/h. Bottom : space (north-south : red) vs space (green), a=1.1 (characterizing horizontal trivial anisotropy). Values of q shown: 0.0 ; 0.6 ; 1.0 ; 1.6 ; 2.2 ; 2.8.

We can also compute the Eulerian space-time diagrams and its spatial counterpart space-space diagrams (see Figure 3.14) for MTSAT and VIRS-5 fluxes. Unfortunately, as can be seen in Figure 3.13, in the case of TMI-8 we only have three data points in the weather regime which is insufficient for a reliable estimate. From Figures 3.4 and 3.6, we chose an order of statistical moment (q=1.8) that is well estimated and, from the values of the chosen moment, we found a correspondence between spatial and temporal lags (for which the moment values are the same). We see on Figure 3.14 straight lines with slopes 1, reflecting the good scaling we obtained on Figures 3.4 and 3.6. A structure ≈100 km zonal extent will on average last 3 hrs, a ≈1000 km structure (a little bit less in the meridional direction) will last 30 hrs, etc. From Figure 3.14, we can also estimate the parameters V_{eff} and a. We found values all consistent with those found from the previous

method, when shifting all the moments, (for MTSAT: V_{eff}~33 km/h=792 km/day and a=1.5 - for VIRS-5: V_{eff}=14 km/h=336 km/day and a=1.5).

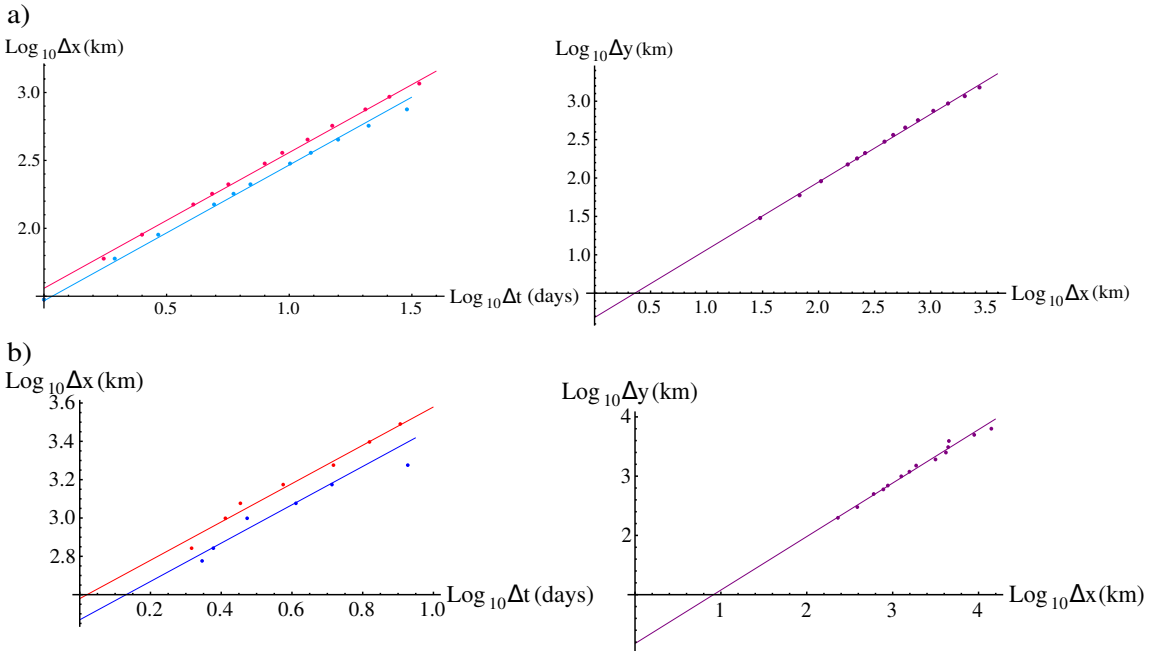

Figure 3.14: a) Left : Space-time diagram for q=1.8 and Δt<63 hrs (belonging to the weather regime) for MTSAT fluxes. Magenta: east-west direction ; V_{eff}=36 km/h. Blue: north-south direction ; V_{eff} =30 km/h. Right: MTSAT fluxes space-space diagram for q=1.8 ; a=1.5. b) Left : Space-time diagram for q=1.8 and Δt<8 days (~weather regime) for VIRS-5 fluxes. Magenta: east-west direction ; V_{eff}=16 km/h. Blue: north-south direction ; V_{eff}=12 km/h. Right: VIRS-5 fluxes space-space diagram for q=1.8 ; a=1.5. Reference lines have slope =1 corresponding to linear space-time (space-space) relations.

3.6 Conclusions

Understanding the space-time statistical behaviour of atmospheric fields as functions of scale is a fundamental yet little studied problem. Indeed, it is troubling that in spite of the plethora of data now available, that there is no agreement about the theoretical or empirical space-time statistical properties of the atmosphere including the power spectrum. However, we argue that over wide ranges, the atmospheric spatial variability is well described by an anisotropic scaling model where two different scaling laws apply in the horizontal and vertical. In this model, no scale separation exists and Taylor's frozen turbulence hypothesis is not justified. Since in the Eulerian frame

advection is the key ingredient in relating spatial to temporal statistics, this anisotropic spatial scaling will have direct consequences for the temporal scaling.

We discussed this theoretically, making the assumption that the largest (planetary scale) eddies advect the smaller ones, averaging over these random advections. The result is that the structure functions and spectra are both power laws of scale functions, themselves approximately quadratic forms in (x, y, t) and (k_x, k_y, ω) spaces respectively. The parameters depended on the mean advection velocity as well as the turbulent velocity and a mean north-south/east-west aspect ratio.

The theory was tested on 1-D and 2-D spectral cross-sections using infrared radiances measured by geostationary satellites which allow us to estimate space-time statistics over wide ranges of scale. Estimating spectra from infrared MTSAT data, we found that our theoretical spectra accurately reproduce the observed 3D (k_x, k_y, ω) spectral density over the range 1 hour to ≈4 days and 30 km to ≈5000 km. Multivariate regressions provided the best fit parameters $\tau_w \sim 20\pm1$ days (using $L_w \sim L_e$=20000 km), the mean lifetime of planetary structures, $V_w \sim 41\pm3$ km/h, their typical relative velocity as well as the average overall advections in zonal ($\overline{v_x} \sim -12\pm4$ km/h) and meridional ($\overline{v_y} \sim 4\pm3$ km/h) directions over a ~2 month period for a region centred slightly south of the equator in the western Pacific. The 1D spectral exponents were the same in the 3 space-time directions (i.e horizontal space-time isotropy for the exponents), with $\beta \sim 1.55\pm0.01$, comparable to the passive scalar, Corrsin-Obukhov value with intermittent corrections (β=5/3 - $K(2)\approx1.55$)). While the data comes primarily from the tropics, we consider high level emergent statistical laws; there is no reason to assume that they contradict the usual (deterministic) laws of tropical meteorology.

Spectra are only second order statistics; to obtain a more complete description of the statistics, we found that we can describe atmospheric radiances (including TRMM's infrared and passive microwave) turbulent flux statistics by a multiplicative cascade model over large ranges of spatial scales with typically slight deviations at small and large scales. Analogous temporal analyses showed similar agreement at small scales, but with significant deviations at scales larger than a few days (2 days for TMI-8, 14 days for VIRS-5 and 4 days for MTSAT), marking two regimes. It was proposed that these two

regimes separated by this temporal scale break (associated with planetary scales in space) could be identified as a "weather regime" at short time scales and a "macroweather" regime at longer time scales, providing a concrete way to characterize the dynamical processes associated with weather and determine their corresponding space-time scales. (This break in the scaling symmetry is also present in the temporal spectrum, although only for the few low frequency data points.) With the help of a multiplicative cascade model, we were able to describe how the space-time statistics change with scales with the help of only a few parameters C_1 (the intermittency near the mean), α (the degree of multifractality), L_{eff} (the effective outer spatial scale), V_{eff} (the effective space-time transformation speed) and a (the zonal/meridional aspect ratio). Although the values of C_1 and a are all close to each other for our three data sets (MTSAT, VIRS-5 and TMI-8), we observe some differences in the remaining parameters. The values of L_{eff} is somewhat different for the three datasets, but its values (in the north-south direction) are comparable to those obtained by (Lovejoy and al., 2009d) (along with C_1) in the direction of the orbit of the satellite. The three datasets being associated with different wavelengths, they were sensitive to different types of structures (rain, clouds, etc.). The parameter α which gives a measure of how "extreme" (or multifractal) is the field was found to vary between 1.5 and 2. We have to mention that the method we used to estimate α is very sensitive on the scale of range considered and errors could be responsible for the discrepancies observed. We also showed that TRMM's VIRS-5 and TMI-8 fluxes exhibit nonclassical behaviour regarding the extreme values in the fact they follow hyperbolic probability distribution with exponent characterizing the extreme tails q_D=7. MTSAT fluxes seemed to involve much higher values of q_D. This can be used to rule out some models such as microcanonical and Log-Poisson cascades.

These results contribute to our understanding of atmospheric dynamics at a fundamental level, but could also be useful in applications such as improving the efficiency of meteorological measurements, as they prescribe the relation between the space-time resolutions at which these measurements should be made. This framework also provides a theoretical basis for interpreting IR satellite derived "Atmospheric Motion Vectors" in terms of turbulent winds. Although the model presented in this paper was used to describe turbulent field statistics, it can be extended to take into account

atmospheric waves as well. For this, our theoretical form can be used to determine the "turbulent background" and the residual can be interpreted in terms of waves. *Wheeler and Kiladis* [1999] similarly argued that atmospheric waves would be detectable from IR thermal spectral density, after the (ad hoc) removal of a turbulent background. We pursue this question in [*Pinel and Lovejoy*, 2013, (i.e. Chapter 4)].

Other questions for the future include comparing the statistics over land and over oceans. This could be done using geostationary data for a different geographical region (for instance, those covered by GOES satellites, which also has a high temporal resolution (30 minutes)). Also, it would be interesting, to extend the spectral analysis to lower frequencies in order to study the space-time statistics and scaling in the macroweather regime (which only seemed to appear for the last few large scale data points in our analysis). Corresponding spatial analyses can be made and another space-time statistical relation should be found (although this question is already discussed by *Lovejoy and Schertzer*, [2013]). Finally, the non-obvious effect of the vertical wind on the space-time scaling of the atmosphere still needs to be clarified.

Chapter 4: Atmospheric Waves as Scaling, Turbulent Phenomena

The following reproduces the article "Pinel, J., S. Lovejoy, (2013): Atmospheric waves as scaling, turbulent phenomena" submitted to **Atmospheric Chemistry and Physics** in February 2013. It presents an extension of the 23/9D anisotropic scaling model in the Fourier horizontal space-time domain (presented in the previous chapter) to take into account the statistical description of atmospheric waves; as well as an empirical test of this new developments using atmospheric radiances data (which were also used in the previous chapter).

Abstract

A paradox of atmospheric science is that the dynamics are highly nonlinear, turbulent and scaling, yet atmospheric waves are invariably modelled by linear or weakly nonlinear theories. We postulate that wave laws are analogous to the turbulent laws and are also constrained by scaling. We propose an effective turbulence - wave propagator which corresponds to a fractional and anisotropic extension of the classical wave equation propagator with dispersion relation similar to those of inertial gravity waves (and Kelvin waves) yet with anomalous (fractional) order $H_{wav}/2$.

Using geostationary IR radiances, we estimate the parameters finding that $H_{wav} \approx 0.17 \pm 0.04$ (the classical value =2). Our results have important consequences for energy transport and for understanding atmospheric dynamics.

4.1 Introduction

The atmosphere is a highly turbulent system with the ratio of nonlinear to linear terms - the Reynolds number - typically of the order $\approx 10^{12}$. At the same time, there is no doubt that atmospheric waves exist and play an important role in transferring energy and momentum. These empirical facts only become problematic when we consider the numerous apparently successful studies comparing data with linear (or weakly nonlinear) theory, commonly (for gravity waves) with the Taylor-Goldstein equations. Indeed, in the

words of [*Nappo*, 2002] "Almost all of what we know about the nature of gravity waves is derived from the *linear theory*" (emphasis in the original). From this, one may easily get the impression that linear wave theories have been empirically confirmed.

A closer look reveals that what has actually been scrutinized are the linear theory dispersion relations and that these have mostly been tested in the horizontal (and occasionally in the vertical) directions. Other predictions of linear theory - «polarization relations» - are invoked but are only used in a diagnostic mode so that they cannot be considered to have been convincingly validated. However, linear theory also predicts the entire space-time propagators relating the wave forcings and responses. A key characteristic of linear theories is that they involve integer powers of the (space and time) differential operators, and this strongly constrains the form of the propagators; below, we show how this allows us to test the theory by seeking possible anomalous propagator exponents.

In the last few years, scaling theories of waves have become more compelling. This is because empirical evidence and theoretical arguments have amassed to the effect that atmospheric dynamics give rise to emergent high Reynolds number scaling laws with different horizontal and vertical exponents. This allows the horizontal scaling to accurately apply over huge ranges in scale, (see [*Lovejoy and Schertzer*, 2010], [*Lovejoy and Schertzer*, 2013] for recent reviews). Although based on the classical laws of turbulence, they involve extensions to account for (multifractal) intermittency and anisotropy. Their success underlines the fundamental role of scale symmetries in constraining the high Re dynamics. It motivates the question: are atmospheric waves also scaling turbulent phenomena? If this is the case, we may logically expect anomalous wave propagators that could easily have dispersion relations identical or nearly indistinguishable from their classical counterparts, while simultaneously having nontrivial consequences for the dynamics and for understanding. Below, we investigate this using geostationary satellite infra red radiances.

4.2 Fractional propagators and turbulence

Consider the classical wave equation for the wave I with forcing f:

$$\left(\nabla^2 - \frac{1}{V^2}\frac{\partial^2}{\partial t^2}\right)^{H/2} I(\underline{r},t) = f(\underline{r},t) \tag{4.1}$$

where V is the wave velocity, $\underline{r}$ is the position vector and t the time variable. The usual wave equation has $H = 2$, but below we will consider the possibility that it is noninteger.

As usual, we can solve equation (4.1) by taking Fourier transforms (denoted by tildas):

$$\tilde{I}(\underline{k},\omega) = \tilde{g}(\underline{k},\omega)\tilde{f}(\underline{k},\omega); \qquad \tilde{g}(\underline{k},\omega) = \left(\omega^2/V^2 - \left|\underline{k}\right|^2\right)^{-H/2} \tag{4.2}$$

where $\underline{k}$ is the wavevector, ω the frequency and $\tilde{g}(\underline{k},\omega)$ the propagator. When H is a positive and even integer, the above follows directly, in other cases, we could define the fractional operator in equation (4.1) by the inverse Fourier Transform of $\tilde{g}(\underline{k},\omega)^{-1}$. If we seek the real space solution, we can use the fact that Fourier space products (eq. (4.2)) correspond to real space convolutions ("*") hence the solution to equation (4.1) is: $I(\underline{r},t) = g(\underline{r},t) * f(\underline{r},t)$ so that the propagator links the forcing (f) to the response (I). Note that the above propagator is symmetric with respect to an isotropic space-time scale transformation by factor λ^{-1}:

$$\tilde{g}\left(\lambda^{-1}\left(\underline{k},\omega\right)\right) = \lambda^H \tilde{g}\left(\left(\underline{k},\omega\right)\right) \tag{4.3}$$

In order to estimate the g($\underline{r}$,t) we can appeal to the method of stationary phase (e.g. [*Bleistein and Handelsman*, 1986]) which ensures that the dominant contribution to $g(\underline{r},t)$ is due to the wavenumber-frequency region over which $\tilde{g}(\underline{k},\omega)$ is singular, this singularity defines the dispersion relation and accounts for its origin and significance. From equation (4.1), we find the classical dispersion relation:

$$\omega = \pm V\left|\underline{k}\right| \tag{4.4}$$

which is therefore of fundamental importance, a fact which is true for any H>0, not only for positive even integer values of H.

Before attempting to estimate propagators of real data, we must take into account the fact that atmospheric waves occur in the presence of turbulence. Indeed the spectrum

is so strongly dominated by a "turbulent background" that it must first be removed before evidence of any wavelike propagator can be observed. This is paradoxical since the wavelike part is singular set over a surface in (k_x, k_y, ω) space and should be easy to detect (actually, the topology need not be so simple, see section 5). However, the singularity is of sufficiently low order and spectral estimates are sufficiently noisy that the surface is hard to observe. Indeed it is much easier to study 2-D subspaces obtained by integrating out one of the spectral coordinates (which also reduces the "noise") but this can integrate out the singularities. This is presumably the reason why one of the main techniques for empirically investigating atmospheric waves used an ad hoc averaging technique to observe various theoretically predicted dispersion relations by removing the turbulent contribution to the spectrum which was then studied on a single (k_x, ω) 2-D space [*Wheeler and Kiladis*, 1999], [*Hendon and Wheeler*, 2008].

Although we also use IR imagery (but at hourly not daily resolution), we use instead a theoretically motivated turbulent spectrum to search for evidence of anomalous wave propagators. To understand this, recall the classical Kolmogorov law of three dimensional isotropic turbulence:

$$\Delta I\left(\underline{\Delta r}\right) = \varphi\left|\underline{\Delta r}\right|^{H}; \quad \varphi = \varepsilon^{1/3}; \quad H = 1/3 \tag{4.5}$$

where I is a component of the wind, ΔI is a fluctuation, $\underline{\Delta r}$ is a vector displacement, φ is a driving turbulent flux, ε is the turbulent energy flux and the equality is understood in a statistical sense. In Fourier space this becomes:

$$\tilde{I}\left(\underline{k}\right) = \tilde{g}_{tur}\left(\underline{k}\right)\tilde{\varphi}\left(\underline{k}\right); \quad \tilde{g}_{tur}\left(\underline{k}\right) = \left|\underline{k}\right|^{-H} \tag{4.6}$$

comparing this with equation (4.2), we see that $\tilde{\varphi}\left(\underline{k}\right)$ is the forcing and $\tilde{g}_{tur}\left(\underline{k}\right)$ is the spatial part of a propagator (a Green's function). Now recall that for real I, that $\tilde{I}\left(\underline{k}\right) = \tilde{I}^{*}\left(-\underline{k}\right)$, if in addition we assume statistical translational invariance ("statistical homogeneity"), then we may define the spectral densities P_I, P_φ, by:

$$\left\langle \tilde{I}\left(\underline{k}\right)\tilde{I}\left(\underline{k}'\right)\right\rangle = \delta\left(\underline{k}+\underline{k}'\right)P_I\left(\underline{k}\right) \; ; \; \left\langle \tilde{\varphi}\left(\underline{k}\right)\tilde{\varphi}\left(\underline{k}'\right)\right\rangle = \delta\left(\underline{k}+\underline{k}'\right)P_\varphi\left(\underline{k}\right) \tag{4.7}$$

so that $P_I\left(\underline{k}\right) \propto \left\langle \left|\tilde{I}\right|^2 \right\rangle$, $P_\varphi\left(\underline{k}\right) \propto \left\langle \left|\tilde{\varphi}\right|^2 \right\rangle$ where "<>" denotes ensemble averaging.

To obtain the classical Kolmogorov-Obhukhov $k^{-5/3}$ law we use:

$$P_\varphi\left(\underline{k}\right) = P_0\left|\underline{k}\right|^{-s_\varphi}\ ;\quad s_\varphi = D - 1 - K(2) \tag{4.8}$$

where P_0 is a dimensional constant, d is the dimension of space and $K(2)$ is the second order intermittency correction. This yields:

$$P_I(\underline{k}) = P_\varphi(\underline{k})\left|\tilde{g}_{tur}\right|^2 = P_0\left|\underline{k}\right|^{-s_\varphi+2H} = P_0 k^{-s_\varphi+2H}\ ;\quad k = \left|k\right| \tag{4.9}$$

The angle integrated ("isotropic") spectral density E(k) is then given by integrating P over shells in Fourier space. Ignoring constant factors (2π in d = 2, 4π in d = 3), we obtain the (intermittency corrected) isotropic Kolmogorov law:

$$E\left(k\right) \approx P_I\left(k\right)k^{d-1} = k^{-\beta};\quad \beta = 1 + 2H - K\left(2\right) \tag{4.10}$$

(since H=1/3, we see that the nonintermittent K(2)=0 law does indeed have exponent β=5/3).

A basic consequence of wide range spatial scaling of atmospheric fields (in particular the wind) is that the spectrum and spectral density of the turbulent fluctuations in horizontal wavenumber - frequency (k_x, k_y, ω) space follow the straightforward space-time extension of equation (4.6):

$$\tilde{I}(\underline{k},\omega) = \tilde{g}_{tur}(\underline{k},\omega)\tilde{\varphi}(\underline{k},\omega);\quad P_I(\underline{k},\omega) = \left|\tilde{g}_{tur}(\underline{k},\omega)\right|^2 P_\varphi(\underline{k},\omega) \tag{4.11}$$

where $P_I(\underline{k},\omega)$, $P_\varphi(\underline{k},\omega)$ are space-time spectral densities, $\tilde{g}_{tur}(\underline{k},\omega)$ is the turbulent propagator. To yield turbulent-like behaviour, $\tilde{g}_{tur}(\underline{k},\omega)$ must be localized in space-time and hence it must have no singularities for nonzero real frequencies and wave vectors [*Lovejoy and Schertzer*, 2010] and [*Pinel et al.*, 2013, i.e. Chapter 3]. Using scaling symmetries, it was further argued that $\tilde{g}_{tur}$ can be expressed in terms of scale functions $\left\|\underline{k}\right\|$ which are anisotropic generalizations of the vector norm $\left|\underline{k}\right|$ in equation (4.6):

$$\tilde{g}_{tur}\left(\underline{k},\omega\right) = \left(i\omega' + \left\|\underline{k}\right\|\right)^{-H_{tur}}\ ;\quad \omega' = \left(\omega + \underline{k}\cdot\underline{\mu}\right)\sigma^{-1} \tag{4.12}$$

For our purposes, we may take a scale function $\left\|\underline{k}\right\|$ with the particularly simple form $\left\|\underline{k}\right\|^2 = k_x^2 + \left(k_y/a\right)^2$; a is the zonal (x) / meridional (y) aspect ratio. The transformation

$\omega \to \omega'$ corresponds to a mean advection by velocity $\underline{\mu}$ and σ accounts for the statistical variability of the (large scale) advection wind about its mean. The parameters are:

$$\underline{\mu} = \left(\overline{v_x}, \overline{v_y}\right) / V_w; \quad V_w = \left(\overline{v_x^2} + a^2 \overline{v_y^2}\right)^{1/2}; \qquad \sigma = \left(1 - \left(\mu_x^2 + a^2 \mu_y^2\right)\right)^{1/2} \tag{4.13}$$

where $\overline{v_x}$ and $\overline{v_y}$ are mean advection velocities, $\overline{v_x^2}$, $\overline{v_y^2}$, are the variances so that V_w is the large-scale turbulent wind speed at planetary scale (size L_e= 20000 km). In equation (4.10), the wavenumbers have been nondimensionalized by V_w and the frequencies ω by the corresponding eddy turn-over time "lifetime" L_e/V_w of the planetary scale structures. Note that a) the factor i in equation (4.12) is necessary so that the propagator respects causality, and b) overall $\tilde{g}_{tur}$ respects the same isotropic scaling symmetry as the wave propagator, equation (4.3) but with exponent H_{tur}.

4.3 Fractional propagators and waves

With the exception of the weak singularities associated with waves, the turbulence dominates the spectral density, the $P_I(\underline{k}, \omega)$ given in equation (4.11) with the propagator equation (4.12) already gives a good approximation to the empirical spectral density. This may be seen in Figure 4.1 using MTSAT data (described below) which shows the 1-D spectral densities E(k_x), E(k_y), E(ω) obtained by successively integrating out various pairs of variables from $P_I\left(k_x, k_y, \omega\right)$, (see [*Pinel et al.*, 2013, i.e. Chapter 3]). This turbulence part corresponds to the "background" spectrum obtained by [*Wheeler and Kiladis*, 1999]; any wave behaviour is to be found in deviations from this.

A simple model that takes into account waves while respecting both the space-time scaling and the turbulent forcing and background is obtained by including a factor $\tilde{g}_{wav}$ in the overall propagator. To be "wave-like", $\tilde{g}_{wav}$ must be unlocalized in space-time and must also be chosen so that the overall scaling symmetry of the system (eq. (4.3)) is respected by $\tilde{g}_I(\underline{k}, \omega)$. Inspired by equation (4.2) and equation (4.11), we can use the form:

$$\tilde{I}(\underline{k},\omega) = \tilde{g}_I(\underline{k},\omega)\tilde{\varphi}(\underline{k},\omega); \quad \tilde{g}_I(\underline{k},\omega) = \tilde{g}_{wav}(\underline{k},\omega)\tilde{g}_{tur}(\underline{k},\omega) \tag{4.14}$$

with $\tilde{g}_{tur}$ given by equation (4.12) and $\tilde{g}_{wav}$ given by:

$$\tilde{g}_{wav}(\underline{k},\omega) = \left(\omega'^2 / v_{wav}^2 - \|\underline{k}\|^2\right)^{-H_{wav}/2} \tag{4.15}$$

this is a generalization of equation (4.2) to account for spatial anisotropy (with $|\underline{k}| \to \|\underline{k}\|$). The replacement $\omega \to \omega + \underline{k} \cdot \underline{\mu}$ is the classical advection transformation (see e.g. [*Nappo*, 2002]); as in the turbulent propagator, we have included the extra factor σ to take into account the statistical variation of the large scale advection. Finally, the parameter v_{wav} is the phase speed nondimensionalized by the turbulent velocity V_w (eq. (4.13)). Note that the overall propagator $\tilde{g}_I$ satisfies the scaling symmetry equation (4.3) with $H = H_{tur}+H_{wav}$. Due to $\tilde{g}_{wav}$, the overall propagator $\tilde{g}_I$ yields the dispersion relation:

$$\omega = -\underline{k} \cdot \underline{\mu} \pm \sigma v_{wav} \|\underline{k}\| \tag{4.16}$$

With respect to the "background" advection (μ), σv_{wav} is the effective wave speed which takes into account the true mean wave speed (v_{max}) and the statistical variability via σ. By taking appropriate scale functions $\|\underline{k}\|$ one can obtain dispersion relations close to gravity and other waves (see *Lovejoy et al.*, 2008b).

Of more relevance here are Kelvin waves which are the low Coriolis parameter/ high "effective thickness" limit of the inertial gravity (Poincaré) wave dispersion relations often invoked at these space-time scales. First, for only one spatial (zonal) dimension, we may note that Kelvin waves are a special case of eq. (4.16) with $\|\underline{k}\| = k_x$. Considering the full horizontal plane, Kelvin waves are "channelled", only propagating in the zonal direction. To obtain some channeling while maintaining the same overall scaling symmetry, we could replace use the spatial (Fourier) scale function $\|\underline{k}\| = \left(k_x^2 + a^2 k_y^2\right)^{1/2}$ by $\|\underline{k}\| = \left(k_x^2 - a^2 k_y^2\right)^{1/2}$ which only allows meridional propagation for small scale (high wavenumber) structures. For example, when μ= 0, large structures with $k_x < \omega/(\sigma v_{wav})$ cannot propagate in the meridional direction, they are "channelled".

Finally, combining equations (4.12), (4.14) and (4.15), we obtain the turbulent wave spectral density:

$$P_I(\underline{k},\omega) = P_\varphi(\underline{k},\omega)\left(\omega'^2 + \left\|\underline{k}\right\|^2\right)^{-H_{tur}} \left(\omega'^2 / v_{wav}^2 - \left\|\underline{k}\right\|^2\right)^{-H_{wav}/2};$$

$$P_\varphi(\underline{k},\omega) = P_0\left(\omega'^2 + \left\|\underline{k}\right\|^2\right)^{-s_\varphi/2}; \quad \omega' = \left(\omega + \underline{k}\cdot\underline{\mu}\right)/\sigma \tag{4.17}$$

In equation (4.17), we have followed the assumption in the isotropic case (eq. (4.8)) that the forcing of the flux has the same scale symmetries as $\left|\tilde{g}_{tur}\right|^2$; s_φ is the spectral exponent of the flux and, P_0 a dimensional constant determined by the climatological (low frequency) average forcing.

4.4 Data Analysis

We follow [*Wheeler and Kiladis*, 1999], [*Hendon and Wheeler*, 2008] but estimate the turbulent background using regressions to estimate the parameters of $\tilde{g}_I$ (i.e. of $\tilde{g}_{tur}$ and $\tilde{g}_{wav}$). The data set was comprised of 1386 images (~ two months of data, September and October 2007) of radiances measured by the first "thermal" infrared channel (10.3-11.3 μm, particularly sensitive to temperature near the top of clouds) of the geostationary satellite MTSAT over south-west Pacific at resolutions 30 km and 1 hr over latitudes 40°S - 30°N and longitudes 80°E - 200°E. We separated the sample into five 277 hr (~12 day) blocks, calculating for each block, the spectral density of fluctuations of the field with respect to the mean image (we used a standard Hann window to reduce spectral leakage).

To see how a purely turbulent spectrum already provides a good approximation, we performed a multivariate regression on the empirical MTSAT spectral density and theoretical form (eq. (4.17)) with $H_{wav} = 0$. Figure 4.1 shows the 1D spectra obtained by integrating the 3D density over the complementary coordinates using $s_\varphi = 2.88\pm0.01$ and $H_{tur} = H = 0.26\pm0.05$. The fit is good over the range of scales 120-5000 *km* in space and 3-100 *hrs* in time (except for small diurnal contributions at 12 and 24 *hrs*), it is especially good if we numerically take into account finite sample size effects at the large and small scales (the curvature in the black line in Figure 4.1). The excellent superposition confirms

the scale symmetry of the type equation (4.3): $P_I(\lambda^{-1}(\underline{k},\omega)) = \lambda^{s_I} P_I(\underline{k},\omega)$ with $s_I = s_\varphi + 2$ $H = 3.4\pm0.1$ (eq. (4.17)).

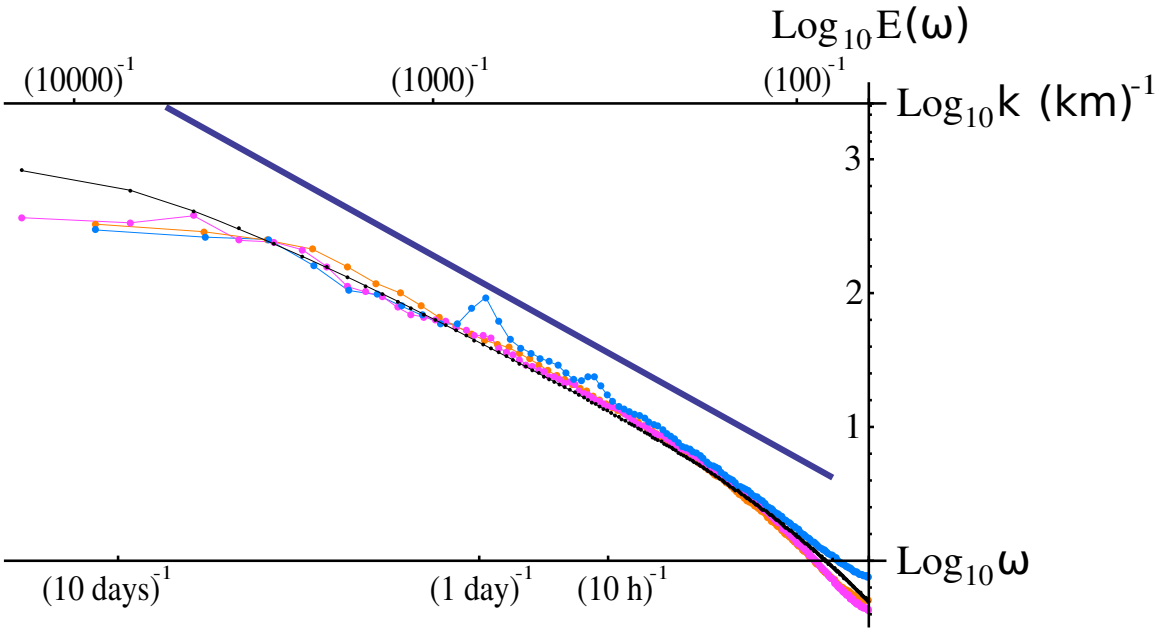

Figure 4.1: 1D spectra from MTSAT data; blue: temporal; orange: meridional; purple: zonal and a multivariate regression curved due to the finite empirical domain; black, using H_{wav} = 0, V_w = 41±3 km/h; $\tau_w = L_e/V_w \approx$ 20±1 days**;** $a \approx$ 1.2±0.1 ; $s_I \approx$3.4±0.1; P_0=2.8±0.2 °C^2 km^2 h; $\mu_x \approx$ -0.3±0.1; ($\overline{v_x} \approx$ -12±4 km/h); $\mu_y \approx$ 0.10±0.08; ($\overline{v_y} \approx$ 4±3 km/h), ς= 0.95±0.03 (reproduced from [*Pinel et al.*, 2013, i.e. Chapter 3]).

We now consider the three 2D spectra, obtained by successively integrating the 3D spectral density over k_x, k_y and ω. The fit is sufficiently good that we can use the above regression with H_{wav} = 0 to estimate all the turbulent parameters. However for the 1-D spectra to have fixed exponents, when fitting the wave part we must use the constraint $H = H_{tur}+H_{wav}$ so that the 1-D spectral slopes are not affected. In this way we find an optimum relative weighting for the turbulence and wave contributions. Figure 4.2 shows these for three different values of H_{wav}. As before, the purely turbulent (H_{wav} = 0) case gives a good fit with mean deviations ±14% in the three 2D spaces (excluding the diurnal spikes and the origin). The orientations of the contours of P(k_x, ω), P(k_y, ω) is a

consequence of the non zero mean zonal velocity $\overline{v_x}$ ~ -12±4 km/h and smaller meridional $\overline{v_y}$ ~ 4±3 km/h, the wave part is the residual: $|\tilde{g}_{wav}|^2 \propto P_I(\underline{k},\omega)\left(\omega'^2 + \|\underline{k}\|^2\right)^{S_\varphi/2+H_{tur}}$, see equation (4.5). Although this is noisy, the value $H_{wav}\approx$ 0.17±0.04 (so that $H_{tur} = H - H_{wav}$ = 0.09±0.06, H = 0.26±0.05 is fixed) gives the best overall fit and nondimensional wave speed v_{wav} =1.0±0.8. The latter means that the wave speed is nearly equal to the turbulent wind so that on average the waves can be roughly stationary.

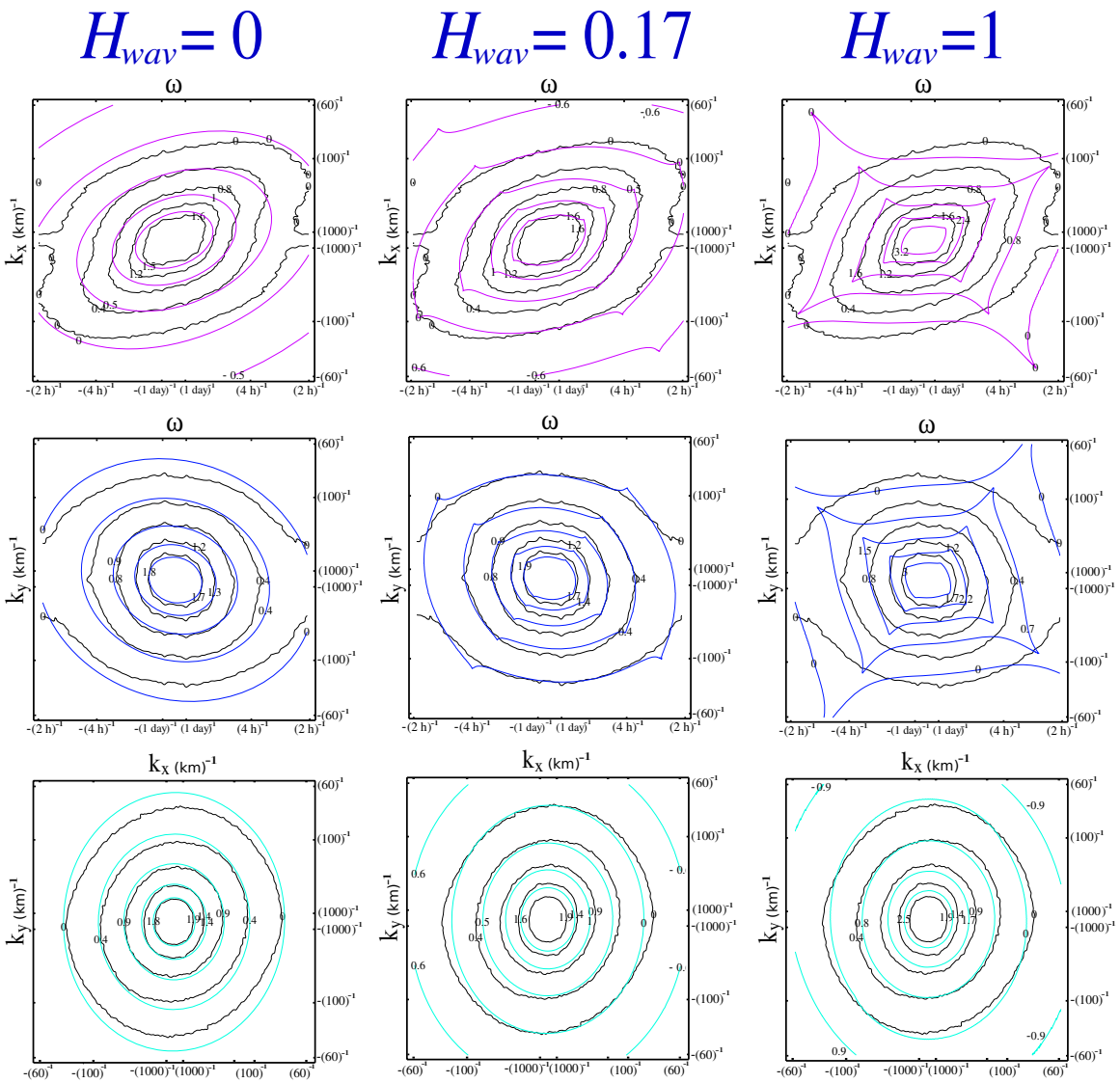

Figure 4.2: Comparison of 2D spectral densities from MTSAT data and a multivariate regression from theoretical $P_I(\underline{k},\omega)$ given by eq.17 for three different values of H_{wav}. The 2D subspaces (top to bottom) are (ω, k_x), (ω, k_y) and (k_x, k_y). The ranges are ω from (2 h)$^{-1}$ to (277 h)$^{-1}$; k_x from (60 km)$^{-1}$ to (≈ 13000 km)$^{-1}$ and k_y from (60 km)$^{-1}$ to (≈8000 km)$^{-1}$. The three different values of H_{wav} are 0, 0.17 and 1 from left to right (with H_{tur} = H - H_{wav}, H = 0.26±0.05, s_φ= 2.88±0.01). H_{wav} = 0 corresponds to the purely turbulent case, H_{wav} = 0.17±0.04 to the regression value with V_w = 41±3 km/h; τ_w= L_e/V_w ≈ 20±1 days; a ≈1.2±0.1; s_I ≈3.4±0.1; P_0 = 2.8±0.2 °C^2 km^2 h; μ_x ≈ -0.3±0.1; ($\overline{v_x}$ ≈ -12±4 km/h); μ_y≈ 0.10±0.08; ($\overline{v_y}$ ≈ 4±3 km/h) hence, σ =0.95±0.03 and nondimensional wave speed v_{wav} = 1.0±0.8.

4.5 Refined singularity analysis

The above analysis is paradoxical since our hypothesis is that there is a singular surface in (k_x, k_y, ω) space yet analysis of the 1-D and 2-D sections showed no direct evidence of singular behaviour. This is consistent with the finding that $0<H_{wav}<1$ implying that the singularities are integrated out in the lower dimensional sections. In order to display potential singularities, we are therefore forced to study the full 3D density $P(k_x, k_y, \omega)$ recognizing that most of the variation is due to the turbulent part and that the wave part - being only weakly singular - is expected to manifest itself in local maxima, perhaps with surface-like topology (line-like in (k_x, k_y) sections). To this end, we implemented an ad hoc singularity detection algorithm that "scans" parallel to the axes to estimate local maxima successively in the k_x, k_y directions. In principle considering the maxima in a single direction is adequate, but in practice the singular surface has parts that are roughly parallel to a given axis; the resulting ambiguity can be resolved by determining maxima in two orthogonal directions.

The results are shown in Figure 4.3, where we compare such an analysis with the theoretical behaviour for constant ω sections. A drawback of the method is that it does not distinguish maxima due to the turbulent contribution and from the (presumed) wave contribution and in the empirical case, the separation is not always evident. In the figure, the two have been distinguished by the color of the lines. We see that although far from perfect, the ellipses indicating the theoretical singularity (dispersion relation) are close to the empirical ones especially at the higher ω. Given that we used a straightforward generalization of the classical wave equation with only one new parameter v_{wav} (two if we

include $H_{wav} = 0.17 \pm 0.04$ but this doesn't affect the singular surface), the results are quite encouraging, yet they indicate some of the difficulties.

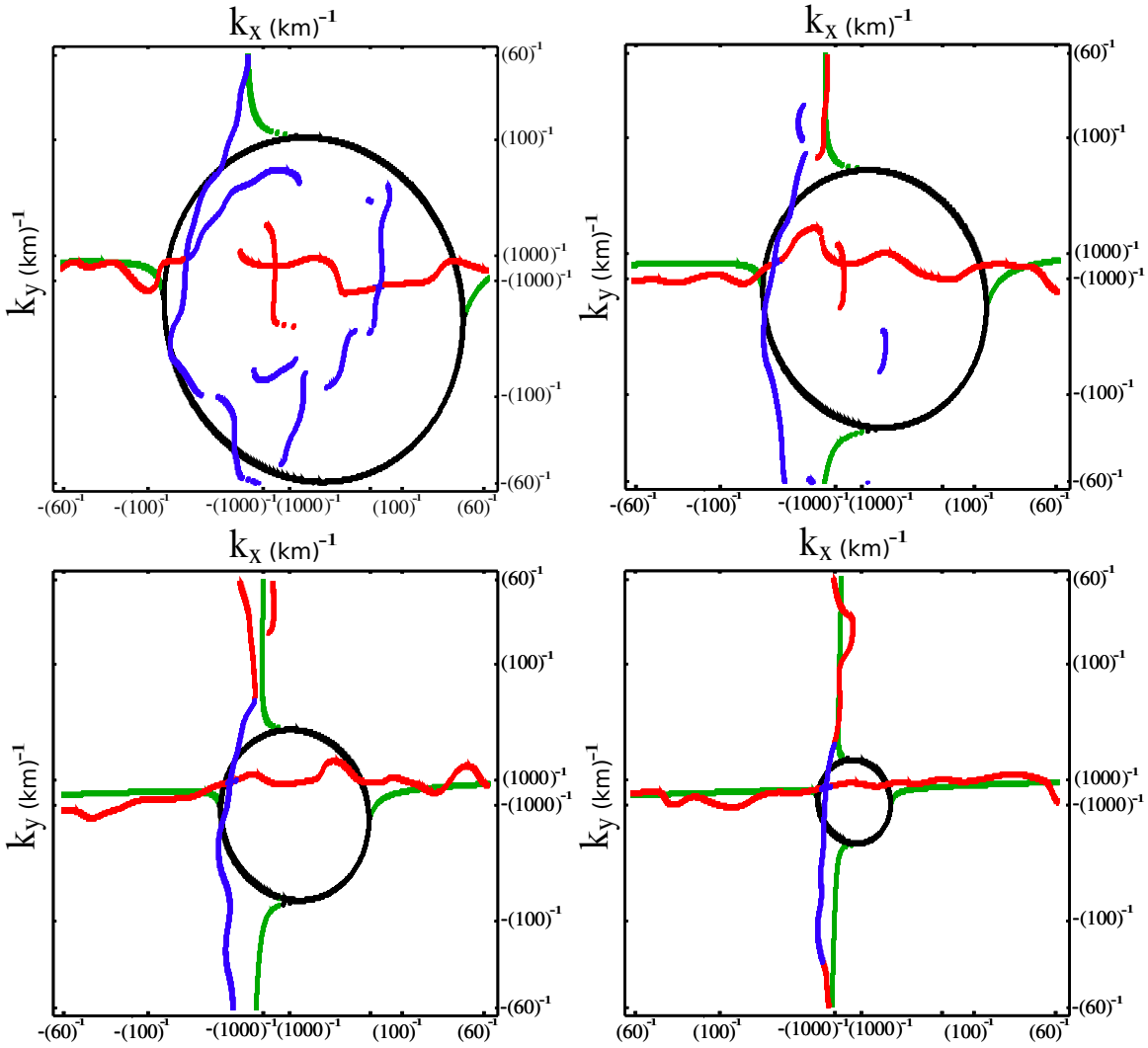

Figure 4.3: Left to right, top to bottom, four (k_x, k_y) sections of $P(k_x, k_y, \omega)$ for $\omega = 2, 3, 5, 10$ hr^{-1}, origin in the centre. The black line is the theoretical singularity (dispersion) curve (eq.14); the blue, the empirically estimated curve using the ad hoc algorithm and the green and red show maxima but presumed to originate in the turbulence "background" (they are very close to the axes).

4.6 Conclusion

The atmosphere is highly nonlinear yet displays both turbulent and wavelike behaviour over huge ranges of space-time scales. Theories explaining the turbulent aspects assume that the dynamics are strongly nonlinear and scaling, in contrast, the

corresponding wave theories have been linear or weakly nonlinear. We proposed that the paradox can be explained by noting that although linear theory predicts propagators, only the relations implied by the singular part of the latter - the dispersion relations - have been tested to any extent. The mathematical structure of the turbulent laws that link the observables to driving turbulent fluxes (such as energy fluxes) use scaling (turbulent) propagators which are very similar to that of wave equations except that the latter are singular. To account for both waves and turbulence, the actual propagators need only respect scale symmetries and can be modelled as products of turbulent-like and wave-like (space-time localized and unlocalized) propagators with both involving anomalous exponents. The wave propagator we used involves the mean horizontal turbulent wind and energy flux as well as a mean background wave advection velocity, obtained as a (anisotropic, fractional) generalization of the classical wave equation (which is approximately satisfied by inertial gravity waves and Kelvin waves). Using geostationary IR radiances, we found that the best fit involved an anomalous wave scaling exponent, $H_{wav} \approx 0.17 \pm 0.04$.

This paper is simply an early attempt to understand waves in highly turbulent media using scaling symmetries as contraints. Ideally, other fields should be studied over wide scale ranges and this in the full (x, y, z, t) space.

Chapter 5: Conclusions

This thesis addresses the problem of understanding and quantifying the variability of atmospheric fields over wide ranges of space-time scales. It is surprising that even with the increase in the quantity and quality of atmospheric data, there is still no consensus on the basic nature of atmospheric dynamics and how its statistical properties change with scale.

We have presented space-time wave extensions of a scaling model, the 23/9D model, which is a generalization of the classical laws of turbulence and which describes atmospheric dynamics taking into account the strong intermittency and stratification of the atmosphere. In this model, the scaling symmetry holds from the dissipation scale up to planetary scales in an *anisotropic* manner. This contrasts with the standard 2D/3D isotropic model of atmospheric turbulence which retains the isotropy assumption, involving two scaling regimes: a 3D isotropic regime at small scales and a 2D isotropic regime at large scales; the two regimes being separated at 10 km by a break in the horizontal scaling. The only empirical evidence giving any support to the 2D/3D isotropic model is from horizontal wind measured by aircraft which exhibit a break in the horizontal scaling at few hundreds of km (not at 10 km) and from a H=1/3 regime at small scales to a H=0.7 regime at large scales (but not to a H=1 regime at large scales as is predicted by the 2D/3D model). Since H=0.7 is a value measured by drop sondes in the vertical, a simple explanation is that aircraft follow gently sloping trajectories - such as isobars - so that for large enough scales, vertical (rather than horizontal) fluctuations dominate the statistics. In order to test this, we used GPS and TAMDAR sensor equipped commercial aircraft data and obtained for the first time the joint horizontal-vertical structure function. The results provide strong support to the 23/9D model. We estimate D ~ 2.57±0.02, (to be compared to the theoretical value 23/9 ≈2.56) which is far from the d=2 (large scales) and d=3 (small scales) values of the standard theory.

In chapter 3, we studied the consequences of this spatial anisotropy for the full horizontal space-time statistics. Using the fact that smaller structures are advected by larger ones and by considering averages over the latter we estimated the scale function and hence the statistics and tested these predictions using geostationary satellite MTSAT

IR data over the range (5 km to ~10000 km, 1 hour to 2 months). We found that our model could accurately reproduce the 3D (k_x, k_y, ω) spectral density over the range 1 hour to ≈4 days and 30 km to ≈5000 km. To test our model, we needed a dataset with large enough ranges of scales available in space and time. Such datasets are not available at the moment in full (x, y, z, t) space so that we used atmospheric radiances measured by geostationary satellite which are (x, y, t) fields. If high resolution (x, y, z, t) atmospheric fields become available, they will make possible an understanding of the role of the vertical wind.

To obtain a more complete description of the statistics, we also found in chapter 3 that we can describe atmospheric radiances turbulent flux statistics (including TRMM's infrared and passive microwave over scale ranges 100 km to 20000 km, 1 day to 1 year) with our model over large ranges of spatial scales with typically slight deviations at small and large scales. This also allowed us to characterize space-time statistics with the Eulerian relation between sizes of structures and their lifetimes ("eddy turnover time") which is used to construct Eulerian space-time and space-space diagrams.

In chapter 4, we presented an extension of the 23/9D model to include atmospheric waves (and not only turbulence) in the description. The theoretical development proposed is based on an effective turbulence - wave propagator which corresponds to a fractional and anisotropic extension of the classical wave equation propagator with dispersion relation similar to those of inertial gravity waves (and Kelvin waves) yet with anomalous (fractional) order $H_{wav}/2$. Using geostationary MTSAT IR radiances, we estimated the parameters finding that H_{wav} ≈0.17 (the classical value =2). Even though we tested our model with a very simple propagator (a fractional extension of the classical wave equation), since the only constraint on the form of the propagators is the scaling symmetry, different forms of propagators leading to different dispersion relations should be investigated in the future.

Characterizing the space-time statistical properties of atmospheric fields as a function of scale is essential for our fundamental understanding of the dynamics of the atmosphere. It has also direct applications, whether it is to validate or improve weather models (for instance with stochastic sub-grid parameterizations). It also prescribes the space-time resolutions at which measurements should be made in order to improve their

efficiency. It also provides a consistent theoretical basis for the description of atmospheric waves or to interpret Atmospheric Motion Vectors in terms of turbulence.

Appendix A

This appendix contains the supplementary material related to the paper "Pinel, J., S. Lovejoy, D. Schertzer, A. F. Tuck, (2012): Joint horizontal - vertical anisotropic scaling, isobaric and isoheight wind statistics from aircraft data, Geophys. Res. Lett. 39, L11803, doi:10.1029/2012GL051689" which is presented in chapter 2.

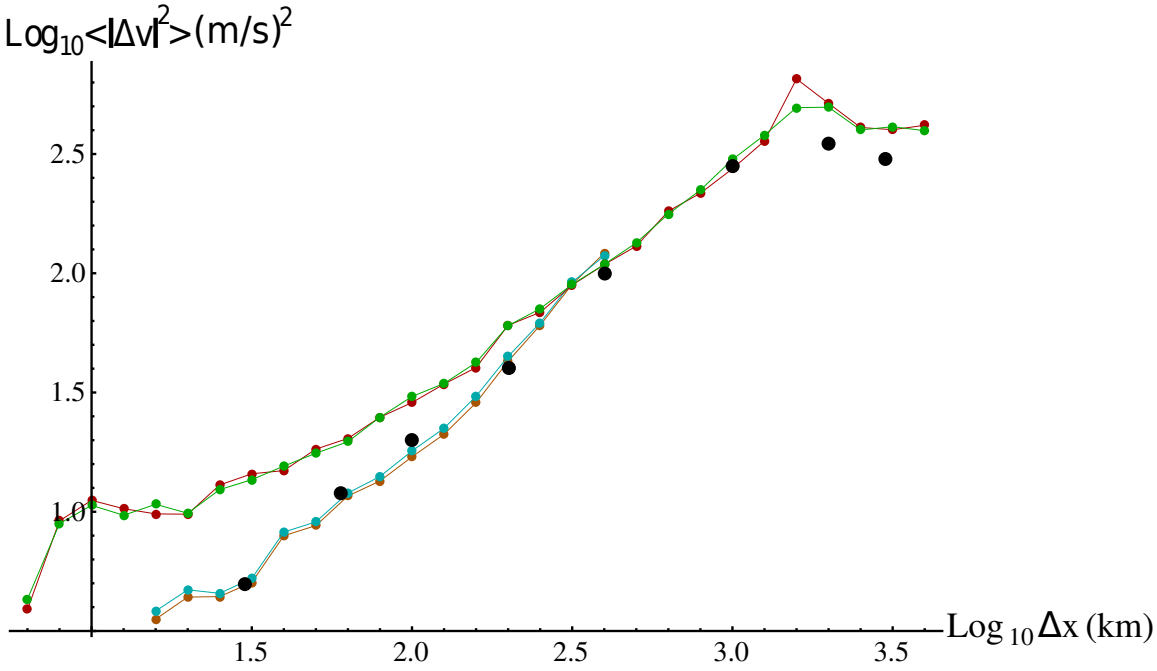

Figure A.1: Comparison of our analysis with the results obtained by Frehlich and Sharman. We show second order structure function for the transverse component of the wind measured by TAMDAR. Unlike the figures in the paper, here we include the low resolution ascending and descending flights segments; we also compare structure functions from two aircraft (top pair), and single aircraft (bottom pair). This analysis was made on the same latitude band as Ferhlich and Sharman (40N-50N) and between roughly the same altitude levels (5km-6km), using the same criteria for near-constant pressure (Δp<4 hPa) and altitude (Δz<200 m) levels. In Blue: data from the same aircraft at near-constant altitude levels. In brown: data coming from the same aircraft at near-constant pressure levels. In green: data coming from different aircraft at near-constant altitude levels. In red: data coming from different aircraft at near-constant pressure levels. The large black dots are reproduced from the Frehlich and Sharman TAMDAR analysis.

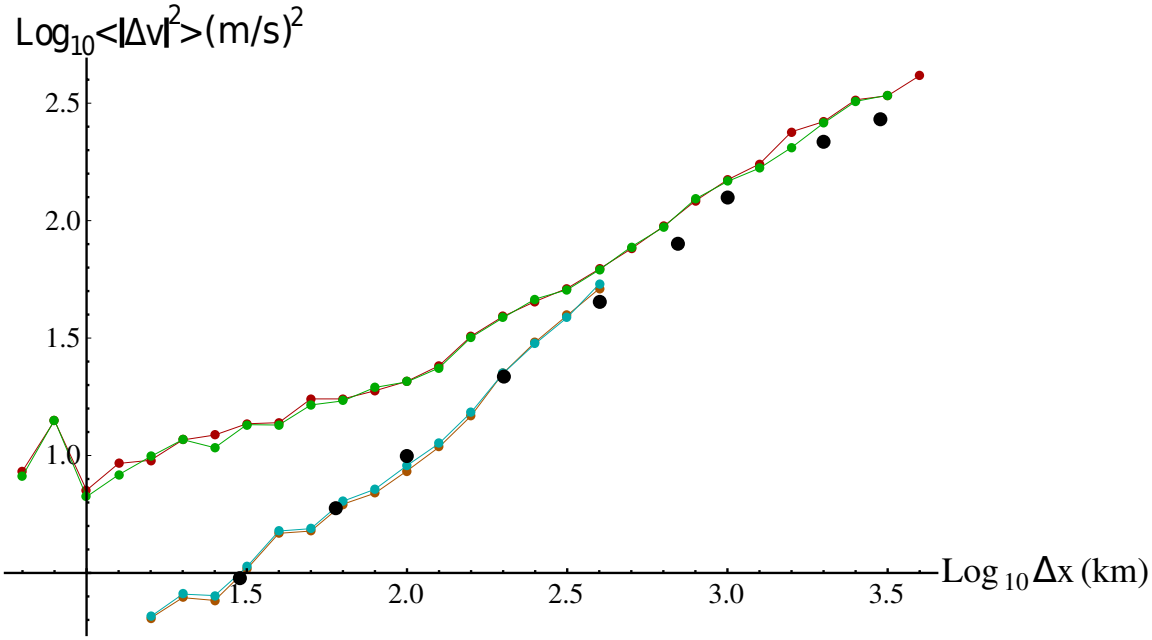

Figure A.2: Same as Figure A.1, but for longitudinal component.

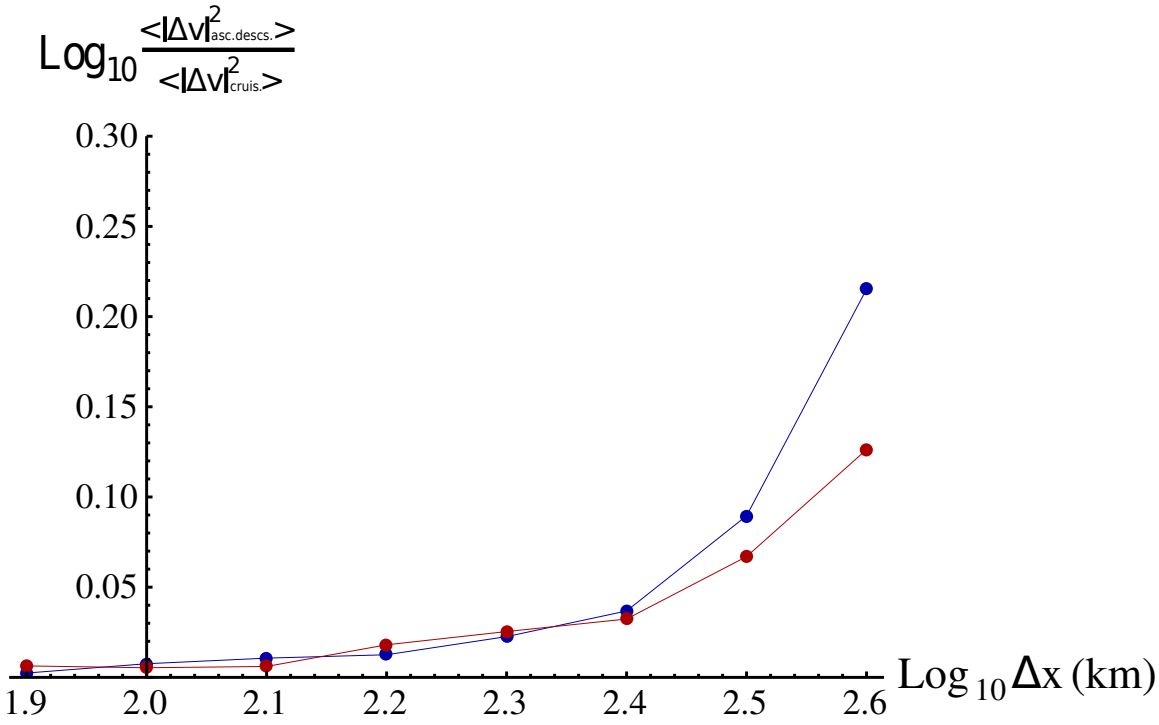

Figure A.3: Difference between log of second order structure functions for cruising parts only and for complete flights, including ascending and descending parts (after take off and before landing). In blue (red): transverse (longitudinal) component. This is for complete year 2009 for latitudes 20N-50N, between 5-5.5 km of altitudes.

BIBLIOGRAPHY

Batchelor, G.K., (1953): *The Theory of Homogeneous Turbulence*, Cambridge: Cambridge University Press.

Batchelor, G.K., A.A. Townsend, (1949): The nature of turbulent motion at large wave-number. Proc. R. Soc. Lond. A 199:238-55

Bleistein, N., and R. A. Handelsman, (1986), *Asymptotic Expansions of Integrals*, Dover, Mineola.

Bolgiano, R., Jr., (1959): Turbulent Spectra in a Stably Stratified Atmosphere, J. Geophys. Res., 64(12), 2226-2229, doi:10.1029/JZ064i012p02226.

Charney J.G. (1971): Geostrophic Turbulence, J. Atmos. Sci 28, p. 1087.

Corrsin, S., (1951): On the spectrum of isotropic temperature fluctuations in a isotropic turbulence. Journal of Applied Physics 22, 469-73.

Daniels, T. S., G. Tsoucalas, M. Anderson, D. Mulally, W. Moninger, R. Mamrosh, (2004): Tropospheric Airborne Meteorological Data Reporting (TAMDAR) Sensor Development. 11th Conf. on Aviation

Dias, J., S. N. Tulich and G. N. Kiladis, (2012): An object based approach to assessing tropical convection organization. J. Atmos. Sci., 69, 2488-2504

Fjortoft, R. (1953): On the changes in the spectral distribution of kinetic energy in two dimensional nondivergent flow. Tellus 7, 168-76.

Frehlich, R.G., R.D. Sharman, (2010): Equivalence of velocity statistics at constant pressure or constant altitude, GEOPHYSICAL RESEARCH LETTERS, VOL. 37, L08801, 5 PP.

Hendon, H. H., and M. Wheeler (2008), Some space-time spectral analyses of tropical convection and planetary waves, *J. Atmos. Sciences*, *65*, 2936-2948.

Kigawa S., and P. C. Sullivan, (1998): Meteorological Satellite Center Technical Note, No.36, December.

Kolmogorov, A.N. (1941): Local structure of turbulence in an incompressible liquid for very large Reynolds numbers. (English translation: Proc. Roy. Soc. A434, 9-17, 1991), Proc. Acad. Sci. URSS., Geochem. Sect. 30, pp. 299-303.

Kraichnan, R.H. (1967): Inertial ranges in two-dimensional turbulence, Physics of Fluids 10, pp. 1417-1423.

Landau, L., E.M. Lifshitz, (1944): *Continuum Mechanics*, (Gostekhizdat, Moscow, in Russian)

Landau, L., E.M. Lifshitz, (1987): *Fluids Mechanics*, Vol. 6 (2nd ed.), Butterworth-Heinemann

Leese, J.A.; Novak, C.S.; Taylor, V.R., (1970): The Determination of Cloud Pattern Motions from Geosynchronous Satellite Image Data. Pattern Recognition 2, 279-292.

Lilley, M., S. Lovejoy, K. Strawbridge, D. Schertzer, (2004) : 23/9 dimensional anisotropic scaling of passive admixtures using lidar aerosol data, Phys. Rev. E, 70, 036307-1-7.

Lilley, M., S. Lovejoy, K. Strawbridge, D. Schertzer, A. Radkevich, (2008): Scaling turbulent atmospheric stratification, Part II: spatial stratification and intermittency from lidar data Quart. J. Roy. Meteor. Soc., 134, 301-315.

Lindborg, E., (1999): Can the atmospheric kinetic energy spectrum be explained by two-dimensional turbulence? J. Fluid Mech., 388, 259–288.

Lindborg, E., et al. (2009): Comment on "Reinterpreting aircraft measurments in anisotropic scaling turbulence" by Lovejoy et al 2009, Atmos. Chem. Phys. Discuss., 9, 22331-22336.

Lindborg, E., et al., (2010): Interactive comment on "Comment on "Reinterpreting aircraft measurements in anisotropic scaling turbulence by S. Lovejoy et al. (2009)" Atmos. Chem. Phys. Disc., 9, C9797-C9798"

Lovejoy, S., D. Schertzer, (2010): Towards a new synthesis for atmospheric dynamics: space-time cascades, Atmos. Res. 96, pp. 1-52, doi.1016/j.atmosres.2010.01004.

Lovejoy, S., D. Schertzer, (2011): Space-time cascades and the scaling of ECMWF reanalyses: fluxes and fields, J. Geophys. Res. 116, D14117 doi:10.1029/2011JD015654.

Lovejoy, S., D. Schertzer, (2013): *The weather and climate, Emergent laws and multifractal cascades*. Cambridge University Press. Cambridge, UK.

Lovejoy, S., Schertzer, D., and Tuck, A. F. (2004): Fractal aircraft trajectories and nonclassical turbulent exponents, Phys. Rev. E, 70(3), 5 pp.

Lovejoy, S., Tuck, A. F., Hovde, S. J., and Schertzer, D. (2007): Is isotropic turbulence relevant in the atmosphere?, Geophys. Res. Lett., 34, L14802, doi:10.1029/2007GL029359.

Lovejoy, S., D. Schertzer, M. Lilley, K. Strawbridge, A. Radkevich, (2008): Scaling turbulent atmospheric stratification, Part I: turbulence and waves, Quart. J. Roy. Meteor. Soc., 134, 277-300.

Lovejoy, S., A.F. Tuck, D. Schertzer, S.J. Hovde, (2009a): Reinterpreting aircraft measurements in anisotropic scaling turbulence, Atmos. Chem. Phys. 9, 1-19.

Lovejoy, S., A.F. Tuck, D. Schertzer, (2009b): Interactive comment on "Reinterpreting aircraft measurements in anisotropic scaling turbulence" by S. Lovejoy et al., Atmos. Chem. Phys. Disc., 9, S2592- S2599.

Lovejoy, S., A.F. Tuck, D. Schertzer, (2009c): Interactive comment on "Comment on "Reinterpreting aircraft measurements in anisotropic scaling turbulence" by Lovejoy et al. (2009)" by E. Lindborg et al, Atmos. Chem. Phys. Disc., 9, C7688-C7699.

Lovejoy, S., D. Schertzer, V. Allaire, T. Bourgeois, S. King, J. Pinel, J. Stolle, (2009d): Atmospheric complexity or scale by scale simplicity? Geophys. Res. Lett., 36, L01801, doi:10.1029/2008GL035863.

Lovejoy, S., A.F. Tuck, D. Schertzer, (2010): The Horizontal cascade structure of atmospheric fields determined from aircraft data, J. Geophys. Res., 115, D13105, doi:10.1029/2009JD013353.

Mandelbrot, B.B., (1974): Intermittent turbulence in self-similar cascades: divergence of high moments and dimension of the carrier. Journal of Fluids Mechanics 62, 331-50.

Monin, A. S., and A. M. Yaglom, (1975): Statistical Fluid Mechanics: Mechanics of Turbulence. Vol. 2. MIT Press.

Moninger,W.R., S. G. Benjamin, B. D. Jamison, T. W. Schlatter, T. L. Smith, and E. J. Szoke, (2008): New TAMDAR fleets and their impact on Rapid Update Cycle (RUC)

forecasts, 13th Conference on Aviation, Range and Aerospace Meteorology , January 2008, New Orleans, LA, Amer. Meteor. Soc.

Nappo, C. J. (2002), *An introduction to Gravity Waves*, 276 pp., Academic Press, Amsterdam.

NASDA, (2001): TRMM data users handbook. National Space Development Agency of Japan Earth Observation Center.

Novikov, E.A., R. Stewart, (1964): Intermittency of turbulence and spectrum of fluctuations in energy-dissipation. Izv. Akad. Nauk SSSR. Ser. Geofiz. 3, 408-12.

Ogura, Y., 1952: The structure of two-dimensionally isotropic turbulence. J. Meteor. Soc. Japan, 30, 59–64.

Obukhov, A., (1949): Structure of the temperature field in a turbulent flow. Izv. Akad. Nauk SSSR. Ser. Geogr. I Geofiz 13, 55-69

Obukhov, A., (1959): Effect of archimedean forces on the structure of the temperature field in a turbulent flow, Dokl. Akad. Nauk SSSR 125

Puschell, J.J., H.A. Lowe, J. Jeter, S. Kus, R. Osgood, W.T. Hurt, D. Gilman, D. Rogers, R. Hoelter, A. Kamel, (2003): Japanese Advanced Meteorological Imager (JAMI): Design, Characterization and Expected On-Orbit Performance. Proceedings of international TOVS study conference, Sainte Adele, Canada.

Puschell, J.J., H.A. Lowe, J. Jeter, S. Kus, W.T. Hurt, D. Gilman, D. Rogers, R. Hoelter, R. Ravella, (2002): Japanese Advanced Meteorological Imager: a next generation GEO imager for MTSAT-1R, SPIE Proceedings 4814, pp. 152-161

Pinel, J., S. Lovejoy, D. Schertzer, A. F. Tuck, (2012): Joint horizontal - vertical

anisotropic scaling, isobaric and isoheight wind statistics from aircraft data, Geophys. Res. Lett. 39, L11803, doi:10.1029/2012GL051689.

Pinel, J., S. Lovejoy, and D. Schertzer, (2013), The horizontal space-time scaling and cascade structure of the atmosphere inferred from satellite radiances, *Atmos. Res.*, (submitted 10/12).

Pinel, J., S. Lovejoy, (2013): Atmospheric waves as scaling, turbulent phenomena. Geophys. Res. Lett., (submitted 10/12).

Radkevich, A., S. Lovejoy, K. Strawbridge, D. Schertzer, (2007): The elliptical dimension of space-time atmospheric stratification of passive admixtures using lidar data, Physica A, doi: 10.1016/j.physa.2007.03.046, 382, 597-615.

Radkevich, A., S. Lovejoy, K. Strawbridge, D. Schertzer, M. Lilley, (2008): Scaling turbulent atmospheric stratification, Part III: Space-time stratification of passive scalars from lidar data, Quart. J. Roy. Meteor. Soc., 134, 316-335.

Richardson, L.F., (1922): Weather Prediction by Numerical Process. Cambridge: Cambridge University Press. Republished by Dover, 1965

Reynolds, O., (1883): An experimental investigation of the circumstances which determine whether the motion of water in parallels channels shall be direct or sinuous and of the law of resistance in parallels channels. Philosophical Transactions of the Royal Society, 174:935-982

Schertzer D, Lovejoy S. (1985a): The dimension and intermittency of atmospheric dynamics. Turbulent Shear Flow 4 Launder B. (ed). Springer-Verlag: Berlin. pp. 7–33

Schertzer, D., S. Lovejoy, (1985b): Generalised scale invariance in turbulent phenomena, Physico-Chemical Hydrodynamics Journal, 6, 623-635.

Schertzer, D., S. Lovejoy, (1987): Physical Modeling and Analysis of Rain and Clouds by Anisotropic Scaling Multiplicative Porcesses. J. Geophys. Res. 92, 9692-9714.

Schertzer, D., S. Lovejoy, (1997): Universal Multifractals do Exist!: Comments on "A statistical analysis of mesoscale rainfall as a random cascade", J. Appl. Meteor. 36, 1296-1303.

Schertzer, D., S. Lovejoy, F. Schmitt, I. Tchigirinskaya, D. Marsan, (1997): Multifractal cascades dynamics and turbulent intermittency. Fractals 5, 427-71

Schertzer, D., I. Tchigirinskaya, S. Lovejoy, A. Tuck, (2011) : Quasi-geostrophic turbulence and generalized scale invariance, a theoretical reply, Atmos. Chem. Phys. Discuss., 11, 3301-3320, 201111/10.

Schertzer, D., I. Tchigirinskaya, S. Lovejoy, A. Tuck, (2012): Quasi-geostrophic turbulence and generalized scale invariance, a theoretical reply, Atmos. Chem. Phys., 12, 327-336, 2012, doi:10.5194/acp-12-327-2012.

Stolle, J., S. Lovejoy, D. Schertzer, (2010): The stochastic cascade structure of deterministic numerical models of the atmosphere, Nonlin. Processes Geophys., 16, 607-621.

Stolle, J., S. Lovejoy, D. Schertzer, (2012): The temporal cascade structure and space-time relations for reanalyses and global circulation models, in press, Q. J. Roy. Meteor. Soc.

Szantai, A. and G. Seze, (2008): Improved extraction of low-level atmospheric motion vectors over west-Africa from MSG images. 9th International Winds Workshop, 14-18 April 2008, Annapolis, MD, USA, pp. 1-8

Takeuchi, W., T. Nemoto, T. Kaneko, Y. Yasuoka, (2010): Development of MTSAT data processing, distribution and visualization system on WWW. Asian Journal of Geoinformatics, 10(3), 29-33.

Taylor, GI, (1938): The Spectrum of Turbulence. Proc. R. Soc. Lond. A 164 919 476-490; doi:10.1098/rspa.1938.0032

Tennekes, H., (1975): Eulcrian and Lagrangian time microscales in isotropic turbulence. J. Fluid Mech., Vol. 67, pp.561-567.

Tuck, A. F., (2008): *Atmospheric Turbulence: a molecular dynamics perspective*, Oxford University Press, Oxford, UK.

Van der Hoven, I. (1957): Power spectrum of horizontal wind speed in the frequency range from .0007 to 900 cycles per hour, J. Meteorol., 14, 160-164.

Wheeler, M., and G.N. Kiladis, (1999): Convectively coupled equatorial waves: analysis of clouds and temperature in the wavenumber-frequency domain, J. Atmos. Sciences 56, pp. 374-399.

Yaglom, A.M. (1966): The influence on the fluctuation in energy dissipation on the shape of turbulent characteristics in the inertial interval. Sov. Phys. Dokl. 2, 26-30.

Yano, J., (2009): Comment on "Reinterpreting aircraft measurments in anisotropic scaling turbulence" by Lovejoy et al 2009, Atmos. Chem. Phys. Discuss., 9, S162-S166.